



Modelling of the rotating packed bed for post-combustion carbon capture using Eulerian porous medium approach

GUOJUN ZHANG

A thesis submitted to the University of Sheffield in partial fulfilment of the requirements for the degree of Doctor of Philosophy

The University of Sheffield
Faculty of Engineering
Department of Mechanical Engineering

August 2023

DECLARATION

The candidate attests that the submitted work is original, with the exception of content collaboratively authored and integrated from joint publications. The contributions of the candidate and the other authors to this work have been clearly outlined below. The candidate further confirms that appropriate credit has been given in the thesis when referencing the work of others.

A part of Chapter 2 of this thesis has been reviewed by *Carbon Capture Science and Technology*, the work conducted in Chapter 4 and Chapter 5 of this thesis has been published in *Chemical Engineering Science*, the work conducted in Chapter 6 of this thesis has been review by *Industrial & Engineering Chemistry Research*.

I conducted the CFD simulations and drafted the papers. My supervisors, Professor Lin Ma, Professor Derek B. Ingham and Professor Mohammed Pourkashanian offered insights throughout my research, aiding in the refinement of paper drafts and facilitating the publication process. All co-authors have granted consent for the incorporation of the published papers in this thesis.

ACKNOWLEDGEMENTS

Firstly, I want to sincerely thank my parents for their wholehearted support, both emotionally and financially. It is because of their support that I was able to persevere and complete my doctoral degree.

Secondly, I want to express special gratitude to my supervisors, Professor Lin Ma, Professor Derek B. Ingham, and Professor Mohamed Pourkashanian. Professor Lin Ma not only provided me with meticulous guidance in my research, but also set a great example in nurturing students. Especially during my second year, facing an eight-month period of stagnation on employing the resistance model, Professor Ma's weekly meetings and discussions helped me overcome this challenge. In addition, Professor Derek B. Ingham has been a steadfast supporter throughout my academic journey. He patiently assisted me in revising multiple rounds of papers and thesis, consistently showing concern for my well-being. Professor Mohamed Pourkashanian always offered encouragement with his warm smile and kind words. If I become a researcher or supervisor in the future, I aspire to follow in their footsteps, dedicating myself to research and emulating their dedication, passion, and generosity in mentoring students, just as they have done for me.

Thirdly, I would like to extend my thanks to my friends Tian Jinbei and Peng Wenjun. Their company during my doctoral journey filled it with laughter, joy, and enriching experiences. Wishing them successful graduation.

Lastly, I would like to dedicate my thesis to my grandparents, who raised me into adulthood. In heaven, I wish they are proud of me.

PUBLICATIONS AND PRESENTATIONS

Journal papers

Zhang, G., Ingham, D., Ma, L., & Pourkashanian, M. Modelling of 3D liquid dispersion in a rotating packed bed using an Eulerian porous medium approach. *Chemical Engineering Science*, 2022; 250: 117393. (DOI: 10.1016/j.ces.2021.117393)

Zhang, G., Ma, L., & Pourkashanian, M. A porous medium approach to the 3D modelling of an entire rotating packed bed for post-combustion carbon capture. *Chemical Engineering Science*, 2023; 274: 118687. (DOI: 10.1016/j.ces.2023.118687)

Zhang, G., Ingham, D., Ma, L., & Pourkashanian, M. Critical comparison between the large-scale rotating packed bed and conventional packed bed for post-combustion carbon capture. *Industrial & Engineering Chemistry Research*, 2023; (under review).

Wu, C., ..., **Zhang, G.**, Ma, L., ... A comprehensive review of carbon capture science and technologies. *Carbon Capture Science and Technology*, 2023; (under review).

Oral presentations

Zhang, G., Ingham D., Ma L., Pourkashanian M. A critical comparison between the rotating packed bed and conventional packed bed for post-combustion carbon capture. ROTOR colloquium, 5-6 October 2023, Berlin, Germany.

Zhang, G., Ingham D., Ma L., Pourkashanian M. A critical comparison between the rotating packed bed and conventional packed bed for post-combustion carbon capture.

The 2nd Fuel and Energy Research Forum Conference, 4-6 September 2023, Sheffield,
UK

Poster presentations

Zhang G., Ma L., Ingham D., Pourkashanian M. 3D modelling of a full rotating packed bed for carbon capture using porous medium approach. UKCCSRC Spring Conference, 28-29 March 2023, Cardiff, UK

Zhang G., Ma L., Ingham D., Pourkashanian M. Comparison between the rotating packed bed and conventional packed bed for post-combustion carbon capture. UKCCSRC Knowledge Exchange Conference, 6-7 September 2023, Sheffield, UK

ABSTRACT

The rotating packed bed (RPB) has shown promising advantages for post-combustion carbon capture (PCC), such as its high mass transfer rate and compact structure. However, there is limited understanding of the hydrodynamics and mass transfer performance within the RPB, including the liquid dispersion in the packing region, CO₂ capture in the outer cavity zone, etc., when comparing with the conventional packed bed (CPB). This is largely because there is not an appropriate computational method that can simulate the fluid flows and the carbon capture processes in a full scale RPB in 3D due to the multiscale of the problem. These restrict the commercial application of the RPB technologies.

The objectives of this thesis is to effectively investigate the hydrodynamics and mass transfer in the multi-scale RPB by employing the Eulerian porous medium approach and developing associated necessary process specific sub-models. The liquid dispersion and CO₂ capture processes are respectively studied in a lab-scale and a pilot-scale RPB, and the CO₂ capture performance in the RPB is compared with CPB.

Firstly, a 3D Eulerian porous medium model is established coupled with the appropriate interfacial, drag and dispersion forces formulations for investigating the effect of the liquid dispersion in a practical lab-scale RPB. The sensitivity of the parameters employed in these formulations is thoroughly analyzed. New forms of the porous resistance model and the effective interfacial area correlation are developed for the non-uniform two-phase flows. The simulation results show that the effect of the capillary pressure and mechanical dispersion forces on the liquid flow distribution and holdup in the RPB is clear and important. In addition, increasing the number of the liquid nozzles

from 1-4 could improve the liquid distribution and liquid holdup in the packing region substantially.

Secondly, a full 3D CFD model, including the packing and the inner and outer cavity zones, is established based on a pilot-scale RPB, employing the Eulerian porous medium method. The CO₂ capture processes, including the hydrodynamics, thermodynamics, and mass transfer, are examined within the entire RPB. The CO₂ capture performance in the packing and outer cavity zones has been quantitatively analyzed under different operating conditions. The simulation results show good agreement with the experimental data, and the contribution of the outer cavity zone to the CO₂ capture of the RPB is in the range of 28 %-42 % in this established RPB.

Thirdly, a large-scale RPB is established computationally according to a design procedure and the experimental parameters from a CPB pilot plant. The CO₂ capture processes in the RPB are effectively and extensively investigated by employing the Eulerian porous medium method and various sub-models developed. Furthermore, the RPB and CPB have been critically compared under different operating conditions. The simulation results show that compared with the CPB, the liquid flow rate could be saved by 40% when using a 50% MEA concentration solution instead of 30%, and the volume of the packed bed in the RPB could be reduced by 80%.

This thesis provides a new and effective approach to simulate the hydrodynamics and CO₂ capture processes in full-scale RPBs, and it also provides important information for the scaling up and operation of RPBs for PCC, highlighting the important potential of RPBs for industrial applications.

CONTENTS

DECLARATION	III
ACKNOWLEDGEMENTS.....	V
PUBLICATIONS AND PRESENTTIONS	VII
ABSTRACT	IX
CONTENTS.....	XI
LIST OF FIGURES	XVII
LIST OF TABLES.....	XXI
NOMENCLATURE	XXIII
CHAPTER 1 : INTRODUCTION.....	1
1.1 Research background	1
1.2 Conventional PCC process	2
1.3 Rotating packed bed for PCC	4
1.4 Research motivation.....	6
1.5 Thesis structure	10
1.5.1 Research aims	10
1.5.2 Novelties	11
1.6 Scope and outline of the thesis.....	12
1.6.1 Scope of the thesis	12
1.6.2 Outline of the thesis	14
CHAPTER 2 : LITERATURE REVIEW	17
2.1 Packing region	17
2.1.1 Flow dynamics.....	18
2.1.1.1 <i>Flow patterns</i>	18
2.1.1.2 <i>Liquid holdup</i>	20
2.1.1.3 <i>Liquid film thickness and droplet diameter</i>	23

2.1.1.4	<i>Gas pressure drop</i>	26
2.1.2	Mass transfer.....	28
2.1.2.1	<i>Effective interfacial area</i>	28
2.1.2.2	<i>CO₂ capture based on mass transfer correlations</i>	30
2.1.2.3	<i>Theory for the mass transfer</i>	32
2.2	Outer cavity zone	34
2.2.1	Flow dynamics.....	34
2.2.1.1	<i>Visual studies</i>	34
2.2.1.2	<i>Droplet diameter</i>	35
2.2.2	Mass transfer.....	36
2.3	CFD simulations	38
2.3.1	Single-phase flow behaviours.....	38
2.3.2	Multi-phase flow characteristics.....	39
2.3.2.1	<i>VOF method and its limitations</i>	39
2.3.2.2	<i>Eulerian method and its challenges</i>	43
2.3.2.3	<i>Mass transfer performance</i>	47
2.4	Comparison between RPB and CPB.....	50
2.5	Knowledge gaps.....	53
CHAPTER 3 : THEORIES AND METHODOLOGIES.....		57
3.1	Governing fluid flow equations	58
3.2	Liquid outlet setting methods.....	60
3.3	Porous resistance force and interfacial force models.....	61
3.3.1	Porous resistance in the packing region.....	62
3.3.2	Interfacial force in the outer cavity zone	66
3.4	Dispersion force models	67
3.4.1	Capillary pressure	68
3.4.2	Mechanical dispersion	69
3.5	Gas-liquid effective interfacial area models	71

3.5.1	Effective interfacial area in the packing zone.....	71
3.5.2	Effective interfacial area in the outer cavity zone.....	72
3.6	Mass transfer model.....	74
3.7	Chemical reaction rate	78
3.8	Heat transfer model.....	79
3.9	Conclusion	81
CHAPTER 4 : LIQUID DISPERSION IN A 3D RPB MODEL USING AN EULERIAN POROUS MEDIUM APPROACH.....		85
4.1	Introduction.....	85
4.2	CFD modelling.....	87
4.2.1	Geometry of the RPB.....	87
4.2.2	Assumptions for the model.....	88
4.2.3	Solution procedure.....	89
4.2.4	Boundary conditions.....	90
4.2.5	Mesh independence	90
4.3	Results and discussion	91
4.3.1	Validation and the liquid holdup along the radial direction.....	91
4.3.2	Sensitivity of the simulation results to the dispersion force model.....	97
4.3.2.1	<i>Capillary pressure model</i>	97
4.3.2.2	<i>Spread factor in the dispersion force model</i>	99
4.3.3	Effect of the operational and design parameters on the dispersion force	102
4.3.3.1	<i>The effect of liquid flow rate</i>	102
4.3.3.2	<i>Effect of the rotational speed and packing porosity</i>	105
4.3.3.3	<i>Effect of the nozzle size and number of nozzles</i>	106
4.4	Comments on the time efficacy of the new Eulerian model.....	109
4.5	Conclusions.....	109
CHAPTER 5 : CO₂ CAPTURE IN AN ENTIRE 3D RPB MODEL USING AN EULERIAN POROUS MEDIUM APPROACH.....		113

5.1	Introduction.....	114
5.2	CFD modelling.....	115
5.2.1	Geometry of the RPB.....	115
5.2.2	Assumptions for the model.....	118
5.2.3	Properties of the fluids and boundary conditions.....	119
5.2.4	Solution procedure.....	121
5.2.5	Grid independence.....	122
5.3	Results and discussion.....	123
5.3.1	Validation and the distribution of variables.....	123
5.3.2	Mass transfer in different zones in the RPB.....	130
5.3.3	Effect of the operating parameters.....	133
5.3.3.1	<i>Effect of the MEA concentration.....</i>	<i>134</i>
5.3.3.2	<i>Effect of the liquid flow rate.....</i>	<i>136</i>
5.3.3.3	<i>Effect of the rotational speed.....</i>	<i>138</i>
5.4	Conclusions.....	140

CHAPTER 6 : CRITICAL COMPARISON BETWEEN THE LARGE-SCALE RPB AND CPB FOR PCC 143

6.1	Introduction.....	143
6.2	Design procedure for the RPB.....	147
6.2.1	Inner packing radius.....	147
6.2.2	Packing width.....	148
6.2.3	Outer packing radius.....	149
6.2.4	Other parameters.....	150
6.3	CFD modelling.....	151
6.3.1	Geometry of the RPB.....	151
6.3.2	Assumptions for the model.....	152
6.3.3	Solution procedure.....	152
6.3.4	Boundary conditions.....	153

6.3.5	Grid independence	155
6.4	Results and discussion	155
6.4.1	Comparison between the CPB and RPB with various rotational speeds	156
6.4.2	Comparison between the CPB and RPB under various flow rates	159
6.4.3	Comparison between the CPB and RPB under various MEA concentrations	162
6.5	Comments on the use of the RPB for post-combustion CO ₂ capture	164
6.6	Conclusions.....	165
CHAPTER 7 : CONCLUSIONS AND FUTURE WORK		167
7.1	Conclusions.....	167
7.1.1	Liquid dispersion in the RPB.....	167
7.1.2	CO ₂ capture processes in the RPB.....	169
7.1.3	Comparison between the RPB and CPB for PCC	171
7.1.4	Overall conclusion	172
7.2	Future work.....	174
REFERENCE		177

LIST OF FIGURES

Figure 1-1 Simplified diagram of the carbon capture process using CPBs [10]...3

Figure 1-2 Schematic of a typical RPB with a single block counter-current flow arrangement.....5

Figure 2-1 Schematic of the flow patterns within (a) the wire mesh packing [46]; (b) the foam packing [20]. 19

Figure 2-2 Comparison of the simulated and visualized liquid flow across the rotating (a) single-layer wire mesh [32]; (b) multi-layer wire mesh packing [53]..... 19

Figure 2-3 Schematic diagram of the RPB experimental rig (a) [43]; (b) [96]; and (c) [44].37

Figure 2-4 (a) Schematic diagram of the physical 2D RPB model; contours of the (b) CO₂ mass fraction in the gas phase; and (c) liquid temperature for 30% MEA and 90% MEA [6].50

Figure 3-1 The calculation procedure for the porous resistance.66

Figure 3-2 The calculation procedure for the mass transfer.78

Figure 3-3 The sub-models employed in Chapter 4.....82

Figure 3-4 The sub-models employed in Chapter 5.....82

Figure 3-5 The sub-models employed in Chapter 6.....83

Figure 4-1 Schematic diagram of the 3D RPB and corresponding size (1, outer cavity zone; 2, packing zone; 3, inner cavity zone; 4, pressure outlet; 5, symmetry; 6, liquid inlet; 7, pressure outlet, Z - axis is the axis of rotation).88

Figure 4-2 Schematic of the mesh in the 3D model.....	91
Figure 4-3 (a) Map of liquid holdup from the experiment [64]; contours of (b) liquid holdup from the simulation; and (c) fractional effective interfacial area from the simulation.	93
Figure 4-4 Comparison of the experimental data [64] and the simulation results for the liquid holdup (a) along the radial direction; (b) under different rotational speeds; and (c) velocity components along the radial direction..	96
Figure 4-5 Contours of the liquid holdup on the planes (a) $x = 0$ and (b) $y = 0$.	97
Figure 4-6 The effect of the capillary pressure models on the liquid holdup.	99
Figure 4-7 The effect of the correlations for the spread factor on the liquid holdup.	101
Figure 4-8 The effect of the liquid flow rate on the liquid holdup under different rotational speeds: (a) 500 rpm and (b) 1000 rpm.....	103
Figure 4-9 The holdup up and fractional effective interfacial area on the symmetric plane before employing the dispersion force with different liquid flow rates: (a) ε_L , 23 cm ³ /s; (b) ε_L , 43 cm ³ /s; (c) f_e , 23 cm ³ /s; and (d) f_e , 43 cm ³ /s.....	104
Figure 4-10 The holdup up and fractional effective interfacial area on the symmetric plane after employing the dispersion force with different liquid flow rates: (a) ε_L , 23 cm ³ /s; (b) ε_L , 43 cm ³ /s; (c) f_e , 23 cm ³ /s; and (d) f_e , 43 cm ³ /s.....	104
Figure 4-11 The effect of the (a) rotational speed; and (b) packing porosity on the liquid holdup.	106
Figure 4-12 The effect of the (a) nozzle length; (b) nozzle width; and (c) number of nozzles, on the liquid holdup.....	108

Figure 4-13 The distribution of the liquid holdup on the symmetric cross-sectional surface.	109
Figure 5-1 Schematic diagram of the 3D RPB (1, gas outlet; 2, case; 3, gas inlet; 4, liquid elimination zone; 5, liquid inlet; 6, outer cavity zone; 7, packing zone; 8, inner cavity zone).	118
Figure 5-2 (a) Schematic of the mesh in the 3D model and (b) predicted CO ₂ capture rate and liquid outlet temperature using different grids.	123
Figure 5-3 Comparison of the (a) CO ₂ mole fraction in the gas outlet; (b) liquid outlet temperature [161].	125
Figure 5-4 Vectors of the (a) liquid velocity; (b) gas velocity; contours of the (c) liquid holdup; (d) effective interfacial area on the planes $z = 0.01$; (e) CO ₂ fraction in the gas phase; (f) liquid temperature on the planes on the planes $z = 0.01$; (g) CO ₂ fraction in the gas phase; and (h) liquid temperature on the planes $y=0$ for 30% and 70 % MEA.	129
Figure 5-5 The circumferentially averaged (a) liquid holdup and effective interfacial area; (b) liquid and rotating packing velocities and (c) CO ₂ mole fraction in the gas phase and liquid temperature along the radial direction.	133
Figure 5-6 The effect of the MEA concentration on (a) $K_L a_e$ and the liquid outlet temperature and (b) ratio of the contribution of CO ₂ capture and mass transfer area in the outer cavity zone.	136
Figure 5-7 The effect of the L/G ratio on (a) $K_L a_e$ and liquid outlet temperature and (b) ratios of the contribution of CO ₂ capture and mass transfer area in the outer cavity zone.	138
Figure 5-8 The effect of the rotational speed on the (a) $K_L a_e$ and liquid temperatures at the liquid outlet and outer packing boundary and (b) ratios of	

the contribution of CO ₂ capture and mass transfer area in the outer cavity zone.	140
Figure 6-1 Schematic diagram of the 2D RPB ((1, packing; 2, liquid inlet; 3, gas inlet; 4, liquid elimination zone; 5, gas outlet).	152
Figure 6-2 (a) The predicted CO ₂ capture rate with different grids, and (b) schematic of the mesh in the 2D model.	155
Figure 6-3 The (a) CO ₂ capture rate and (b) liquid outlet temperature under various rotational speeds.	158
Figure 6-4 The distributions of the (a) liquid holdup; (b) effective interfacial area; (c) CO ₂ fraction in the gas phase; (d) MEA mass fraction; (e) liquid specific heat; and (f) liquid temperature for 300 and 800 rpm.	159
Figure 6-5 The (a) CO ₂ capture rate and (b) liquid outlet temperature under various rotational speeds and liquid flow rates.	162
Figure 6-6 The MEA fraction in the liquid phase when the liquid flow rate ratios are (a) 0.6; (b) 0.7; and (c) 0.9 for 600 rpm.	162
Figure 6-7 The CO ₂ capture rate under various rotational speeds and MEA concentrations.	164
Figure 6-8 The CO ₂ capture rate under various MEA concentrations and liquid ratios for 300 rpm.	164

LIST OF TABLES

Table 2-1 The number of meshes number used in the models.....	20
Table 2-2 Correlations for the prediction of the (fractional) effective interface area in the packing region.	29
Table 2-3 Summary of the dimensions and operating conditions of the rotating packed bed for comparison.	53
Table 3-1 Some of the correlations utilized in the current study.	76
Table 4-1 The operational conditions employed in the experiments [64].....	90
Table 5-1 The operational conditions of the experiments [161].	116
Table 5-2 The mole fraction of each component in the gas phase.	119
Table 5-3 The mass fraction of each component in the MEA solutions.	120
Table 5-4 The viscosity and surface tension of the MEA solutions [185, 186].	120
Table 5-5 The operational conditions for the baseline case.	133
Table 6-1 The experimental data from the CO ₂ capture plant using CPBs in the PACT facilities [196].	146
Table 6-2 The information of the large-scale RPB model.	151
Table 6-3 The mole fraction of each component in the gas phase.	154
Table 6-4 Mass fraction of the each components in the 30% MEA solutions. .	154

NOMENCLATURE

Abbreviations

CFD	Computational Fluid Dynamics
CPB	Conventional Packed Bed
HSM	Hydrophobic Surface-Modified
HTU	Height of Transfer Unit
IMTP25	INTALOX Metal Tower Packing
IPCC	Intergovernmental Panel on Climate Change
PACT	Pilot-scale Advanced Capture Technology
PCC	Post-combustion Carbon Capture
PI	Process Intensification
REU	Representative Elementary Unit
RPB	Rotating Packed Bed
TERC	Translational Energy Research Centre
UDF	User Defined Functions
UKCCSRC	UK Carbon Capture and Storage Research Centre
VOF	Volume of Fluid

Roman alphabet

a_s	specific area of the dry packing materials, $m^2 \cdot m^{-3}$
a'_s	specific area of the wet packing materials, $m^2 \cdot m^{-3}$
A_e	effective interfacial area, $m^2 \cdot m^{-3}$
C	mass concentration, $kg \cdot m^{-3}$
C_{pG}	specific heat of gas phase, $J \cdot kg^{-1} \cdot K^{-1}$
C_D	drag coefficient
d_{min}	characteristic diameter, m
d_p	liquid droplet diameter, m

d_w	diameter of the wire mesh, m
d'_w	diameter of the wet wire mesh, m
D	diffusivity, $\text{m}^2 \cdot \text{s}^{-1}$
D_h	hydraulic diameter, m
D_i	inner packing diameter, m
D_o	outer packing diameter, m
E	enhancement factor
E'_i	total energy, J
f, f^*	drag function
f_d	volume ratio of the inner cavity zone occupied by the liquid distributor
f_e	ratio of effective interfacial area to the total packing surface area
f_l	laminar fanning factor
f_t	turbulent fanning factor
F	pressure factor
$\vec{F}_{disp,i}$	dispersion forces of phase i , $\text{N} \cdot \text{m}^{-3}$
$\vec{F}_{drag,i}$	interaction force between phase i and solids of the packing material, $\text{N} \cdot \text{m}^{-3}$
$\vec{F}_{D,i}$	mechanical dispersion force for phase i , $\text{N} \cdot \text{m}^{-3}$
\vec{F}_{GL}	interfacial force between the gas and liquid phases, $\text{N} \cdot \text{m}^{-3}$
\vec{g}	gravitational force, $\text{m} \cdot \text{s}^{-2}$
g_c	centrifugal acceleration, $\text{m} \cdot \text{s}^{-2}$
g_1	characteristic centrifugal acceleration, $\text{m} \cdot \text{s}^{-2}$
h	height of the packing, m
h_j	enthalpy of the species, $\text{J} \cdot \text{mol}^{-1}$
h_{GL}	heat transfer coefficient between the gas and liquid phases, $\text{W} \cdot \text{m}^{-2} \cdot \text{K}^{-1}$
H	Henry constant, $\text{Pa} \cdot \text{m}^3 \cdot \text{mol}^{-1}$

\vec{j}	mass diffusion flux, $\text{kg} \cdot \text{m}^{-2} \cdot \text{s}^{-1}$
k_b	reaction rate constant, $\text{m}^3 \cdot \text{mol}^{-1} \cdot \text{s}^{-1}$
k'_{eff}	effective thermal conductivity, $\text{W} \cdot \text{m}^{-1} \cdot \text{K}^{-1}$
k'_F	thermal conductivity of fluid, $\text{W} \cdot \text{m}^{-1} \cdot \text{K}^{-1}$
k_i	mass transfer coefficient of phase i , $\text{m} \cdot \text{s}^{-1}$
k'_S	thermal conductivity of the packing, $\text{W} \cdot \text{m}^{-1} \cdot \text{K}^{-1}$
k_2	reaction rate constant, $\text{m}^3 \cdot \text{mol}^{-1} \cdot \text{s}^{-1}$
K_L	overall mass transfer coefficient, $\text{m} \cdot \text{s}^{-1}$
K_{iS}	porous resistance coefficient between phase i and solid, $\text{kg} \cdot \text{s}^{-1}$
K_{GL}	momentum exchange coefficient between the gas and liquid phases, $\text{kg} \cdot \text{s}^{-1}$
$K_L a_e$	overall volumetric mass transfer coefficient, s^{-1}
L	packing length, m
L_e	effective flow length of packing, m
M	molar mass, $\text{g} \cdot \text{mol}^{-1}$
N_g	ratio of the centrifugal to gravitational acceleration
p	kinetic energy ratio of the liquid jet to the exit gas
P	pressure, Pa
P_c	capillary pressure, Pa
q	dimensionless liquid initial velocity
Q_i	volume flow rate, $\text{m}^3 \cdot \text{s}^{-1}$
$Q_{h,GL}$	transferred heat between the gas and liquid phases, $\text{W} \cdot \text{m}^{-3}$
r	radius or radial distance, m
r_c	ratio of CO ₂ capture in the outer cavity zone to the entire RPB
r_{CO_2}	CO ₂ capture rate, %
r'_{CO_2}	CO ₂ reaction rate, $\text{kg} \cdot \text{m}^{-3} \cdot \text{s}^{-1}$
r_e	ratio of mass transfer area in the outer cavity zone to the entire RPB

r_i	inner packing radius, m
r_o	outer packing radius, m
R	gas constant, $\text{J} \cdot \text{K}^{-1} \cdot \text{mol}^{-1}$
R_{ij}	net rate of production of the species j by the reaction, $\text{mol} \cdot \text{m}^{-3} \cdot \text{s}^{-1}$
S_f	spread factor
$S_{m,i}$	mass transfer rate between gas and liquid, $\text{kg} \cdot \text{m}^{-3} \cdot \text{s}^{-1}$
$S_{h,i}$	heat of chemical reaction, $\text{J} \cdot \text{mol}^{-1}$
S_H	energy source, $\text{W} \cdot \text{m}^{-3}$
S_j	species source, $\text{kg} \cdot \text{m}^{-3} \cdot \text{s}^{-1}$
S_M	mass source, $\text{kg} \cdot \text{m}^{-3} \cdot \text{s}^{-1}$
\vec{S}_U	momentum source, $\text{N} \cdot \text{m}^{-3}$
t	time, s
T_i	temperature of phase i , K
u	flow rate per unit area, $\text{m} \cdot \text{s}^{-1}$
u_e	effective velocity, $\text{m} \cdot \text{s}^{-1}$
\vec{u}_i	velocity of phase i , $\text{m} \cdot \text{s}^{-1}$
u_0	superficial velocity, $\text{m} \cdot \text{s}^{-1}$
U	average superficial liquid velocity, $\text{m} \cdot \text{s}^{-1}$
U_G	superficial gas velocity near flooding, $\text{m} \cdot \text{s}^{-1}$
U_1	characteristic flow rate per unit area, $\text{m} \cdot \text{s}^{-1}$
$\vec{v}_{D,i}$	drift velocity of phase i , $\text{m} \cdot \text{s}^{-1}$
\vec{v}_e	effective velocity relative to the rotating packing, $\text{m} \cdot \text{s}^{-1}$
\vec{v}_i	local velocity of phase i relative to the rotating packing, $\text{m} \cdot \text{s}^{-1}$
v_{jet}	liquid jet velocity, $\text{m} \cdot \text{s}^{-1}$
V	volume, m^3
Δx	radial length of a cell, m
y_{i,CO_2}	CO ₂ mole fraction in the gas inlet

y_{o,CO_2}	CO ₂ mole fraction in the gas outlet
y_{op,CO_2}	CO ₂ mole fraction on the outer packing surface,
Y_{ij}	mass fraction of species j in phase i

Greek alphabet

α	phase saturation
γ	packing void fraction (porosity)
β	dynamic contact angle, °
β_1	characteristic dynamic contact angle, °
\mathcal{X}^+	dimensionless channel length
ε	volume fraction
δ	diffusion layer thickness, m
ω	angular velocity, rad · s ⁻¹
κ_G	thermal conductivity of the gas phase, W · m ⁻¹ · K ⁻¹
θ	angle of flow direction slop to the bed axis, °
φ	flooding correlation fitting parameter
ρ_i	density of phase i , kg · m ⁻³
$\Delta\rho_{GL}$	density difference between liquid and gas phases, kg · m ⁻³
μ	dynamic viscosity, kg · m ⁻¹ · s ⁻¹
μ_e	effective dynamic viscosity, kg · m ⁻¹ · s ⁻¹
τ	tortuosity factor
τ_L	particulate relaxation time, s
$\bar{\tau}$	stress tensor, N · m ⁻²
$\bar{\tau}_{eff,ij}$	effective shear tensor
λ_{RT}	Rayleigh-Taylor instability wavelength
σ	surface tension, N · m ⁻¹
ν	kinematic viscosity, m ² · s ⁻¹

ν_1	characteristic kinematic viscosity, $\text{m}^2 \cdot \text{s}^{-1}$
---------	--

Subscripts

<i>cell</i>	mesh cell
CO_2	carbon dioxide
<i>F</i>	fluid
<i>G</i>	gas phase
<i>i</i>	phase G or L
<i>j</i>	species
<i>L</i>	liquid phase
<i>MEA</i>	monoethanolamine
N_2O	nitrous oxide
<i>O</i>	outer cavity zone
<i>OW</i>	computational cell next to the casing wall
<i>P</i>	packing zone
<i>PW</i>	computational cell next to the packing wall
<i>S</i>	solids phase for the packing materials
<i>w</i>	water

Dimensionless Groups

<i>Ha</i>	Hatta number
<i>Nu</i>	Nusselt number
<i>Pr</i>	Prandtl number
<i>Re</i>	Reynold number
<i>Re'</i>	relative Reynold number
<i>We</i>	Webber number

CHAPTER 1 : INTRODUCTION

Summary

This chapter begins with an introduction of the research background, including the serious issues of CO₂ emissions and the reasons for CO₂ capture. Then, a description of the post-combustion carbon capture (PCC) technology using a conventional packing bed (CPB) is introduced. In addition, the potential of employing a rotating packed bed (RPB) as the process intensification (PI) equipment in the context of PCC is introduced, which is the research objective of this thesis. Also, the research motivation, research aims, novelties, and structure of the thesis are presented.

1.1 Research background

Greenhouse gas emissions, mainly carbon dioxide, have become an urgent issue in the 21st century, leading to the temperature continuously increasing in the Earth's atmosphere. The current concentration of CO₂ in the air has increased by about 1.5 times compared with the levels of the pre-industrial revolution and with a growth rate of about 2.2% per year [1]. As a result, the Earth's temperature has risen by 0.18 °C per decade since 1981 [2]. This continuous climate change has caused many problems, such as desertification, rising sea-level, as well as stronger extreme weather events. It is reported by the Intergovernmental Panel on Climate Change (IPCC) that the global greenhouse gas emissions must be reduced by 50-85% by 2050 and limit global

warming below 2 degrees [3]. The EU has a commitment for a net-zero greenhouse gas emissions target by 2050 [4], which aims to achieve a balance between the amount of greenhouse gas emissions produced and the amount removed from the atmosphere [5]. Therefore, reducing CO₂ emissions has become an emergency activity.

The worldwide power plants contribute a huge amount of CO₂, which could be up to 30% of the total CO₂ emissions [6]. It has been noted that a 500 MWe supercritical coal-fired power plant, operating at an efficiency of 46%, releases more than 8,000 tonnes of pure CO₂ per day which is a huge volume [7]. Although other methods and renewable resources, such as solar, wind, and tidal, have been utilized in generating electricity, the cost and their limits restrict their use in electricity generation. Thus, employing fossil fuel power stations will continue to play a critical role in generating electricity for many years to come. Accordingly, the CO₂ released by the power stations is required to be captured.

1.2 Conventional PCC process

At present, there are mainly three basic kinds of CO₂ capture systems for the use of fossil fuels: post-combustion carbon capture (PCC), pre-combustion carbon capture, oxy-fuel combustion carbon capture. In particular, PCC based on the amine solvents is the most mature and commercial way to reduce CO₂ emissions from power plants [8, 9] because of its fast reaction rate, considerable gas throughput, as well as the flexibility to retrofit the existing power plants.

A typical amine-based CO₂ capture process is shown in Figure 1-1 [10]. The conventional packed beds (CPBs) are usually employed as the absorber and desorber – the two most important units in the CO₂ capture system. In the absorber, the CO₂ in the

raw gas feeding from the bottom counter-current contacts and reacts with the amine solvent flowing down from the top. Then, the treated gas will be released into the air at the top of the absorber and the rich amine solvent (the CO₂ absorbed solution) passes through heat exchanger and enters the desorber to regenerate. In the desorber, the high-temperature steam produced by the reboiler flows upward and the CO₂ will be separated. The obtained lean solvent is then pumped into the absorber and this begins the next round of the CO₂ capture process.

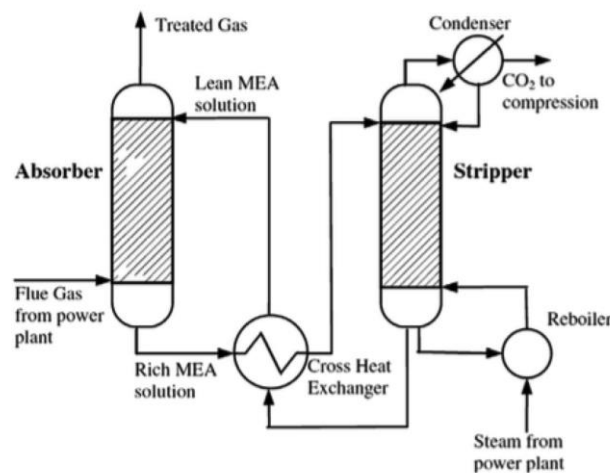


Figure 1-1 Simplified diagram of the carbon capture process using CPBs [10].

As mentioned above, the absorption unit (CPB), where the gas and liquid react, is one of the most important units in the amine-based CO₂ capture system. The absorber can directly affect the gas-liquid mass transfer and chemical reaction rate. Generally, the huge amount of raw gas needs to be treated in the CPB, which results in the large absorber size and the expensive capital cost. For example, Lawal et al. [7] reported that two absorbers with a packing height of 17 m and 9 m in diameter will be required to remove CO₂ from the flue gas of a 500 MWe sub-critical coal-fired power plant. In addition, the high amine solvent flow rate demanded by the large CPB would consume

large heat energy for the rich solvent regeneration, which leads to a reduction in the power generation efficiency by up to 13% [11]. Although it has been proved that employing higher concentrated solutions could reduce the solvent flow rate and have a larger absorption capacity [12], the high-concentrated amine solution with a high viscosity is rarely used in the CPB because of its severe corrosion and poor liquid dispersion performance. Also, the liquid misdistribution could form in the gravity field when the liquid flows downward, thus causing a smaller gas-liquid contact area and a poor mass transfer performance. Hence, some effort should be put into overcoming these issues, including the high energy consumption, the very poor gas-liquid contact behaviour as well as the huge facility size.

1.3 Rotating packed bed for PCC

Process intensification (PI) has been attracting considerable attention owing to the centrifugal force resulting from a high gravitational environment (100-1000 times gravity) [13]. The rotating packed bed (RPB), one of the most important applications in the topic of PI, has the potential to enhance the CO₂ capture performance. Generally, the RPB may be divided into three main parts from the inside to outside - inner cavity, packing and outer cavity zones, see Figure 1-2. At the beginning, the liquid jets out from the liquid distributor and passes through the inner cavity zone entering the packing region with only a radial velocity. Then it hits against with the rotating porous packing violently and the liquid is quickly dispersed, some of the liquid is attached to the packing surface and some eventually splits into numerous tiny droplets. This process forms a large effective interfacial area (m^2/m^3) between the gas and liquid phases and renews them quickly [14]. The mixing at the inner packing is very strong, which is called the “end-effect” zone [15, 16]. After that, the liquid achieves its tangential

velocity, and its motion becomes largely synchronized with the rotating packing in the rest of the packing region [17]. As a result, the liquid dispersion and mass transfer coefficient are relatively weak compared with that in the end-effect zone [18], which indicates that the liquid dispersion plays an important role in determining the liquid flow behaviour in the RPB and it is the predominant reason for the enhancement of the mass transfer in RPBs. After that, the liquid leaves the packing with a large tangential velocity and enters the outer cavity zone in the form of liquid droplets. Finally, the liquid droplets hit the cavity casing wall and the liquid phase flows out from the liquid outlet tube under the influence of the gravitational force. It should be noted that before the liquid leaves the outlet tube, the liquid has been reacting with the gas phase all the time in the RPB, thus indicating that the CO₂ capture in the RPB occurs not only in the packing zone, but also in the outer cavity zone.

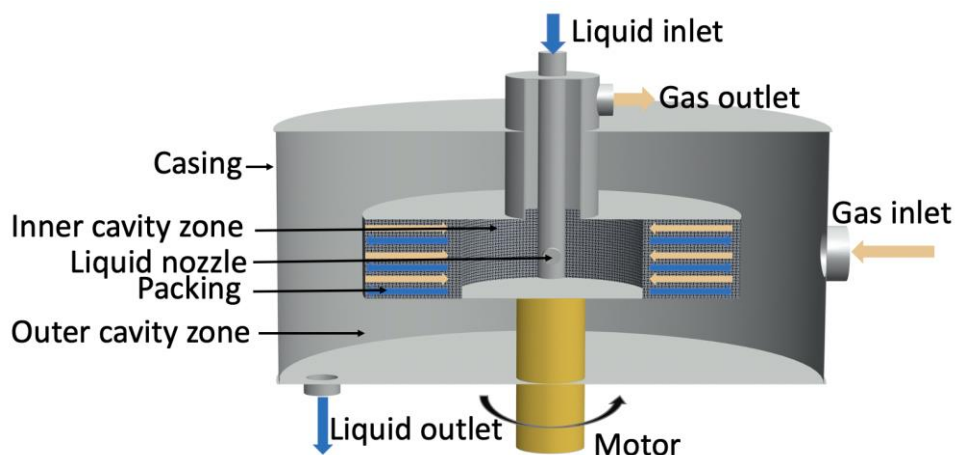


Figure 1-2 Schematic of a typical RPB with a single block counter-current flow arrangement.

When passing through the packing region, the liquid forms small droplets and thin films, which can enhance the effective interfacial area and the micromixing [19]. In addition,

the surface renewal of the phases (such as gas-liquid, liquid-liquid, gas-liquid-solid) in the packing is improved, which also results in a significant increase in the CO₂ capture. Compared with the CPBs, the use of RPBs remarkably increases the mass transfer efficiency by 1-3 orders of magnitude [13]. Furthermore, high amine concentration solutions with large viscosities could be used in the RPB because of the high centrifugal force, leading to a lower liquid flow rate and smaller regeneration energy consumption. In this case, this could clearly reduce the size of the RPB, which also means lower capital costs and a smaller footprint [16, 20, 21]. Also, in the packing region with a large centrifugal force, the liquid maldistribution could be avoided, and the contact area between the gas and liquid phases can be guaranteed even under the shaking and thrashing conditions. Overall, compared with the CPB, the RPB has many advantages, including the higher mass transfer rate, cheaper capital cost, lower liquid holdup, etc. Thus, the RPB exhibits remarkable potential for removing CO₂ from the power plants.

1.4 Research motivation

Although the RPB has many advantages when compared with the CPB and has been employed in many industries, such as volatile organic compounds removal [22], it has rarely been commercially utilized for CO₂ capture [23]. One reason is the lack of the understanding of the flow dynamics and mass transfer processes in the RPB, especially the liquid dispersion in the packing region and the CO₂ capture in the outer cavity zone. The second reason is that the RPB's advantages over the CPB is unclear for PCC industrial application. Therefore, some work should be carried out to tackle these issues. In particular, an in-depth and thorough understanding of the hydrodynamics (liquid dispersion) as well as mass transfer within the entire RPB should be achieved. In addition, the CO₂ capture performance should be quantitatively compared in the large-

scale RPB and CPB, and some valuable instructions for operating the industrial-scale RPB should be provided.

The computational fluid dynamics (CFD) method has shown its advantages in measuring and evaluating important flow characteristics, such as the local flow velocity, which is difficult to be achieved by using the experimental method. In addition, employing the CFD method is more cost-effective and time-saving. Currently, the volume of fluid (VOF) method has been widely utilized to model the RPB [16, 19, 21, 24-33], which can clearly capture the gas-liquid contact surface. However, it can only be used for analyzing very small lab-scale RPB models and it will become computationally prohibitive for the simulations of large or 3D RPBs due to the limitations in the computational resources and simulation times [21, 31]. Alternatively, the Eulerian porous medium method, which treats the whole packing as a porous media instead of a complex matrix composed of numerous wire meshes, could significantly reduce the mesh number and simulation time required [6, 34-37]. Therefore, it is possible to simulate the 3D full-scale RPB using this method for the scaling up and process optimization. Nevertheless, the appropriate mathematical models need to be added to the governing equations and the accuracy of the RPB model depends on these sub-models employed, such as the models of the porous resistance, dispersion force, effective interfacial area, as well as mass and heat transfer. Thus, these models should carefully developed in this thesis.

Based on the fluid flow process within the RPB, it is known that the liquid dispersion, due to its interaction with the packing, plays an important role in determining the liquid flow behavior in the RPB, and it is the predominant reason for the enhancement of the mass transfer in RPBs. Liquid dispersion in the RPBs has been previously explored

both experimentally and computationally. For example, the dispersion phenomenon of a liquid jet impacting on the static and rotating single/multi-layer wire meshes has been visually examined under the effect of gravity and centrifugal force [14, 32, 38, 39]. In addition, the influence of the surface wettability and the liquid velocity, etc. on the liquid dispersion in the RPB have been analyzed in [18, 39-41]. However, the above studies were only at the stage of observing the phenomenon and the process of the dispersion in RPBs, and no one has evaluated and quantified the dispersion in a RPB. Thus, developing a dispersion force model that is suitable for the RPB is very important, especially when the Eulerian porous medium model are used, which employs some useful mathematical formulations for estimating the forces acting on the phases. Therefore, one of the objectives of this thesis is to develop the dispersion force models and to quantitatively investigate the effect of liquid dispersion.

According to Section 1.3, it is known that the CO₂ capture occurs in the entire RPB, not only in the packing zone, but also in the outer cavity zone. However, most investigations only focus on the packing region, and the contribution of the outer cavity zone to the CO₂ capture is rarely studied. In the experimental investigations, it has been reported that the mass transfer area of the outer cavity zone could be up to 30% of the entire mass transfer area [42, 43]. Furthermore, experiments showed that the contribution of the outer cavity zone to the mass transfer was determined to take up approximately 13-25% of the total mass transfer in the entire RPB [44, 45]. Therefore, the CO₂ absorption in the outer cavity zone cannot be ignored. However, no one has used the CFD method to investigate it. And the characteristics of the multiphase flow and mass transfer are very different in the rotating packing and static cavity space, which is quite complex. In addition, it is difficult to predict the contact area between gas and liquid in the outer

cavity zone because the liquid phase exists in the form of liquid droplets in the cavity space and liquid film on the casing wall. Therefore, the appropriate sub-models, such as the interfacial force model, effective interfacial model, liquid droplet diameter model, etc., for the packing and outer cavity zones should be separately and carefully developed for accurately analyzing the CO₂ capture in the entire RPB.

Although the RPB has many advantages over the CPB for the CO₂, it has rarely been commercially applied for PCC. The first reason is that the design procedures for the large-scale RPB have not yet been proposed for the CO₂ absorption. Even though the large-scale RPB has been constructed for industrial CO₂ capture, the operation of a CO₂ capture plant with an RPB absorber is another issue that required attention. Furthermore, the advantages of the RPB over the CPB has not been thoroughly and clearly established. To provide some valuable information for operating the RPBs and show the potential for the RPBs to be employed industrially for PCC, a large-scale RPB should be established and modelled under various operating conditions in this thesis.

Therefore, this thesis provides a feasible and effective approach to model 3D multiscale RPBs by employing the Eulerian porous medium model. The liquid dispersion in the packing region should be investigated and the dispersion force models would be developed. Through coupling with various sub-models, the CO₂ capture processes, including the hydrodynamics, thermodynamics, and mass transfer, should be effectively and accurately analyzed in the entire RPB (packing region and outer cavity zone). Furthermore, the CPBs and the RPBs need to be compared in the large-scale to evaluate the RPB's advantages and some valuable information would provide for the RPB scaling up and process optimizations.

1.5 Thesis structure

1.5.1 Research aims

The overall aim of this thesis is to develop RPB models to effectively and accurately investigate the hydrodynamics, thermodynamics, and mass transfer for paving the way for RPB scaling up and process optimizations, and to comprehensively compare the RPB and CPB for PCC.

The specific objectives of this research are as follows:

- To validate the hydrodynamics in the established RPB model and effectively investigate the flow dynamics in the RPB, especially the liquid dispersion in the packing region, by developing a 3D Eulerian model coupled with the dispersion force models.
- To explore the sensitivity of the parameters employed in the dispersion force models, including the capillary pressure and mechanical dispersion force models, as well as the effect of the dispersion forces on the flow dynamics under different design and operating parameters.
- To validate the CO₂ capture performance in the RPB model and predict the CO₂ capture efficiency within the whole RPB (mainly the packing and outer cavity zones) by employing a comprehensive 3D Eulerian model, which can successfully simulate the flow dynamics, mass transfer, chemical reaction, and heat transfer within the entire RPB.
- To separately develop the sub-models, such as the force and effective interfacial models, for the packing and outer cavity zones to quantitatively analyze the CO₂

capture process in different zones and evaluate the ratio of the CO₂ removal in the cavity zone to the whole RPB.

- To establish a large-scale RPB model with an outer diameter over 1 m and to perform the process optimization of the CO₂ capture processes under various operating conditions to provide some recommendations for the operation of RPBs for commercial application in PCC.
- To conduct a critical comparison between the CPB and the RPB in the field of CO₂ capture. Also, the advantages of deploying the RPB is to be clearly quantified in order to highlight the potential of RPBs for industrial applications.

1.5.2 Novelties

- A 3D Eulerian porous medium model has been established in order to investigate the hydrodynamics in a RPB, especially the influence of the liquid dispersion, which is coupled with the interfacial, drag and dispersion forces formulations. In this new model, the dispersion models have been employed for the first time to simulate the liquid dispersion in an entire packing region. In addition, new forms of the porous resistance model and the correlation for the effective interfacial area have been developed for the non-uniform gas-liquid two-phase flows. The simulation results demonstrate that the use of the Eulerian method can substantially reduce the simulation time and effort when compared to the VOF method. The developed model serves as the foundation for studying the CO₂ capture process in a full 3D RPB, paving the way for scaling up and optimizing the RPB technology.
- For effectively predicting the CO₂ capture within the RPB, a novel 3D entire RPB model, including the packing, inner and outer cavity zones, has been proposed by

using the aforementioned Eulerian model. The CO₂ capture processes, including the hydrodynamics, thermodynamics and mass transfer, could be thoroughly analyzed by incorporating with various sub-models, such as the models of the forces, effective interfacial area, heat transfer, mass transfer, etc. In specific, the effective interfacial area, force and even liquid droplet diameter models have been introduced separately for the packing region and the outer cavity zone to accurately predict the CO₂ capture performance inside the full RPB. The CO₂ absorption processes in these zones have been quantitatively evaluated under various operating conditions by the CFD method for the first time. The established model can accurately predict the CO₂ absorption in the RPB and provides a feasible way to effectively simulate a large full-scale RPB.

- In order to compare the CPB and RPB in terms of the CO₂ capture, a large-scale RPB model has been established by CFD method for the first time based on the design procedure and the practical experimental parameters from a CPB pilot plant. The process optimization has been performed in the large-scale RPB under various operating conditions. The CO₂ capture performance in the CPB and RPB has been quantitatively compared and the advantages of employing the RPB have been quantitatively analyzed. These findings provide some valuable insights for the RPB operation and highlight the potential for the RPB to be employed for PCC in the future.

1.6 Scope and outline of the thesis

1.6.1 Scope of the thesis

The thesis is focused on three main parts:

The first part of the thesis focuses on the analysis of the flow characteristics using a 3D Eulerian porous medium model based on a practical RPB. In order to investigate the liquid dispersion, the dispersion models (including the capillary pressure model and mechanical dispersion model) are developed, and the sensitivity of the parameters employed in these models has been analyzed. In addition, new forms of the porous resistance model and the correlation for the effective interfacial area are modified for the non-uniform gas-liquid two-phase flows. The model has been validated, and the effects of the dispersion force on the liquid holdup under different design and operational parameters, including nozzle design, liquid flow rate, rotational speed, etc., have been thoroughly examined. The effectiveness of using the Eulerian method is demonstrated, paving the way for RPB technology scaling-up and design optimization.

The second part of the thesis focuses on the CO₂ capture processes within an entire RPB, including the packing and outer cavity zones, through using a comprehensive 3D pilot-scale Eulerian model. Based on the sub-models developed for investigating the flow dynamics, mass transfer, chemical reaction and heat transfer models, the CO₂ capture processes and some important variables within the entire RPB are thoroughly explored. Due to the difference between the packing and outer cavity zones, the separate models for the forces and effective interfacial area for these zones are introduced for each zone. In addition, the CO₂ absorption that occurs in the packing and outer cavity zone is quantitatively evaluated. The model is validated with the experimental data and the effect of the operating parameters are investigated. This provides a feasible approach for accurately and effectively modelling the physical and chemical processes in a 3D full-scale and large-scale RPBs.

The third part of the thesis focuses on the simulation of a large-scale RPB and the

comparison between the CPB and the RPB for the CO₂ capture. A large-scale RPB has been established computationally according to the experimental parameters from a CPB pilot plant. The Eulerian porous medium method and various sub-models have been employed in order to effectively and extensively investigate the CO₂ capture processes in this large-scale RPB. In addition, the process optimization of the CO₂ capture has been quantitatively performed with employing various operating conditions. The advantages of applying the RPB over the CPB have been analyzed by comparing the required volume of the packed bed and the liquid flow rate. Also, some important suggestions for commercial deployment of the RPB has been introduced.

1.6.2 Outline of the thesis

This thesis is divided into seven chapters:

In Chapter 1, the research background of the thesis is discussed, along with the approaches for CO₂ capture using the RPB and CPB, as well as the motivations and aims of the research.

In Chapter 2, an extensive literature review focusing on the hydrodynamics and mass transfer is conducted, with a particular focus on RPB studies that have utilized CFD methods. In addition, a summary of the research gaps identified in the literature is presented.

In Chapter 3, the development of a comprehensive RPB model for effectively and comprehensively investigating the CO₂ capture processes is described, including the theories and methodologies employed in the process.

In Chapter 4, the obtained simulation results on the flow dynamics in a 3D Eulerian

RPB model are presented and discussed. The effect of the operating and design parameters on the liquid dispersion are analyzed.

In Chapter 5, the simulation results of the CO₂ capture performance within the entire RPB are discussed. The contribution of the outer cavity zone to the CO₂ capture of the RPB is evaluated under various conditions.

In Chapter 6, a large-scale RPB model is established and the critical comparison between the CPB, and the RPB under various operating conditions for the CO₂ removal is conducted.

In Chapter 7, the main conclusions are summarized and suggestions for future work are provided.

CHAPTER 2 : LITERATURE REVIEW

Summary

This chapter reviews the research works on the flow dynamics and CO₂ capture in RPBs and illustrates the challenges for the RPB industrial application. First, the hydrodynamics and mass transfer in the packing region and outer cavity zone have been separately reviewed. Then, various technologies to explore the RPBs have been reviewed, especially the Eulerian method and the challenges to use it. Further, the difficulties in applying the RPB have been analyzed and the comparison research between CPBs and RPBs have been reviewed, and the knowledge gaps for investigating RPBs are summarized.

2.1 Packing region

The RPB could be divided into three parts: the inner cavity zone, the packing zone and the outer cavity zone [42]. It is known that the effective interfacial area and the surface renewal of the phases in the packing region are significantly enhanced because of the high rotational speed, where most of the CO₂ is captured. There is no doubt that the packing region is the most crucial zone within the RPB and it is also the place that most investigators have focused on.

The packing region has been widely studied in terms of the flow dynamics and mass transfer. For the hydrodynamics, the flow patterns, liquid holdup, liquid droplet

diameter and liquid film thickness, as well as gas pressure drop, in the packing region have been investigated. While for the mass transfer, the effective interfacial area, the mass transfer rate, etc., have been analyzed. At the same time, various correlations for the liquid holdup, effective interfacial area, etc., have been developed according to these studies.

2.1.1 Flow dynamics

2.1.1.1 Flow patterns

The visual study of the liquid flow in the packing region has been conducted by using the experimental and CFD methods. After entering the packing region, the liquid phase has a strong interaction with the packing. The liquid flow in the reticulated and foam packing regions was visually achieved under various operating conditions and its patterns could be divided into three types: the pore flow, droplet flow and film flow, see Figure 2-1 [20, 46]. This can significantly enhance the mass transfer area between the gas and liquid phases. The same flow patterns in wire mesh and foam packings were clearly obtained by using the 2D VOF models [16, 20, 25-28, 47]. Both the simulation and experimental works showed that the flow patterns varied depending on the rotational speed.

Then, the forming process and breakage behaviors of the liquid droplets impacting the static and rotating single/multi-layer wire meshes were recorded by high-speed cameras [14, 18, 30, 32, 39, 40, 47-52]. The results indicated that the rotational speed, initial liquid jetting velocity, packing properties, etc., could influence the liquid dispersion. Further, this process for the droplets was simulated in the 3D models by using the VOF method and compared with these photographs [30, 32, 48, 53-57], which was shown in

Figure 2-2. From Figure 2-2(a), after passing through a layer of packing material, the liquid was dispersed into many droplets from a jet stream, which indicated that the effective interfacial area and the mixing could be remarkably enhanced at the first few layers of the wire mesh (inner edge of the packing), which is called the end-effect zone [18]. In addition, different flow patterns in the end-effect zone and bulk packing were observed [58] and the thickness of the end-effect zone was quantified [26, 59].

Although the number of mesh displayed in Table 2-1 is not very large for modelling the liquid phase passing through the single or a few layers of wire mesh, it is quite computational prohibitively expensive to model the liquid dispersion process in a real RPB with dozens of layers of wire mesh. As a result, an effective method should be developed to investigate the liquid dispersion.

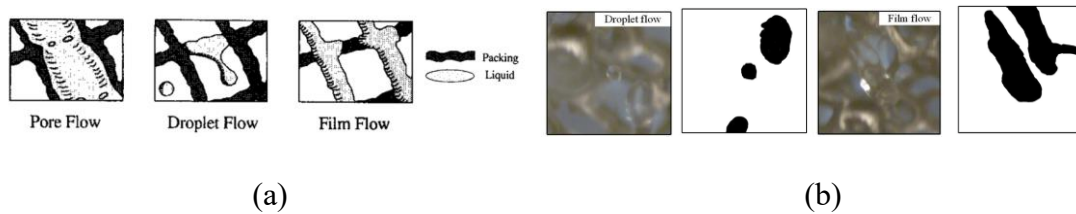


Figure 2-1 Schematic of the flow patterns within (a) the wire mesh packing [46]; (b) the foam packing [20].

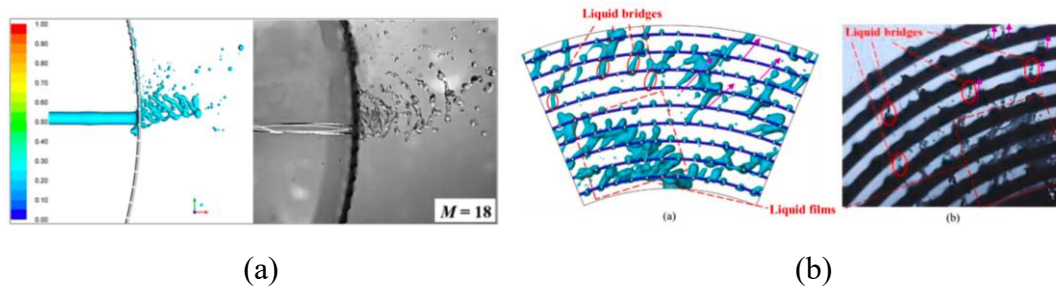


Figure 2-2 Comparison of the simulated and visualized liquid flow across the rotating (a) single-layer wire mesh [32]; (b) multi-layer wire mesh packing [53].

Table 2-1 The number of meshes number used in the models.

Author	Dimensional	Layer type	Number of layer	Mesh number (million)	Reference
Chen et al.	3D	single	1	5	[49]
Liao et al.	3D	single	1	17	[57]
Liu et al.	3D	single	1	15	[55]
Wen et al.	3D	single	1	70	[56]
Xu et al.	3D	single	1	18-27	[32]
Guo et al.	3D	multi	12	1.6	[17]
Li et al.	3D	multi	14	51	[48]
Zhang et al.	3D	multi	9	15	[53]

2.1.1.2 Liquid holdup

The liquid holdup (the amount of liquid held within the packing region) has a major impact on the gas-liquid mixing and the effective interfacial area formed between the gas and liquid, which directly influences the mass transfer performance of the RPB. In addition, it can reflect the porous resistance in the packing region, therefore, it is a critical parameter for the flow dynamics.

Initially, the electrical resistance technique was utilized to measure the liquid holdup in the packing region [60] and the most widely used correlation for predicting the liquid holdup was introduced, which is presented in Equation (2-1). From this correlation, it is known that the liquid holdup is determined by the rotational speed, liquid flow rate and liquid viscosity, and the liquid holdup is independent of the gas flow before the flooding point. Further, this correlation has been employed to validate many 2D RPB models when investigating the hydrodynamics in the packing region [6, 28, 29, 34, 38]. Based on this correlation, Xie et al. [31] proposed a new correlation with a similar form,

see Equation (2-2), using a small 3D representative elementary unit (REU) but the contact angle between the packing surface and liquid phase was considered in this research, and this indicates that the packing surface treatment and liquid surface tension could also affect the liquid holdup [40, 61]. In addition, the liquid holdup in a part of the 3D RPB model with the periodic boundaries was examined [48, 53, 62]. However, the VOF method has been applied in these works (REU or a part of the RPB) and this method is unsuitable for simulating a 3D full-scale RPB or entire packing model due to the large computing resources and long simulation time required.

$$\varepsilon_L = 0.039 \left(\frac{g}{g_0}\right)^{-0.5} \left(\frac{U}{U_0}\right)^{0.6} \left(\frac{v}{v_0}\right)^{0.22} \quad (2-1)$$

$$\varepsilon_L = 0.039 \left(\frac{g}{g_0}\right)^{-0.4764} \left(\frac{U}{U_0}\right)^{0.5716} \left(\frac{v}{v_0}\right)^{0.3197} \left(\frac{\gamma}{\gamma_0}\right)^{-0.7557} \quad (2-2)$$

With advancements in technology, the X-ray CT technique was employed to determine the liquid holdup in the packing region. Also, this technique allows for the measurement of the liquid holdup along the radial direction within the packing [63-65]. In addition, another form of the liquid holdup correlation was proposed for the wire mesh and foam packings by introducing the Galileo number (Ga), Kapitza number (Ka) and Reynolds number (Re), which is given in Equation (2-3). In addition to the above-mentioned correlations, many other liquid holdup correlations with a similar form have been proposed [66-68] and described in detail in the work of Zhang et al. [69]. Since these correlations were obtained by employing different packing, liquid type, etc., these correlations may be too general and cannot accurately predict the liquid holdup in a practical RPB.

$$\varepsilon_L = \begin{cases} 12.159Re^{0.923}Ga^{-0.610}Ka^{-0.019}, & \text{for wire mesh packing} \\ 12.159Re^{0.479}Ga^{-0.392}Ka^{-0.033}, & \text{for nickel foam packing} \end{cases} \quad (2-3)$$

Subsequently, the liquid holdup in the packing region was thoroughly investigated under different design parameters, especially the liquid distributor and gas inlet tube. For instance, the effect of the number and width of the liquid inlets on the liquid holdup have been investigated in the 2D RPB simulations [30, 38]. While, some design parameters, such as the liquid inlet length and the diameter of the gas inlet tube, could not be explored by using the 2D model. In addition, too many assumptions have been made in the 2D models, which may cause an inaccurate result. Thus, employing a 3D RPB model is a better choice to study the flow characteristics within the packing region. In addition, many investigators [17, 18, 32, 38-40, 53] have explored the liquid dispersion performance under the effect of gravity and the centrifugal force. Furthermore, the influence of the surface wettability and the liquid velocity, etc. on the liquid dispersion in the RPB have been analyzed in [18, 39-41]. The results show that the liquid dispersion plays an important role on the liquid holdup, however, the above studies are only at the stage of observing the phenomenon and the process of the dispersion in RPBs, and no one has evaluated and quantified its effect on the liquid holdup.

From the above analysis, we know that a complete 3D RPB model should be established and the VOF method is computational prohibitively expensive for the simulations of large RPBs. As a result, it is important and urgent to find a feasible and effective way to model a full-scale RPB for investigating the flow dynamics and the effect of the liquid dispersion on the liquid holdup should be quantitatively analyzed.

2.1.1.3 Liquid film thickness and droplet diameter

Due to the interaction between the liquid phase and rotating packing, the liquid spreads out and splits into small droplets, or forms thin films on the packing surface in the packing region, thus indicating that the effective interfacial area and micromixing can be enhanced [19]. The liquid droplet diameter and liquid film thickness directly affect the mass and heat transfer performance in the RPB, and they are important parameters in the development of the expressions for the mass and heat transfer coefficients.

Although the liquid film that covered the packing material could be detected by using a camera or an electrical resistance technique [31, 58, 70], it was difficult to directly and accurately determine its thickness from these visual works.

In order to obtain the thickness of the liquid film, Guo et al. [71] measured it flowing axially and transversely on a wire gauze. They found that the film thickness was thinner when using a higher rotational speed or a liquid with lower viscosity. In addition, an empirical correlation was developed to predict the liquid film thickness based on the experimental data, see Equation (2-4). Rauscher et al. [72] and Munjal et al. [73], respectively, investigated the liquid film thickness when the liquid flowed across a rotating disk and blade but the same correlation for the liquid film thickness was introduced, which is given as Equation (2-5). The main difference between the two equations is that the specific area of the packing (a_s) is considered in Equation (2-4) on which the liquid phase could cover. According to the above equations, the thickness of the liquid film decreases as the liquid viscosity reduces, resulting in a lower diffusion resistance, which is favorable for CO₂ absorption [74].

$$\delta = 4.20 \times 10^8 \frac{Q_L}{2\pi r h} \frac{v_L}{a_s \omega^2 r} \quad (2-4)$$

$$\delta = \left(3 \left(\frac{Q_L}{2\pi r} \right) \frac{v_L}{r \omega^2} \right)^{\frac{1}{3}} \quad (2-5)$$

For the liquid droplet diameter, it was investigated by an experimental method and CFD simulation [18, 71, 75-77] and the results illustrated above all show that the average droplet diameter is influenced by the physical property of the liquid (viscosity, density and surface tension), the operational conditions (inlet liquid velocity, rotational speed) as well as the packing parameter, such as the number of packing layers. Specifically, Gao et al. [77], Duan et al. [24] and Ouyang et al. [25] analyzed the impacts of the rotational speed, radial distance, inlet flow rate and the characteristic size of the packing on the droplet size by utilizing a high-speed camera and the droplet size distribution was expressed by adopting the Rosin–Rammler distribution. Shi et al. [27] developed a 2D RPB model and found that the average droplet size became smaller after adding a ring of static baffles in the middle of the packing.

Zhang et al. [18] studied the liquid droplets as the liquid passed through a single-layer static stainless steel wire mesh with/without hydrophobic surface-modified (HSM) treatment. The experimental results showed that the average droplet diameter generated by the HSM wire mesh was much smaller than that of the non-HSM wire mesh since the HSM wire mesh showed a higher hydrophobicity stability. In addition, Zhang et al. [18] took the contact angle between the liquid and wire mesh surface into account and empirically introduced a correlation Equation (2-6). According to Chen et al. [49], the ligament length at the impact position of the horizontal fiber was noticeably longer than that of the vertical fiber even when operating under identical conditions. Thus, the

pinch-off and recoil timescales were introduced to assess the influence of this disparity on the diameter of the liquid droplets, as represented by Equation (2-7). However, Equations (2-6) and (2-7) may not be an appropriate fit for the RPB because it was derived from the static single-layer wire mesh instead of the rotating multi-layer wire mesh packing.

$$\frac{d}{D} = 0.36 \left(\frac{u}{u_0}\right)^{0.051} \left(\frac{\sigma}{\sigma_0}\right)^{-0.291} \left(\frac{\mu}{\mu_0}\right)^{0.100} \left(\frac{\theta}{\theta_0}\right)^{-0.894} \quad (2-6)$$

$$d = \left(\frac{3V_0 \left(\alpha \left(100 \frac{\tau_p}{\tau_r} \right)^\beta + r \right)}{4\pi} \right)^{\frac{1}{3}} \quad (2-7)$$

Wen et al. [50] employed a multi-layer wire mesh to study the hydrodynamics in the mesh packings with novel fiber cross-sectional shapes and the effect of the cross-sectional shape (circularity index, δ) on the liquid diameter was explored, which is given as Equation (2-8).

$$d = 7.225 d_0 W e^{-0.269} R e^{0.013} \varphi^{0.795} \delta^{0.814} \quad (2-8)$$

Zhang [78] examined the liquid droplet diameter in the packing region under various operating conditions, and a set of experimental data was achieved. Based on this set of experimental data [78], the liquid droplet diameter in the packing region was regressed as two correlations, which are shown in Equations (2-9) and (2-10), respectively. Although the formulas of the liquid diameter in the packing zone are different, the value of these correlations is in a similar range, namely $-1 \times 10^{-5} < d_p < 1 \times 10^{-4}$.

$$d_{p,P} = 0.7284 \left(\frac{\sigma}{\omega^2 r \rho} \right)^{0.5} \quad (2-9)$$

$$d_{p,P} = 12.84 \left(\frac{\sigma}{\omega^2 r \rho} \right)^{0.630} u^{0.201} \quad (2 - 10)$$

2.1.1.4 Gas pressure drop

For the gas phase, the gas pressure drop could not only reflect the resistance in the packing region, but also influence the energy consumption. Thus, the gas pressure drop is another important parameter for the flow dynamics [79].

Initially, the dry pressure drop across the different packing materials, including the wire mesh [80], foam [81], Sumitomo (a metal sponge-like material made of 85% nickel and 15% chromium) [82] has been analyzed. Compared with the pressure drop caused by the velocity variation and centrifugal force, the friction resistance in the packing region is the dominant factor in the total pressure drop, which could account for 40-70% [83]. Also, it is concluded that the frictional pressure drop in the packed bed depends on the rotor dimensions, the packing properties, the gas inlet design as well as the operating conditions. Furthermore, the influence of the RPB type on the pressure drop has been examined, and the results show that the pressure drop for the cross-current flow RPB is smaller than that in the counter-current flow RPB.

Further, Liu et al. [84] analyzed the pressure drop in different spaces in a RPB with a rotational-stationary metal foam packing, which consists of the drop resulting from the rotating packing, the entry and exit losses at the outer and inner periphery of the rotor, respectively, as well as the pressure drop attributed to the momentum change as the gas transitions from the inner periphery of the rotor to the outlet pipe [80]. In addition, the pressure drop was examined when a single gas phase or gas-liquid phase passes through the RPB [85, 86]. They found that the dry pressure drop is lower than that in the wet

bed due to two reasons: on one hand, the wet packing surface can make the friction coefficient between the packing and the gas change. On the other hand, the liquid easily occupies the pores of the metal foam or wire mesh packing, which can be regarded as a porous material, and this blocks the passage of gas. Surprisingly, this conclusion contradicts that in a previous research [87], in which the dry and wet pressure drops across the rectangular packing and elliptic cylindrical packing have been investigated. The possible reasons are that the packing surface may be different, and the liquid phase is more prone to be retained in the metal foam packing due to its smaller pores. Nevertheless, both experimental results indicate that the liquid flow rate has little impact on the wet pressure drop within the specified experimental range [84, 87].

Overall, the gas pressure drop mainly results from two aspects: the first aspect is the resisting force, which includes the velocity variation, centrifugal force, and frictional resistance. Another aspect is the structure of the RPB, including the inlet, packing, outlet as well as the inner and outer cavity zones. According to the two aspects, various correlations to predict the pressure drop have been presented in [83, 88].

The CFD method was also employed to investigate the pressure drop of the PRBs. For example, the distribution of the pressure within the packing region was explored in the 2D RPB models [34, 37]. However, the obtained results may not be very accurate because the gas was evenly fed into the packing from the outer packing surface instead of from the dedicated gas inlets. In addition, the influence of the design parameters, such as the shape of the gas inlet tube, on the pressure drop could not be analyzed. Although the 3D models were established in order to optimize the RPB design, only the dry pressure drop was studied and the liquid phase was not included [21, 36, 89,

90]. Furthermore, the influence of the liquid phase on the pressure drop as well as the impact of the gas flow on the liquid holdup were not examined. Therefore, it is worth building a 3D RPB model to thoroughly investigate the gas and liquid flow characteristics.

2.1.2 Mass transfer

2.1.2.1 Effective interfacial area

The gas-liquid effective interfacial area (the contact area between the gas and liquid phases per unit volume of the packing, m^2/m^3) is a critical parameter as it can assist to accurately predict the porous resistant force and mass transfer performance. This term is different from the contact/mass transfer area (m^2), which directly represents the physical surface area that is available for mass transfer between phases. Various empirical equations for the effective interfacial area have been derived for CPBs and they have been utilized for RPBs simulation by replacing the acceleration force term in the equation with the centrifugal force in the RPBs, such as Equation (2-11) in Table 2-2 [91]. However, this often results in an underestimation in the value of the effective interfacial area [34, 92, 93].

Table 2-2 Correlations for the prediction of the (fractional) effective interface area in the packing region.

Packing type	Method	Correlation	Number	Reference
CPB with Random packing	Deduced	$f_e = 1 - \exp \left[-1.45 \left(\frac{\sigma_c}{\sigma} \right)^{0.75} Re_L^{0.1} We_L^{0.2} Fr_L^{-0.05} \right]$	(2-11)	[91]
RPB with foam metal	Chemisorption of CO ₂ with NaOH	$f_e = 11906 Re_L^{-1.8070} Fr_L^{-0.0601} We_L^{0.9896}$	(2-12)	[94]
RPB with wire mesh	Chemisorption of CO ₂ with NaOH	$f_e = 66510 Re_L^{-1.41} Fr_L^{-0.12} We_L^{1.21} \left(\frac{c^2}{(c+d)^2} \right)^{-0.74}$	(2-13)	[95]
RPB with wire mesh	Chemisorption of CO ₂ with NaOH	$f_e = 15.17 Re_G^{0.16} Re_L^{-0.38} Fr_L^{-0.13} We_L^{0.45} \varphi^{-0.29}$	(2-14)	[96]
RPB with wire mesh	CFD method	$A_{e,p} = 202.3485 \left(\frac{g_c}{g_1} \right)^{0.0435} \left(\frac{U}{U_1} \right)^{0.4275} \left(\frac{v}{v_1} \right)^{0.1200} \left(\frac{\beta}{\beta_1} \right)^{-0.5}$	(2-15)	[31]

The effective interfacial area in different RPBs was measured for CO₂ capture experiments [39, 43, 44, 97]. The results showed that the effective interfacial area increased with higher rotational speed and gas-liquid ratio. In specific, Rajan et al. [94] and Luo et al. [95] evaluated the effective interfacial area in the foam metal and wire mesh packings via the CO₂-NaOH absorption system, and accordingly, the fractions of the effective interfacial area were respectively given as Equations (2-12) and (2-13) in Table 2-2 [94, 95]. However, it should be noted that the above research considered the

effective interfacial area in the entire RPBs as representative of the packing region, potentially leading to an overestimation of the effective interfacial area. After realizing this issue, Luo et al. [96] focused on the effective interfacial area in the packing region by adding two ring baffles positioned at the upper and lower edge of the rotor, which could isolate the packing from the entire RPB. Also, the impact of the gas flow on the effective interfacial area was considered and a modified fractional effective interfacial area correlation for the packing region was introduced as Equation (2-14). Nevertheless, the accuracy of the correlation is affected by the absorption rate of CO₂, partial pressure of CO₂ in the gas phase, diffusivity of CO₂ in solution, etc. Therefore, it is not completely reliable.

In a recent publication, Xie et al. [31] conducted a study to estimate the effective interfacial area of liquid flow over a REU of a RPB. They employed the VOF modelling method and considered various gravitational acceleration forces and different liquid viscosities to resemble the absorbent with various concentrations passing through the rotating packing. The effective interfacial area was assessed directly by the contact area between the liquid and gas phases per unit volume of the wire mesh packing, which is not influenced by factors such as the absorption system, reaction temperature, CO₂ inlet concentration in the gas phase, etc. The model's validity was confirmed through experimental observations, and Equation (2-15) presents a correlation proposed for the effective interfacial area.

2.1.2.2 CO₂ capture based on mass transfer correlations

Many studies have been performed to investigate the mass transfer process and the process analysis based on various correlations derived from the RPB, such as

volumetric mass transfer coefficient. Process simulation methods using Aspen Plus combined with FORTRAN [23, 98, 99], gPROMS [92, 93, 100, 101] as well as other types of software [75, 102] have been proposed.

Aspen Plus has been widely used to study the CO₂ capture process for the CPBs, however, it lacks a suitable model available for RPBs. In order to address this issue, some built-in correlations for the mass transfer coefficients, liquid hold-up, effective interfacial area and pressure drop were replaced with new correlations that have been developed for RPBs [23, 98]. These correlations were coded as subroutines in visual FORTRAN and then linked dynamically with the Aspen Plus software. Furthermore, Joel et al. [99] studied the influence of the parameters on the CO₂ removal efficiency and the energy consumption within the RPB stripper, respectively. Moreover, the CO₂ capture process by Benfield solution was investigated by Yi et al. [75] employing correlations for gas and liquid mass transfer coefficients, liquid holdup, etc., based on the Matlab technique. Similarly, Oko et al. [103] analyzed the impact of environmental temperature on the CO₂ capture within the RPB, utilizing correlations for effective interfacial area, gas and liquid mass transfer coefficients. They also emphasized the significance of intercoolers in the RPB absorber, employing the gPROMS ModelBuilder.

Through utilizing the process simulation methods and various mass transfer coefficient correlations, the CO₂ capture process could be predicted and analyzed. Nonetheless, the prediction accuracy using this method heavily relies on the availability and accuracy of the existing correlations [104]. These correlations of the mass transfer coefficient have been developed from various systems, packing, and operating conditions. Thus, these

correlations are usually too general to be employed in a practical RPB. And most of them are not derived from the CO₂ and amine solution within the counter-current RPBs, which is used in this thesis. Also, the mass transfer in the outer cavity zone of the RPB has been overlooked in these works, which may result in an inaccurate predicted mass transfer behavior. Thus, an alternative approach should be introduced for describing the CO₂ capture process in the RPB.

2.1.2.3 Theory for the mass transfer

At present, there are three main theories for explaining the mass transfer between the phases, which are the two-film theory, the penetration theory, as well as the surface renewal theory. The two-film theory regards that two layers of film exist in both the gas and liquid phases separated by an interface. In addition, the mass transfer from one phase to another phase occurs by molecular diffusion through the film under steady state. Based on the two-film theory, Yi et al. [75] and Sun et al. [105] developed the mathematic models to explore the CO₂ capture in the RPB and the overall mass transfer coefficient was compared with the experimental data under different operating conditions. Both predicted results had a good agreement with the experimental data with a deviation within 10%.

The penetration theory and surface renewal theory can be seen as an advancements over the two-film theory as mass transfer takes place under unsteady-state conditions, and the two parameters - the contact time and surface renewal frequency are introduced, respectively. Zhang et al. [106] and Qian et al. [102] have investigated the absorption of the CO₂ into different solutions by using models based on the penetration theory. In addition, the predicted results agree well with the experimental data, with deviations

within 15% and 4%, respectively. Further, Qian et al. [107, 108] have investigated the selective absorption of H₂S using a RPB based on the same theory. They reported that the lifetime of a liquid film in the RPB is significantly longer (by 7 orders of magnitude) than the penetration time of H₂S. Therefore, the reaction and mass transfer of H₂S can still occur efficiently, even during a quite brief gas-liquid contact time within the RPB. Therefore, an impressive H₂S capture efficiency of approximately 99.76% also can be attained [108]. Furthermore, a model based on the renewal frequency has been used to explore the gas-liquid mass transfer characteristics in a RPB. In addition, Luo et al. [15] conducted experiments and found that the experimentally obtained values of $k_L a_e$ align with the model predictions within a range of $\pm 15\%$. Similarly, Luo et al. [109] employed the surface renewal theory to analyze the CO₂ absorption process in the RPB under the steady and dynamics states. The model was validated by the experimental data and the dynamics study was conducted by changing the gas/liquid flow rates. The results suggested that the RPB has a fast response for the process changes.

While it has been demonstrated that the penetration theory and surface renewal theory offer improved accuracy in calculating mass transfer [110], measuring the contact time and surface renewal frequency in RPBs, especially under unsteady-state conditions, can be challenging. As a result, the two-film theory remains the most widely used and practical approach for describing CO₂ mass transfer between phases [111-115]. For instance, in the CFD study conducted by Lu et al. [6], the two-film model combined with the Henry's law successfully represented the CO₂ chemical-enhanced absorption in RPBs. This approach proved its reliability and feasibility to express the mass transfer in the RPB, without relying on correlations for mass transfer coefficients.

2.2 Outer cavity zone

The cavity zone refers to the annular space situated between the outer edge of the rotor and the inner boundary of the casing within the RPB, where numerous tiny liquid droplets move to. Mass transfer can also take place in the outer cavity zone, in addition to the packing region. The outer cavity zone typically exhibits a significant larger space compared to the packing region. This suggests that significant mass transfer also could occur in the outer cavity zone. However, it is often overlooked, with most research efforts concentrated on the packing region. Consequently, only a few studies have explored the outer cavity zone, focusing on the flow dynamics and the mass transfer process occurring within that region.

2.2.1 Flow dynamics

2.2.1.1 Visual studies

The study of the liquid flow characteristics in the outer cavity zone is essential for a better understanding of the mass transfer that takes place in this zone. Sang et al. [116] explored the liquid flow pattern and the flow pattern transition in the outer cavity zone. Two distinct flow patterns - ligament flow and droplet flow - were observed, and the ligament flow disappeared and numerous droplets formed as the rotational speed increased. The above phenomenon could also be observed in the 2D RPB models with the VOF method [26, 28, 47]. In addition, Gao et al. [77] visually obtained the process of the droplets coalescence in the outer cavity zone by the experimental and CFD methods. Further, Sang et al. [42] analyzed the process of the liquid flow in the outer cavity zone. The droplets from the outer edge of the packing, moving at a high velocity, traveled a short distance and impacted upon the casing wall, thus generating a liquid

film and a significant number of splashing droplets. In this process, droplets originating from the outer edge of the packing were referred to as mother droplets, while the splashing droplets were called daughter droplets. Thus, the mass transfer in the cavity zone encompasses three components: the mother droplets before impacting the casing, the liquid film adhered to the inner surface of the casing, and the daughter droplets after impact on the casing.

2.2.1.2 Droplet diameter

As mentioned in Section 2.1.1, the droplet diameter is crucial for the mass transfer and heat transfer performance in the RPB. Sang et al. [116] and Gao et al. [77] have investigated the impact of various factors, such as the rotational speed, outer packing radius, liquid viscosity and liquid initial velocity, on the average droplet diameter and its distribution in the outer cavity zone by using the R-R distribution method. They both found that the rotational speed is the dominant parameter for the droplet diameter, while the liquid initial velocity exhibits a limited effect on the average droplet diameter. Based on the experimental data, two correlations for the average droplet diameter are proposed as follows [77, 116]:

$$d_{p,o} = 0.042We^{-0.272}Re^{0.068}\left(\frac{u_0}{\omega r_o}\right)^{0.098}r_o \quad (2-16-(a))$$

$$We = \frac{\rho\omega^2 r_o^3}{\sigma}; Re = \frac{\rho\omega r_o^2}{\mu}; q = \frac{u_0}{\omega r_o}; u_0 = \frac{Q_L}{2\pi r_i h} \quad (2-16-(b))$$

$$d_{p,o} = 47.5R^{0.194}N^{-0.765}Q_L^{0.0391} \quad (2-17)$$

Compared with Equation (2-17), the properties of the liquid phase, including the viscosity and surface tension, are considered in Equation (2-16). In addition, Equation

(2-17) is derived from the packing that consists of vertical blades rather than the wire mesh, thus, making Equation (2-16) potentially more suitable for the RPB packed with the wire mesh.

2.2.2 Mass transfer

At present, the majority of the investigations have considered the RPB as a whole unit, which assumes that the chemical reaction only occurs in the packing and not in the cavity zone. However, it is worth noting that the volume of the cavity zone could even account for about 77.8% of the whole RPB. This indicates that the mass transfer and chemical reactions in the cavity zone could not be ignored. Unfortunately, only a few works have explored mass transfer in the outer cavity zone, and almost all of them relied on experimental techniques.

The mass transfer in the outer cavity zone has been investigated through the use of innovative experimental methods. One such example is the work by Guo et al. [43], where a unique approach involved introducing N₂ flow exclusively into the packing region to ensure that reactions occurred solely within the cavity zone while protecting the packing zone, which is shown in Figure 2-3(a). The findings revealed that the mass transfer area of the cavity zone accounted for approximately 30% of the overall RPB mass transfer area, with the remaining 70% attributed to the packing area. Another study conducted by Luo et al. [96] employed a novel experimental rig (see Figure 2-3(b)), dividing the internal space of the RPB into four distinct zones, thus allowing for a separate calculation of the contact area in each zone. The obtained results indicated that the mass transfer area of the cavity zone ranged from 8.5% to 9.2% for different types of packing materials. In addition, an L-shaped tube has been set up between the rotor

and the casing for measuring the CO₂ concentration in the gas stream by Yang et al. [44] as presented in Figure 2-2(c). Their work determined that the contribution of the cavity zone to mass transfer ranged from approximately 13% to 25% of the total mass transfer in the entire RPB. Therefore, the mass transfer in the outer cavity zone cannot be ignored and warrants further investigation.

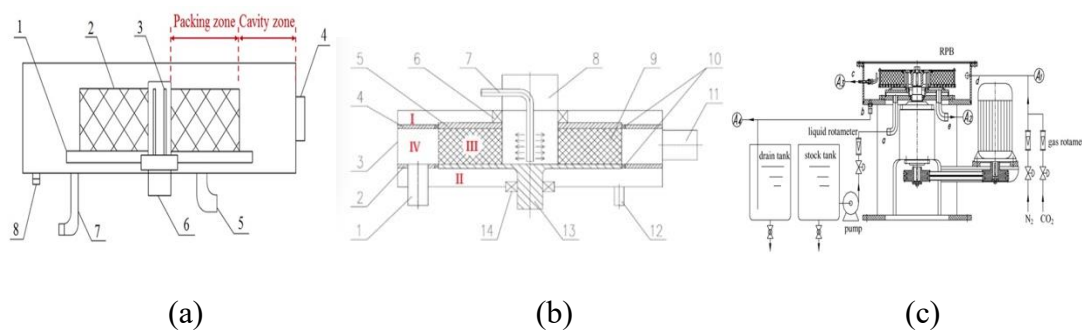


Figure 2-3 Schematic diagram of the RPB experimental rig (a) [43]; (b) [96]; and (c) [44].

In addition to the experimental method, a mathematical model was built to predict the average droplet diameter and mass transfer area of the cavity zone by Sang et al. [42, 116]. The influence of the rotational speed, liquid initial velocity and outer packing radius was also analyzed. The results showed a high level of agreement with the experimental data and revealed that the liquid film and daughter droplets played a more significant role in the overall mass transfer within the cavity zone compared to the mother droplets.

By incorporating both experimental and mathematical approaches, the researches has emphasized the significance of the cavity zone in the RPB due to the unignorably mass transfer area and mass transfer contribution. However, it is important to note that the cavity zone remains relatively unexplored, particularly in terms of utilizing simulation

methods. Consequently, further research efforts should focus on investigating the liquid flow dynamics and chemical reactions occurring within the cavity zone by utilizing the CFD approach, which could help to accurately and effectively predict the CO₂ capture processes and optimize the RPB performance.

2.3 CFD simulations

Among the studies on the RPB, CFD has been widely employed to investigate the gas and liquid flow inside the 2D and 3D RPB models. For the single-phase, the gas flow behaviours, including the pressure drop and its distribution, have been studied in various RPB models. While for the gas-liquid phase, two methods, i.e. the VOF and Eulerian methods have been utilized to investigate the wet pressure drop, liquid holdup, liquid dispersion, etc., within the RPB. In addition, the mass transfer performance has been explored by using the CFD method coupled with user defined functions (UDF).

2.3.1 Single-phase flow behaviours

The gas flow characteristics have been studied mainly by employing a 3D RPB model. For instance, the distribution of the gas pressure and pressure drop were simulated as it passed through a 3D packing region with a complex wire mesh matrix, similar to the experimentally investigated structured packing [21, 33]. Liu et al. [21] concluded that a considerable portion of the gas pressure drop occurred in the inner cavity zone. Also, an interesting phenomenon of intense turbulence, defined as the gas-side end effect, was observed in the outer packing zone within the PRB. In addition, the packing region could be regarded as a porous media for reducing the computing resources. In this way, Llerena-Chavez and Larachi [89], Yang et al. [36] and Wu et al. [90] investigated the mal-distribution of the gas pressure in the 3D RPB models. In order to reduce the mal-

distribution and improve the gas-side mass transfer coefficient, the optimum design of the RPB were also conducted by incorporating internals or baffles. In addition, their shape and distribution were examined by analyzing the gas distribution. However, the drag force between the packing and gas flow was typically determined by the general Ergun equation instead of the drag force model derived from the wire mesh or foam packing, where the effect of the packing structure on the gas flow behaviours was not completely taken into account [38]. Furthermore, the impact of the liquid phase on the gas flow characteristics was not clear, and it was reported that the difference between the dry and wet pressure drop in the RPB was quite large [80, 86, 87, 117], thus indicating that the study of only single-phase flow is not sufficiently accurate compared to the practical situations.

2.3.2 Multi-phase flow characteristics

2.3.2.1 VOF method and its limitations

For the two-phase flow modelling, the VOF model has been extensively utilized in the 2D and 3D RPB models since it is well-suited for tracking the volume fraction of each phase and can accurately capture the gas-liquid interface as well as the behavior of droplets impacting on the wire mesh. Also, it allows for a clear representation of the dynamic evolution of the interface between the gas and liquid phases in the RPB system.

For 2D simulations, Duan et al. [24], Shi et al. [27], Gao et al. [77] and Wu et al. [30] studied the flow patterns and liquid droplet size in the packing and outer cavity zones by combining the VOF model, sliding model, and the Reynolds stress model or realizable k - ϵ model. In specific, the sliding model was utilized to simulate the rotation

of the packing, which is the most accurate approach but computationally demanding [118]. To simplify the model, Xie et al. [28] and Zhang et al. [38] assumed that making the liquid nozzle rotate in the opposite direction relative to the rotational coordinate system and fixing the packing could achieve the same effect. In fact, there is no additional centrifugal force acting on the liquid phase due to the static of the packing, which is different from a real RPB environment. As a result, the tangential velocity of the liquid phase would decrease when passing through the static packing region, in contrast to the actual tangential velocity in a rotating packing [24, 119]. All these obtained simulation results showed that the liquid distribution in the packing region became more uniform with higher rotational speed, thus causing an improved micromixing behaviour, as reported in the work of Yang et al. [29] and Guo et al. [19]. Yang et al. [29] investigated the oxygen absorption in the water using a UDF and Chen's liquid side mass transfer coefficient correlation. They found that the micromixing behaviour was extremely strong in the region near the inner edge of the packing, referred to as the 'end effect' zone [60], due to the liquid-packing collisions. Further, a novel approach was proposed by Ouyang et al [26] to quantify the thickness of the 'end effect' zone in terms of the residence time. Also, different turbulence models were utilized and compared in the work of Ouyang et al. [16, 25, 26]. Furthermore, Liu et al. [20] and Yang et al. [29] explored the liquid holdup and the liquid distribution within the packing under various operating conditions, and the results were compared via Yang's [29] and Burns' [60] correlations, respectively.

However, too many assumptions have been made in the above 2D simulations, which may cause an inaccurate result. For instance, the latitude and longitude wires with cross-section shape have been simplified as four square straight wires parallel to the rotational

axis, neglecting the direct influence of the wire mesh structure on flow characteristics [27]. In addition, the RPB design optimization could not be fully completed based on the 2D model, especially for the height of the packing or shape of the liquid nozzle. Therefore, 3D RPB models are required to achieve the RPB optimization design and more accurate flow characteristics.

In order to better understand and optimize the RPBs, 3D RPB models have been used to study the multi-phase flow characteristics. Xie et al. [31] analysed the gas-liquid flow by using 3D REUs of the RPB where different gravitational forces were employed in the REU to model the flow at different locations across a typical RPB, so that the overall characteristics of the liquid flow in the RPB was successfully assembled. By utilizing this mesoscale model, the sensitivities of the liquid holdup and effective interfacial area to the rotational speed, liquid flow rate, contact angle and viscosity were investigated, and the corresponding prediction correlations were proposed. And a correlation of the effective interfacial area was proposed which has been further utilized in the work of Lu et al. [6], Zhang et al. [37]. In addition, using the VOF method, Guo et al. [17] investigated the liquid holdup, liquid droplet size and residence time in a packing models in 3D. However, the multilayer wire mesh packing was simplified as numerous straight wires parallel to the rotor axis, without considering the effect of the horizontal wire meshes. Thus, the difference of the liquid holdup obtained from the experiment, simulation and Bruns' correlation was large.

In order to obtain the liquid behaviours in the inner packing zone, Chen et al. [49], Wen et al. [56], Zhang et al. [38] and Xu et al. [32] explored the interaction and dispersion after the liquid jet impacts on the 2D and 3D rotating single-layer wire mesh,

respectively. The obtained liquid flow pattern was compared with that from the experiment, and the impacts of the mesh number and operating condition were analyzed. After that, the liquid flow passing through multi-layer wire mesh was simulated by adopting the VOF method, sliding model, dynamic mesh adaptation procedure, which could improve the dynamic process of the droplet breakup in turbulent flows [17]. However, the liquid flow behaviours among the multi-layer wire mesh were not clearly captured due to the small mesh number (around 1.6 M). Recently, Zhang et al. [53] utilized a sector RPB model with periodic boundaries to simulate the dynamics evolution process of droplets across the multi-layer wire mesh, increasing the number of meshes reached to 15 million. With the large number of meshes, the effect of the contact angle and rotational speed on the liquid flow pattern was investigated and a new flow pattern of the “branch flow” was reported in the packing region. Also, a similar model was established by Vlahostergios et al. [62] to pave the way for exploring the production of nanoparticles of CaCO_3 and $4\text{MgCO}_3\text{Mg}(\text{OH})_2\cdot 4\text{H}_2\text{O}$ but with a porous medium model.

According to the aforementioned work, none of them has modelled the full scale RPB by employing the VOF method. The advantage of employing the VOF method is that it can reasonably, clearly and accurately capture the interface between the gas and liquid, including the evolution of the liquid droplets in the RPB. Due to the multiscale nature of the liquid flow in an RPB, the computational mesh should be fine enough to resolve the finest droplet and liquid films, typically in millimetres and even microns metre scales, in addition to the packings, within a metre scale RPB. When modelling in full scale 3D RPB, this will require a prohibitively large number of computational cells and computational time. This is the reason why most of the CFD simulations using CFD

methods are for small 3D RPB models and mostly in 2D [21, 119]. In addition, the VOF model requires a transient simulation, thus meaning that a much longer time is required. For instance, about 1.4 million cells and a simulation time of about 60 h were required for each case in the 2D work of Guo et al. [19], despite only simulating an RPB with inner and outer diameters of 80 mm and 140 mm, respectively. Therefore, considering the future scaling up and optimization of RPBs, a promising modelling approach - the Eulerian method - should be considered.

2.3.2.2 Eulerian method and its challenges

The Eulerian method has shown a great potential for reducing the computational cost in modelling the RPBs [6, 34]. This method has been commonly used in the simulation on the conventional packed bed, however, it is scarcely utilized in the RPB as many challenges should be dealt with first.

Gao et al. [77] employed the Eulerian method to investigate the droplet characteristics and behaviours in a rotor model with 180 vertical blades arranged evenly along its circumference. However, the appropriate mathematical models need to be added to the governing momentum equations to describe such as the porous resistance and liquid dispersion forces. In the above work, only the gas-liquid interfacial force was introduced and the interfacial force were calculated based on the Schiller and Naumann model [120]. It was shown that the Eulerian multiphase model was able to provide good estimates of the droplet velocity. This work is very similar to the study conducted by Li et al. [48]. By using the same Eulerian method and interfacial force model, Li et al. [48] established a more complex and realistic sector RPB model with periodic boundaries, where the packing was composed of multiple layers of flat and corrugated wire mesh,

totaling fourteen layers in the radial direction. The liquid holdup and wetting efficiency were achieved and the flow patterns passing through the wire mesh could be clearly observed. The RPB structure was optimized by designing the liquid distributor and installing the blades, which resulted in an enhanced axial utilization efficiency. However, in order to clearly achieve the flow characteristics within the RPB, the aforementioned studies employed a detailed wire mesh packing configuration. Consequently, the required number of mesh in the above works was too large, with the sector RPB model established by Li et al. [48] reaching an amazing 51 million.

The Eulerian method with the porous medium model may overcome this problem because it does not focus on resolving the matrix structure of the packing in detail. Instead, the packing is considered as a porous medium and its effect on the flow is considered computationally using a suite of mathematical formulations. This can substantially reduce the complexity and number of the cells in the computational mesh that is employed, thus leading to a significant reduction in the computational resources and simulation times required. For instance, Martínez et al. [35] have used the Eulerian method to examine the distribution of the water and SO₂ velocity in a porous medium model without drawing the wire mesh profiles. However, the drag forces between phases and packing as well as the interfacial force between the phases could not be simply estimated from the pressure drop data available in the work of Sindalya et al. [80]. Thus, in order to employ this method, the primary task is to find an appropriate porous media model that can accurately express the drag force between the gas and liquid, the gas and solids and the liquid and solids for the wire mesh packing used in RPBs, since it substantially influences the liquid holdup and the gas pressure drop.

Although various porous medium resistance force models, such as those for spherical packing [121, 122], structured slit packing [123], and tube bundle packing [124], have been proposed, Lu et al. [34] proved that these models were not suitable for the wire mesh packing used in RPBs. In 2009, Kołodziej and Łojewska [125] put forward a one-phase model that takes into account both the viscous and inertia contributions to the overall resistance of the wire meshed porous media, based on single flow experiments through wire gauzes, which is similar to that of the flow through a wire mesh packing in RPBs. Based on the Kołodziej one-phase model, Lu et al. [34] developed it into a multi-phase model to examine the gas-liquid counter-current flow in a 2D RPB. The results indicated that this model was more appropriate in predicting the liquid holdup compared with other porous media models and the simulation time could be significantly reduced.

Subsequently, Kołodziej et al. [126] introduced a refined porous resistance model by redefining the effective length and effective velocity of the liquid flow in the packing region. Based on the Kołodziej one-phase porous medium models and the experimental data, Bussière et al. [127] plotted the total Fanning friction factor for all the woven screens and regressed the fitting curves to $f = 7.357 \times Re^{-0.596} + 0.04351$. However, this regressed fanning friction factor is not suitable for all the woven screens, thus, it may not accurately predict the pressure drop and liquid holdup in some cases [127]. Zhang et al. [37] compared the Kołodziej, Kołodziej refined and Bussiere regressed models by analyzing the liquid holdup and gas pressure drop. It showed that the Kołodziej refined model was the most accurate for simulating the gas-liquid flow in RPBs, which may be utilized in this thesis.

In the above-mentioned studies, the liquid dispersion in the packing region has not been taken into account, which plays an important role in determining the liquid flow behaviour and is the predominant reason for the enhancement of the mass transfer in RPBs [18]. Liquid dispersion in the RPBs has been explored previously both experimentally and computationally using the VOF method. Ma et al. [41], Su et al. [40] and Zhang et al. [18] experimentally reported the details of the process of the droplet impacting on the stationary wire mesh as well as the dispersion phenomenon under the effect of gravity. Further, the liquid dispersion and liquid flow patterns cross the rotating multi-layer wire mesh have been observed and the influence of the feature size of packing, rotational speed, liquid flow rate on the droplet diameter has been analyzed [24, 30].

Similar to the experimental work, the dispersion phenomenon of a liquid jet impacting on the rotating single-layer and multi-layer wire meshes has been simulated by utilizing the VOF method [14, 17, 32, 38, 53]. However, the above studies were only at the stage of observing the phenomenon and the process of the dispersion in RPBs, and no one has evaluated and quantified the dispersion in a RPB, especially when using the Eulerian method.

In order to employ the Eulerian porous medium model to investigate the liquid dispersion, a dispersion model needs to be devised to calculate the dispersion force term as a consequence of the volume averaging in the momentum equations [128]. Currently, there has been no dispersion model developed specifically for RPBs. However, various such models have been proposed for the modelling of the liquid dispersion in the CPBs. These models may be divided into the capillary pressure models and mechanical

dispersion models according to the dispersion mechanism that they model in the CPBs [129]. The capillary pressure force is produced by the difference in the pressures across the fluid interface. In addition, the mechanical force is caused by the complex advection of the momentum by the fluid at the pore scale [130] or, in other words, the variation in the velocity with respect to the main flow at the macroscopic scale [131].

It should be noted that the packings employed in the CPBs and RPBs are very different. In addition to the bed design, the packing elements are different and the packing in an RPB is much more densely packed. The driving force and the flow patterns are also very different. Nevertheless, one may take the view that both CPB and RPB are similar in that they both can be regarded as being a porous media and the liquid disperses from a higher volume fraction to a lower volume fraction under the framework of the porous medium approach. The macro dispersion mechanisms are similar in RPBs and CPBs. Hence, it is expected that these dispersion models for CPBs could be employed in RPBs with careful evaluations. One of the main objectives of this thesis is to assess the suitability and limitations of the existing dispersion models when they are applied to model the RPBs. More information about these models are presented in Chapter 3.

2.3.2.3 Mass transfer performance

As is well known, the mass transfer can be greatly improved in the RPB due to the centrifugal force resulting from the rotation of the packed bed. Currently, only a few studies have explored the mass transfer process within the RPB, especially for the CO₂ capture, through employing both the VOF and the porous medium approaches. Guo et al. [19] employed the VOF, together with the laminar finite-rate reaction and Reynolds stress turbulence models to explore the micromixing efficiency of the 2D RPB based

on the iodide–iodate reaction system. Yang et al. [29] investigated the oxygen absorption in the water in the 2D packing region by employing the VOF model and Chen’s liquid side mass transfer coefficient correlation via a UDF. They both found that the micromixing behaviour was extremely strong in the ‘end effect’ zone due to the liquid dispersion produced by the collision between the liquid and the packing. Since the semi-mass transfer correlation was used, it may not be able to accurately predict the mass transfer process in a practical RPB as the correlation was too general. As mentioned before, using VOF method requires a prohibitively large number of computational cells to model a 3D full-scale RPB where multiple-length scales which exist in the RPB have to be resolved to achieve an acceptable level of accuracy in CFD simulations. Therefore, the Eulerian porous medium approach is preferred.

Lu et al. [6] introduced a 2D axisymmetric Eulerian porous medium model incorporating the two-film chemical-enhanced mass transfer model and heat transfer model to investigate the CO₂ capture in a RPB, as is illustrated in Figure 2-3(a). The model uses a much coarser computer mesh compared with that typically employed in a VOF model, with only a 0.09 M mesh number, thus saving the computing resources and simulation time. The results showed that the overall gas phase mass transfer coefficient increased with increasing the rotation speeds and the liquid to gas mass flow rate (L/G ratio). Although using the developed models could effectively predict the CO₂ capture performance and liquid temperature distribution (see Figures 2-3(b) and 2-3(c)), they were not enough accurate in this 2D packing model. For example, the predicted overall mass transfer coefficient was much lower than the experimental data, which could be even up to 50% when using 90% MEA solution [6]. The possible reasons are as follows: firstly, the mass transfer in the outer cavity was not considered,

and it have been reported that the contribution of the cavity zone to the overall mass transfer accounts for about 13–25% in the whole RPB [44]; secondly, the influence of the liquid droplet diameter on the heat transfer was ignored and the liquid droplet diameter was set using the default value in the software, which was too small. The liquid diameter is reversely proportional to the heat transfer rate between the phases. The smaller diameter leads to a higher heat transfer rate, thus resulting in a lower liquid temperature and reaction rate; thirdly, the liquid flow is uniformly distributed at the inner packing surface in the above simulation, which directly influences the liquid holdup and mass transfer performance. If the liquid is jetted from the liquid nozzles, the liquid phase in the packing region will become a nonuniform flow, and accordingly, the effective interfacial area for the non-uniform gas and liquid flows should be reconsidered; finally, the liquid dispersion in the packing region has not been taken into account due to the interaction with the wire mesh, which plays an important role in determining the liquid flow behaviour and is the predominant reason for the enhancement of the mass transfer in RPBs [18].

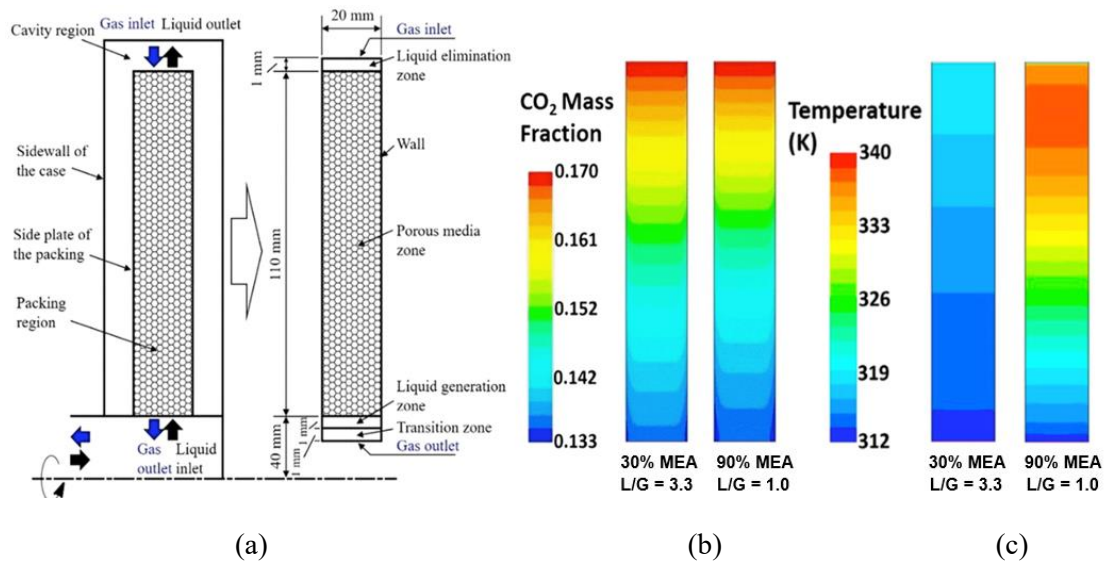


Figure 2-4 (a) Schematic diagram of the physical 2D RPB model; contours of the (b) CO₂ mass fraction in the gas phase; and (c) liquid temperature for 30% MEA and 90% MEA [6].

Overall, a 3D full-scale RPB model using the Eulerian porous medium method could be effectively performed. In this model, the liquid dispersion in the packing region, the CO₂ capture in the outer cavity zone, the effective interfacial area for the non-uniform gas-liquid flow, and even the liquid droplet diameter in the packing and outer cavity zone, should be carefully and thoroughly considered in order to accurately predict the CO₂ capture processes within the entire RPB model.

2.4 Comparison between RPB and CPB

Although the RPB has many advantages, such as a high mass transfer rate and small equipment size, it has not been commercially utilized for PCC [132]. The first possible reason is that the design procedures for the large-scale RPB and the principles for the scaling up of the RPB have not been proposed for PCC. Although a general design procedure has been mentioned in the studies conducted by Agarwal et al. [13] and

Sudhoff et al. [133], it may not be suitable for the PCC process. In addition, the overall mass transfer rate, which is a key parameter to determine the outer packing radius, is difficult to be determined since this parameter is currently only available from the laboratory or pilot-scale RPBs. Consequently, the size of the RPB may not be accurately achieved. Therefore, systematic design procedures for the large-scale RPB should be carefully considered in the future.

Secondly, even though the large-scale RPB has been constructed for industrial CO₂ capture, how to operate a CO₂ capture plant with the RPB absorber is another issue. In fact, the influence of the operating parameters on the hydrodynamics and CO₂ capture performance have been investigated by using the experimental and simulation approaches [6, 20, 25, 31, 53, 75, 89, 102, 134, 135]. However, these investigations have been conducted based on the lab-scale or pilot-scale RPBs with the outer packing diameter being smaller than 0.3 m. It is unknown whether the conclusions drawn by these small RPBs are still suitable for the large-scale RPB since the CO₂ capture processes in multi-scale RPBs may be different. For example, the change in the trends of the liquid temperature in different RPBs are opposite when the liquid flow rate increases [92, 109]. Therefore, the sensitivity of the operating parameters on the CO₂ capture processes inside a large-scale RPB should be more thoroughly investigated in order to offer more important information on the operating and process optimization.

In addition, the advantage of the RPB over the CPB has not been thoroughly and clearly established. Existing literature indicates that the RPB has a superior mass transfer performance at both the lab-scale and pilot-scale facilities [83, 136-139]. Nevertheless, the mass transfer rate will decrease with the increase in the radial length of the packing

due to a weaker liquid-packing interaction, especially in a large-scale RPB [140], which is different from the CPB. Thus, it is difficult to ascertain whether the mass transfer rate in the large-scale RPB is still better than that in the large-scale CPB. In addition to the capture level, while RPBs may offer reduced equipment size and capital costs, the extra energy required by the rotor and its cost-effectiveness compared to CPBs remain uncertain, although it has shown that the energy required by the motor is extremely smaller than regeneration energy in the work of Chamchan et al. [141]. More importantly, the regeneration energy would be significantly saved if the liquid flow rate required by the RPB could be reduced. Overall, the RPB and CPB should be more thoroughly compared when employing them for CO₂ capture.

In fact, the comparison between the RPB and CPB has been conducted in both the lab-scale and pilot-scale in many experimental works [106, 134, 141, 142]. Chamchan et al. [141] compared the RPB and CPB absorbers in the pilot-scale with a fixed low MEA concentration of 20% and a high rotational speed of 1600 rpm. The simulation results indicated that the height of the transfer unit (HTU) of the CPB was around 10 times that of the RPB, and the energy consumption using the RPB is slightly higher than that when using the CPBs. However, the RPB sizes employed in these experiments are still small, and these are listed in Table 2-3, and the maximum outer packing radius is no more than 0.36m. Thus, the obtained conclusion may be not suitable for the large-scale RPB application. Further, Kang et al. [93] and Thiels et al. [142] successfully modelled the above CPBs and RPBs based on the gPROMS and Aspen Plus platforms and some semi-empirical correlations were employed to model the liquid holdup, mass transfer rate, etc. However, these correlations were too general since they were derived from various mass transfer systems and packings, thus they may fail to accurately predict the

CO₂ capture processes and compare the RPB and CPB.

Table 2-3 Summary of the dimensions and operating conditions of the rotating packed bed for comparison.

References	[141]	[134]	[106]	[142]
CO ₂ mole fraction (%)	32%	15%-50%	10%	10%
Absorbent	20% MEA	3% NH ₂	--% ionic liquid	30% MEA
Rotational speed (rpm)	1600	400-1300	1130-2150	1600
CPB diameter and height (m)	0.1, 2	0.0254, 0.3-1.2	0.025, 0.2	0.025,0.6
RPB inner, outer packing diameters and height (m)	0.12, 0.36, 0.06	0.025, 0.125, 0.023	0.02, 0.04, 0.02	0.025, 0.125, 0.023
CPB/RPB volume ratio	3	0.5-2.2	5.2	1

In conclusion, the studies on the design procedures for large-scale RPB, process optimization for a large-scale RPB, and the comparison between the RPB and CPB are still very limited, and these topics need much further research before the industrial application for the PCC.

2.5 Knowledge gaps

In general, the RPB could overcome the disadvantages, such as high operation cost and large plant footprint, brought about by the CPB. The RPB has by far gained more attention and many investigators have put substantial effort in the studying of the RPB. The works on the fluid flow characteristics and mass transfer process in the packing and outer cavity zones, the research methods, as well as the comparison between the RPB and CPB have been reviewed and discussed in the chapter, and some issues have been found and demand much more investigation, which is illustrated as follows:

(i) The 3D Eulerian method with porous media model should be employed for studying the flow dynamics and mass transfer.

The Eulerian method with porous media model has been proven to be a promising and effective way to study the gas-liquid flow behaviours for the RPB in the previous works. However, these works cannot accurately predict the hydrodynamics because of the employed 2D model, using improper porous resistance force, and without considering the effect of the liquid dispersion, and these issues can directly and significantly influence the flow characteristics. For effectively and accurately predicting the liquid flow characteristics, these difficulties should be overcome. As a result, a new model - 3D Eulerian porous medium model, should be developed.

(ii) The liquid flow characteristics, especially the liquid dispersion in the packing region, should be investigated.

In addition to the experimental method, the liquid dispersion when liquid flow impacts on the single/multi layers wire mesh packing has been studied via using the VOF approach. However, it is time-consuming by employing this method due to the large number of the mesh and the complex geometry. In addition, the works on the liquid dispersion are only at the stage of observing the phenomenon and the process of the dispersion in RPBs, and they are not sufficient to evaluate and quantify the dispersion in RPBs. Nevertheless, the dispersion force model has not been proposed and no one has employed the dispersion force in the Eulerian RPB model. Thus, it is essential to develop a dispersion force model, which is suitable for RPB, to accurately explore the liquid flow in the RPB.

(iii) The 3D RPB model with momentum, mass, and heat transfer models should be

developed for the PCC.

At present, the mass transfer and the process analysis of the RPB have been analyzed, however, these works heavily rely on the correlations of the liquid holdup, effective interfacial area, and mass transfer rate, whose applicability and accuracy are uncertain for a practical RPB. In addition, the hydrodynamics, thermodynamics and mass transfer could influence each other in the RPB. Thus, the heat transfer model and reaction-enhancement mass transfer model should be employed into the Eulerian porous medium model developed above for accurately and comprehensively examining the CO₂ absorption into amine solution.

(iv) The CO₂ capture in the packing and outer cavity zone should be separately analyzed.

Most of the studies concentrate on the hydrodynamics and mass transfer in the packing region, and the outer cavity zone are always ignored. However, it is reported that the phase flow in the outer cavity zone is complex and some limited researches experimentally conclude that the cavity zone contributes substantially to the mass transfer. Also, no related CFD model has been developed for the outer cavity zone. Therefore, the models of the drag force, effective interfacial area, and liquid droplet diameter should be separately introduced for each zone in the RPB. As a result, the ratio of the mass transfer in the outer cavity zone to the overall mass transfer within the whole RPB should be evaluated.

(v) The comparison of the CPB and RPB should be conducted for commercial applications.

According to the literature review, the RPB has not been commercially applied for CO₂ absorption. The first reason is that there is no design procedure for scaling up the RPB

so far. Even if the large-scale RPB model has been established, how to operate this large-scale RPB is unknown as the CO₂ capture process may be different in multi-scale RPB, thus, the CO₂ capture performance should be investigated under various operating conditions. Furthermore, the advantage of the RPB over the CPB has not been thoroughly and clearly illustrated, therefore, the comparison of the CPB and RPB would be quantitatively evaluated in this thesis.

CHAPTER 3 : THEORIES AND METHODOLOGIES

Summary

This chapter introduced the Eulerian methods for simulating the gas-liquid flow characteristics and mass transfer process in the RPB. For investigating the CO₂ capture processes (hydrodynamics, thermodynamics, mass transfer) within the RPB, the governing equations, the drag force models, the dispersion force model, the effective interfacial area models for the non-uniform gas-liquid flows, the reaction-enhancement mass transfer model, the heat transfer model, and the liquid droplet diameter models are developed. In particular, the dispersion models are proposed for exploring the liquid dispersion in the packing region. In order to quantitatively evaluate the CO₂ capture in the packing and outer cavity zones, the drag force models, the effective interfacial area models, and the liquid droplet diameter models are separately illustrated for these two zones.

In Chapter 2, the Eulerian method with the porous medium model has been proven to be a promising approach to simulate the hydrodynamics and mass transfer in the RPB. The Eulerian porous medium model [6, 34] treats the gas and liquid as two continuous but penetrable phases. Also, the packing is considered as a porous medium and its effect on the flow could be computationally described by the drag force model and dispersion force model, which are illustrated in Section 3.3 and Section 3.4,

respectively. In addition, the effective interfacial area model for the non-uniform flow will be presented, see Section 3.5. According to the method and models employed, the flow dynamics in the packing region will be explored. Furthermore, the reaction-enhancement mass transfer model and heat transfer model are illustrated in Sections 3.6-3.8. As a result, the coupled model can realize the momentum, heat, and mass transfer between the phases, and accordingly, the hydrodynamics, thermodynamics, and CO₂ capture within the RPB can be explored.

Unlike most of the investigations on the RPB, in addition to the packing region, the study of the outer cavity zone is one of the research objectives of this thesis since some of the CO₂ is proven to be also captured in the outer cavity zone [42, 43, 96, 116]. In order to accurately model the hydrodynamics and mass transfer process within the entire RPB, the interfacial force model and the effective interfacial area model for the packing and outer cavity zones will be separately developed. The detailed method and models are given in the following sections.

3.1 Governing fluid flow equations

The continuity equation describing the overall mass conservation is expressed as follows:

$$\frac{\partial}{\partial t}(\varepsilon_i \rho_i) - \nabla \cdot (\varepsilon_i \rho_i \vec{u}_i) = S_{m,i} \quad (3-1)$$

where ρ_i is the density ($i = G$ for gas or L for liquid), t is the time, \vec{u}_i is the fluid velocity, $S_{m,i}$ is the mass transfer rate between phases, and ε_i is the phase fraction, which is defined as follows:

$$\varepsilon_i = \alpha_i \gamma = \frac{V_i}{V_G + V_L} \gamma = \frac{V_i}{V_G + V_L + V_S} \quad (3-2)$$

where α_i is the phase saturation ($\alpha_i = \frac{V_i}{V_G+V_L}$), V_i is the volume of the i th phase, the subscripts G, L, S indicate the gas, liquid, and solid phase, respectively, and γ and V_S are the porosity and solid volume of the packing, respectively, which are 1 and 0 for the outer cavity zone.

The momentum conservation equation includes the convection force, the pressure force, the viscous force, the body force, the drag force, the interfacial force, and the dispersion force. Therefore, the governing momentum equations of the fluid flow are as follows:

$$\begin{aligned} \frac{\partial}{\partial t} (\varepsilon_L \rho_G \vec{u}_L) + \nabla \cdot (\varepsilon_L \rho_L \vec{u}_L \vec{u}_L) = \\ -\varepsilon_L \nabla P + \varepsilon_L \nabla P_c + \nabla \cdot (\varepsilon \bar{\tau}_L) + \varepsilon_L \rho_L \vec{g} - \vec{F}_{drag,L} + \vec{F}_{GL} + \vec{F}_{disp,L} \end{aligned} \quad (3-3)$$

$$\begin{aligned} \frac{\partial}{\partial t} (\varepsilon_G \rho_G \vec{u}_G) + \nabla \cdot (\varepsilon_G \rho_G \vec{u}_G \vec{u}_G) = \\ -\varepsilon_G \nabla P + \nabla \cdot (\varepsilon \bar{\tau}_G) + \varepsilon_G \rho_G \vec{g} - \vec{F}_{drag,G} - \vec{F}_{GL} + \vec{F}_{disp,G} \end{aligned} \quad (3-4)$$

where P is the pressure, P_c is the capillary pressure, which is produced by the difference in the pressures across the fluid interface and only included in the liquid phase momentum equation, $\bar{\tau}_i$ is the stress tensor, \vec{g} is the gravitational force, $\vec{F}_{drag,i}$ is the drag force between the fluid and packing, \vec{F}_{GL} is the interfacial force between the gas and liquid, and $\vec{F}_{disp,i}$ is the dispersion force.

The species transport equation and energy equation are as follows:

$$\frac{\partial (\varepsilon_i \rho_i \vec{u}_i Y_{ij})}{\partial t} + \nabla \cdot (\varepsilon_i \rho_i \vec{u}_i Y_{ij}) = -\nabla \cdot (\varepsilon_i \vec{J}_{ij}) + \varepsilon_i R_{ij} \quad (3-5)$$

$$\frac{\partial(\varepsilon_i \rho_i E_i)}{\partial t} + \nabla \cdot (\varepsilon_i \vec{u}_i (\rho_i E_i + P)) = \varepsilon_i \nabla P \left(k'_{eff} \nabla T_i - \sum h_j \vec{J}_{ij} + (\bar{\tau}_{eff,ij} \cdot \vec{u}_i) \right) + \varepsilon_i Q_{h,i} + \varepsilon_i S_{h,i} \quad (3-6)$$

where Y_{ij} is the mass fraction of the species j in i th phase, such as the CO_2 in the gas phase or MEA in the liquid phase (j =species), R_{ij} is the production of the species j by the reaction, such as MEACOO^- ($\text{HOC}_2\text{H}_4\text{NHCOO}^-$), \vec{J}_{ij} is the mass diffusion flux, E_i is the total energy, T_i is the temperature of the phase, h_j is the enthalpy of the species, $\bar{\tau}_{eff,ij}$ is the effective shear tensor, $Q_{h,i}$ is the transferred heat between the phases, see Section 3.8, $S_{h,i}$ is the heat of the chemical reaction, and k'_{eff} is the effective thermal conductivity. Since the heat transfer between the fluid and packing is considered in the RPB model, thus, k'_{eff} is computed by volumetrically averaging the mean fluid conductivity and the solid conductivity, which is given as follows:

$$k'_{eff} = \gamma k'_F + (1 - \gamma) k'_S \quad (3-7)$$

where k'_F and k'_S are the thermal conductivities of the fluid and packing, respectively.

3.2 Liquid outlet setting methods

In reality, the liquid outlet tube is filled with the liquid phase all the time and almost no gas phase flows out from the liquid outlet. However, it is difficult to establish a gas inlet boundary and a liquid outlet boundary in Fluent when they overlap. In addition, a larger amount of the gas flow will flow out from the liquid outlet boundary if the pressure outlet boundary condition is employed. In order to avoid these problems, an elimination zone has been applied in order to prevent the gas phase from flowing out from the liquid outlet. The mass, momentum, species and energy for the liquid phase in the elimination

zone can be removed during a one-time step, and meanwhile, the gas phase can be retained. The appropriate source equations for this zone are described as follows:

For the liquid mass source,

$$S_M = -\frac{\rho_L \varepsilon_L}{\Delta t} \quad (3-8)$$

For the liquid momentum source,

$$\vec{S}_U = -\frac{\rho_L \varepsilon_L}{\Delta t} \vec{u}_L \quad (3-9)$$

For the species source,

$$S_J = -\frac{\rho_L \varepsilon_L}{\Delta t} Y_{Lj} \quad (3-10)$$

For the energy source,

$$S_H = -\frac{\rho_L \varepsilon_L}{\Delta t} h_L \quad (3-11)$$

where S_M , \vec{S}_U , S_J , S_H are the source terms of the mass, momentum, species, and energy, respectively, Δt is the current timestep set in Fluent. If the elimination zone is employed in the RPB model, S_M , \vec{S}_U , S_J , S_H should be respectively added to the equations of the mass, momentum, species, and energy for the liquid phase.

3.3 Porous resistance force and interfacial force models

Due to the stacked wire mesh matrix in the packing region, the forces acting on the phases are clearly different in the packing and outer cavity zones. Therefore, the force models for the packing region and outer cavity zone should be separately introduced.

3.3.1 Porous resistance in the packing region

Resolving the complex geometry of the packing structure at the pore scale is computationally not feasible. Instead, the packing structure is replaced with an effective porous medium. It is very important to determine the correct resistance force model for the porous medium in order to describe the gas-liquid interfacial force and phase-solid drag force accurately, since the packing could substantially influence the liquid holdup and the pressure drop [125]. Although various porous medium resistance force models, such as those for spherical packing [122, 143, 144], structured slit packing [123], and tube bundle packing [124], have been proposed, Lu et al. [34] have illustrated that these models failed to predict the practical liquid holdup in the wire mesh packing, thus indicating that these models were not suitable for the RPBs [127]. In 2009, Kołodziej and Łojewska [125] proposed a one-phase model that takes into account both the viscous and inertia contributions to the overall resistance of the wire meshed porous media, based on single flow experiments through wire gauzes, which is similar to that of the flow through a wire mesh packing in RPBs. Subsequently, Kołodziej et al. [126] introduced another form of the porous resistance model by redefining the effective length and effective velocity of the liquid flow in the packing region, and suggested the following pressure drop equations:

$$\frac{\Delta P}{L} = 4(f_l + f_t) \frac{\rho u_0^2}{2d_w} \frac{1 - \gamma}{\gamma^3} \frac{\tau^2}{\cos\theta} \quad (3 - 12 - a)$$

$$L_e = \frac{L}{\cos\theta}, u_e = \frac{u_0 \tau}{\gamma} \quad (3 - 12 - b)$$

where ΔP is the pressure drop, L and L_e are the length/depth of the packing and the effective flow length, respectively, u_0 and u_e are the superficial velocity and effective

velocity, respectively, f_l and f_t are the Fanning factors for the laminar and turbulent flows, respectively, d_w is the diameters of the dry wires, τ is the tortuosity factor resulting from the tortuous path that the fluid passes through, θ is the angle between the axis of the packing and the direction of the fluid flow. This resistance model is a good improvement over the previous model [125] proposed by Kołodziej and Łojewska because the liquid residence time ($t = \frac{L_e}{u_e} = \frac{L\gamma}{u_0 \cos\theta\tau}$) usually increases after considering the influence of the tortuous path and the orientation of the packing. Also, it is proved that using this model produces results which are in much better agreement with the experimental data [127].

When the liquid passes through the packing region in the RPB, the liquid phase exists in the forms of both liquid film on the packing surface and liquid droplets in the void of packing, the surface of the film and droplets per unit volume of packing is noted as the wet specific area ($a_s \times f_{e,p}$), and the remaining area of the packing is covered by the gas, noted by the dry specific area, $a_s \times (1 - f_{e,p})$. $f_{e,p}$ is the fraction of the effective interfacial area of the packing, and it is defined as the ratio of the wet specific area $A_{e,p}$ to the total packing specific area:

$$f_{e,p} = \frac{A_{e,p}}{a_s} \quad (3 - 13)$$

The effective interfacial area $A_{e,p}$ needs to be modelled and this will be discussed later in Section 3.5.

The drag force between the gas and the solids, the liquid and the solids, as well as the interfacial force between the gas and the liquid can be expressed as follows [6, 34, 125]:

$$\vec{F}_{drag,L} = K_{LS}\vec{v}_L = f_{e,p}\varepsilon_L\vec{v}_L \left[4(f_l + f_t) \frac{\rho_L|\vec{v}_L|\varepsilon_S}{2d_w \varepsilon_L \cos\theta} \tau^2 \right] \quad (3-14)$$

$$\vec{F}_{drag,G} = K_{GS}\vec{v}_G = (1 - f_{e,p})\varepsilon_G\vec{v}_G \left[4(f_l + f_t) \frac{\rho_G|\vec{v}_G|(1 - \varepsilon_G)}{2d_w \varepsilon_G \cos\theta} \tau^2 \right] \quad (3-15)$$

$$\vec{F}_{GL} = K_{GL}(\vec{v}_G - \vec{v}_L) = f_{e,p}\varepsilon_G(\vec{v}_G - \vec{v}_L) \left[4(f_l + f_t) \frac{\rho_G|\vec{v}_G - \vec{v}_L|(1 - \varepsilon_G)}{2d_w \varepsilon_G} \tau^2 \right] \quad (3-16)$$

$$f_l = \frac{1}{Re_K} \left(\frac{3.44}{\sqrt{\mathcal{X}^+}} + \frac{\frac{1.25}{4\mathcal{X}^+} + 16 - \frac{3.44}{\sqrt{\mathcal{X}^+}}}{1 + \frac{0.00021}{\mathcal{X}^{+2}}} \right) \quad (3-17)$$

$$f_t = \frac{0.079}{Re_K^{0.25}} \quad (3-18)$$

$$\mathcal{X}^+ = \frac{d_w}{D_h Re_K} \quad (3-19)$$

$$Re_K = \frac{\rho v_e D_h}{\mu} \quad (3-20)$$

For the fluid-solids interaction:

$$\tau = 1 + \frac{\varepsilon_S}{2}, d_w = \frac{4\varepsilon_S}{a_S}, v_e = |\vec{v}_i|\tau, D_h = \frac{4\varepsilon_i}{a_S} \quad (3-21)$$

For the gas-liquid interaction:

$$\tau = 1 + \frac{\varepsilon_S + \varepsilon_L}{2}, d'_w = \frac{4\varepsilon_S}{a'_S}, v_e = |\vec{v}_G - \vec{v}_L|\tau, D_h = \frac{4\varepsilon_G}{a'_S}, a'_S = \left(\frac{\varepsilon_S}{\varepsilon_S + \varepsilon_L} \right)^{0.5} a_S \quad (3-22)$$

where $\vec{F}_{drag,G}$, $\vec{F}_{drag,L}$ and \vec{S}_{GL} are the drag forces between the gas and the solids, the liquid and the solids and the interfacial force between the gas and the liquid, respectively; K_{GS} , K_{LS} and K_{GL} are the porous resistance coefficients between the gas and the solids, the liquid and the solids and the momentum exchange coefficient

between the gas and the liquid, respectively; d'_w is the diameter of the wet wires, D_h is the hydraulic diameter, Re_K is the Reynold number, \vec{v}_i and \vec{v}_e are the local velocity and effective velocity relative to the rotating packing, respectively; μ is the dynamic viscosity, and a_s and a'_s are the specific area of the dry packing and the wet packing, respectively.

It is worth noting that the angle between the flow direction and the bed axis (θ) is a critical parameter for describing the porous resistance in the packing. Nevertheless, this parameter is difficult to achieve by the experimental approach. According to the literatures [125, 126], it is reported that the value of θ is determined by the equation: $\tan(\theta) = d_w/M$ (M is the centre distance between the wire mesh). Thus, θ is set as 10° in this thesis, which is determined by a commonly used specification of the wire meshes with the wire mesh diameter and the centre distance between the wire mesh being 0.6 and 3.5 mm, respectively. Also, this value has been employed in the work of Zhang et al. [37].

In order to clearly illustrate the calculation process of the porous resistance within the packing region, a flowchart is provided to elucidate the application of the above equations.

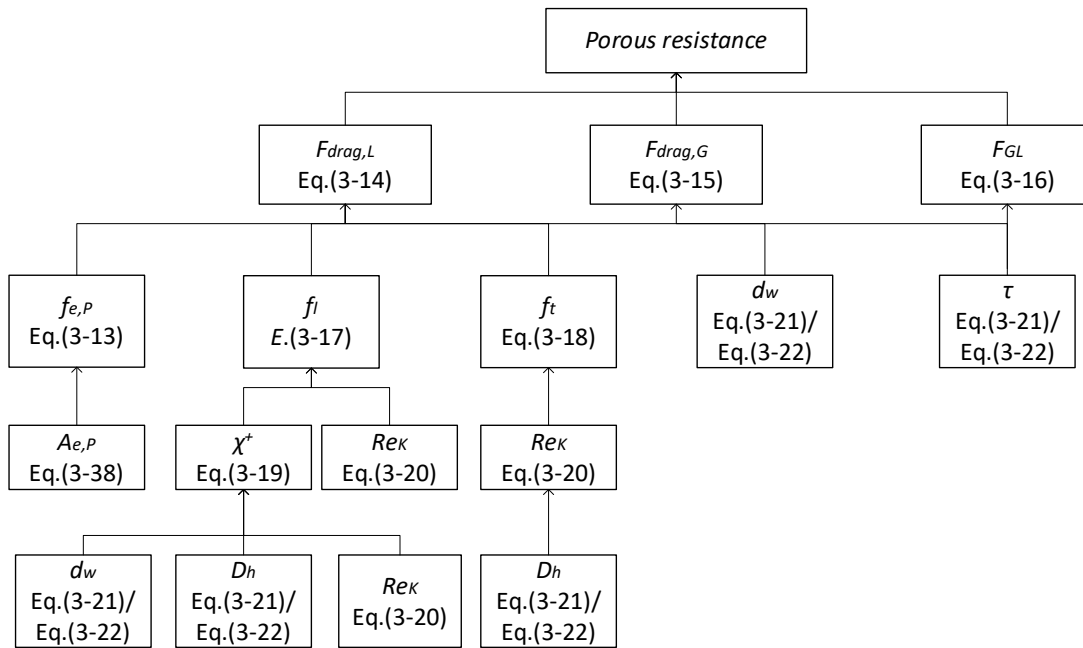


Figure 3-1 The calculation procedure for the porous resistance.

3.3.2 Interfacial force in the outer cavity zone

The interfacial force is the only force that is considered in the outer cavity zone for the liquid and gas phases. This is due to the momentum exchange between the gas phase and liquid phase and this force is usually presented as an exchange coefficient in Ansys Fluent. There are many built-in models to calculate the interfacial exchange coefficient and a model, named universal drag laws [145], has been designed for the bubble-liquid and droplet-gas flows that could be utilized for achieving the interfacial exchange coefficient in the outer cavity zone, namely

$$K_{GL} = \frac{\varepsilon_G \varepsilon_L \rho_L f}{\tau_L} \quad (3-23)$$

$$\tau_L = \frac{\rho_L d_p^2}{18\mu_G} \quad (3-24)$$

$$f = \frac{C_D Re}{24} \quad (3-25)$$

$$Re' = \frac{\rho_G |\bar{u}_G - \bar{u}_L| d_p}{\mu_e} \quad (3-26)$$

$$C_D = \begin{cases} \frac{24}{Re'}, Re' < 1 \\ \frac{24}{Re'} (1 + 0.1 Re'^{0.75}), 1 \leq Re' \leq 1000 \\ \frac{2}{3} \left(\frac{d_p}{\lambda_{RT}} \right) \left\{ \frac{1 + 17.67 f^{*6/7}}{18.67 f^*} \right\}^2, Re' > 1000 \end{cases} \quad (3-27)$$

$$f^* = (1 - \varepsilon_L)^3; \mu_e = \frac{\mu_G}{(1 - \varepsilon_L)^{2.5}}; \lambda_{RT} = \left(\frac{\sigma}{g \Delta \rho_{GL}} \right)^{0.5} \quad (3-28)$$

where f and f^* are the drag functions, τ_L is the particulate relaxation time, C_D is the drag coefficient, Re' is the relative Reynolds number, μ_e is the effective viscosity, λ_{RT} is the Rayleigh-Taylor instability wavelength, and $\Delta \rho_{GL}$ is the absolute value of the density difference between the liquid and gas phases.

3.4 Dispersion force models

As mentioned in Section 3.1, in two-phase flows through porous media, the dispersion terms appear in the governing fluid flow equations due to the volume averaging of the momentum equations. In order to employ the Eulerian porous medium model to investigate the liquid dispersion, a dispersion model needs to be devised to calculate the dispersion force term as a consequence of the volume averaging in the momentum equations [128]. Currently, there has been no dispersion model developed specifically for RPBs. However, various such models have been proposed for the modelling of the liquid dispersion in the CPBs. Although the porous media packing types, the nature of the packing types, the driving force and the flow patterns are different in the CPB and

RPB, we take the view that both CPB and RPB are similar in that they both can be regarded as being a porous media and the liquid disperses from a higher volume fraction to a lower volume fraction under the framework of the porous medium approach. The macro dispersion mechanisms are similar in RPBs and CPBs. Hence, it is expected that these dispersion models for CPBs could be employed in RPBs with careful evaluations. The dispersion terms mainly result from two distinct mechanisms: capillary pressure and mechanical dispersion. Popular models for these two mechanisms for CPBs, and also assessed in this section for the RPB, are as follows:

3.4.1 Capillary pressure

For the capillary pressure, in general, two models have been used, i.e. the Grosser model and the Attou and Ferschneider model. The model of Grosser et al. [146] was introduced through a permeability concept based on the Leverett's function. The Attou and Ferschneider model [143] considers the loss of stability of the liquid film on the particle surface at the pore scale. The Grosser and Attou capillary pressure models are presented in Equations (3-29) and (3-30), respectively, as follows:

$$P_c = \frac{1 - \gamma}{\gamma d_w} \sqrt{180} \sigma \left[0.48 + 0.036 \ln \left(\frac{1 - \varepsilon_S - \varepsilon_L}{\varepsilon_L} \right) \right] \quad (3 - 29)$$

$$P_c = 2\sigma \left(\frac{1 - \gamma}{1 - \varepsilon_G} \right)^{\frac{1}{3}} \left(\frac{1}{d_w} + \frac{1}{d_{min}} \right) F \left(\frac{\rho_G}{\rho_L} \right) \quad (3 - 30 - a)$$

$$d_{min} = \left(\frac{\sqrt{3}}{\pi} - \frac{1}{2} \right)^{\frac{1}{2}} d_w \quad (3 - 30 - b)$$

$$F \left(\frac{\rho_G}{\rho_L} \right) = 1 + 88.1 \left(\frac{\rho_G}{\rho_L} \right) \left(\text{for } \frac{\rho_G}{\rho_L} < 0.025 \right) \quad (3 - 30 - c)$$

where σ is the surface tension, and d_{min} is the characteristic diameter. Further, these

models can be modified by considering the fraction of the effective interfacial area of the packing, $f_{e,p}$ [147] as follows:

$$P_G - P_L = (1 - f_{e,p})P_c \quad (31)$$

where $P_G - P_L$ is the modified capillary pressure between the gas and liquid phase. These models have been used to analyze the effect of the capillary pressure on the radial liquid distribution in CPBs [128, 129, 148, 149]. However, most investigators tend to ignore the capillary pressure due to the large particle size and high packing porosity [130] in the CPB, and the mechanical dispersion was the only dispersion force that has been considered in their investigations [112-114]. However, in the RPB model, the effect of the capillary pressure on the liquid dispersion would be taken into account. This consideration is important because the diameter of the wire mesh is typically small, and the packing porosity employed in Section 5 is relatively low, with a value of 0.801.

3.4.2 Mechanical dispersion

Liu and Long [150], Mewes et al. [151] and Lappalainen et al. [152] have proposed many mechanical dispersion models for the CPBs. Among these models, the model proposed by Lappalainen et al. [152] is the most popular, and it has been employed in many works for the CPB simulations [112-115]. This model was initially derived based on spherical particle packings, and then it was proven to be suitable for structured packings [123, 130], thus indicating that this model has a wide range of adaptability to model the flow in different types of packings. Hence, the original model of Lappalainen et al. [152] is considered in this thesis to take into account the liquid dispersion in the RPB, which can be expressed as follows:

$$\vec{F}_{D,G} = K_{GS}\vec{v}_{D,G} + K_{GL}(\vec{v}_{D,G} - \vec{v}_{D,L}) \quad (3-32)$$

$$\vec{F}_{D,L} = K_{LS}\vec{v}_{D,L} - K_{GL}(\vec{v}_{D,G} - \vec{v}_{D,L}) \quad (3-33)$$

where $\vec{F}_{D,i}$ is the mechanical dispersion force for the i th phase, and $\vec{v}_{D,i}$ is the drift velocity for the i th phase.

Based on the Fickian assumption, the drift velocity is a function of the gradient of the phase volume fraction and a spread factor, S_f . It can be written as follows:

$$\vec{v}_{D,L} = -\frac{S_f}{\varepsilon_L} \left(|\vec{v}_L| \nabla \varepsilon_L - (\vec{v}_L \cdot \nabla \varepsilon_L) \frac{\vec{v}_L}{|\vec{v}_L|} \right) \quad (3-34)$$

$$\vec{v}_{D,G} = -\frac{S_f}{\varepsilon_G \alpha_G} \left(|\vec{v}_G| \nabla \varepsilon_G - (\vec{v}_G \cdot \nabla \varepsilon_G) \frac{\vec{v}_G}{|\vec{v}_G|} \right) \quad (3-35)$$

$$S_f = 0.231 d_w^{0.5} \sigma \quad (3-36)$$

where $\nabla \varepsilon_i$ is the spatial gradient of the phase volume fraction.

Compared with the liquid dispersion force, the gas dispersion force is very small and has little effect on the liquid flow dynamics. More importantly, there is no forced gas flow in the RPB model used in Chapter 4; therefore, the gas dispersion force (equation (3-32)) may be neglected [130]. Furthermore, since the gas-liquid momentum exchange coefficient K_{GL} in Equations (3-15) and (3-16) is extremely small compared with the liquid-solid porous resistance coefficient K_{LS} , Equation (3-33) can be reduced to

$$\vec{F}_{D,L} = K_{LS}\vec{v}_{D,L} \quad (3-37)$$

This is the most important force term in the liquid mechanical dispersion force, which has been verified in previous numerical studies [130].

3.5 Gas-liquid effective interfacial area models

The effective interfacial area is a crucial parameter for forecasting the transfers of mass, momentum, and energy across the interface between the phases. It is influenced by the fluid flow characteristics that is presented in the RPB. Since the characteristics of the multiphase flow are quite different when passing through the rotating packing and in the static cavity space, similar to the drag force, the effective interfacial area models in the packing and outer cavity zones should be, respectively, presented.

3.5.1 Effective interfacial area in the packing zone

The gas-liquid effective interfacial area is a critical parameter that has to be modelled when using porous medium models since it not only influences the flow dynamics, but also affects the mass transfer performance.

In our recent publication, Xie et al. [31] have estimated the effective interfacial area when the liquid flows over a RPB packing material using the VOF modelling method by considering a range of different gravitational acceleration forces and liquid viscosities. The model has been validated against experimental observations and a correlation for the effective interfacial area was proposed as follows:

$$A_{e,P} = 202.3485 \left(\frac{g_c}{g_1}\right)^{0.0435} \left(\frac{U}{U_1}\right)^{0.4275} \left(\frac{\nu}{\nu_1}\right)^{0.1200} \left(\frac{\beta}{\beta_1}\right)^{-0.5856} \quad (3 - 38)$$

where the experimental constants $g_1 = 205.6 \text{ m/s}^2$, $U_1 = 0.0106 \text{ m/s}$, $\nu_1 = 3.35 \times 10^{-6} \text{ m}^2/\text{s}$ and $\beta_1 = 75^\circ$; g_c is the central pedal acceleration, U is the average superficial liquid velocity, ν is the kinematic viscosity of the liquid, and β is the dynamic contact angle, which is determined by the packing surface and liquid property. When the dynamic contact angle (β) in the effective interfacial area model is set as 12° , the

modelled fractional effective interfacial area for the cases simulated in the following sections is in the reasonable range of 0.29-0.68 [44, 96] and the liquid holdup and the CO₂ capture coefficient matches the experimental data well. Therefore, this correlation will be employed in this thesis and the average superficial velocity should be replaced by the local superficial velocity to fit the non-uniform flows as follows:

$$U = \varepsilon_L |\vec{v}_L| \quad (3 - 39)$$

In addition, within the packing bed, the method given by [6] has been employed to calculate the effective interfacial area in the cell next to the packing wall as follows:

$$A_{e,PW} = \frac{A_{PW}f_{e,P} + a_s f_{e,P} V_{cell,PW}}{V_{cell,PW}} = \left(\frac{1}{\Delta x_{PW}} + a_s \right) f_{e,P} \quad (3 - 40)$$

where $A_{cell,PW}$ and $V_{cell,PW}$ are the wall surface area and volume of the cell next to the packing wall, respectively, Δx_{PW} is the radial length of the cell normal to the packing wall, a_s is the specific area of the packing, f_e is the fractional effective interfacial area in the packing, which is the ratio of the wet specific area to the total packing specific area ($\frac{A_{e,P}}{a_s}$), and $f_{e,P}$ of the packing walls is considered to be the same as that in the packing region.

3.5.2 Effective interfacial area in the outer cavity zone

At present, no correlation of the effective interfacial area has been introduced for the outer cavity zone of the RPBs in the published papers. The liquid phase exits in the form of the liquid droplets in the outer cavity space and the liquid film on the casing wall. For a spherical bubble or droplet, the algebraic interfacial area concentration models are derived from the surface area to volume ratio ($A_e = \frac{\pi d_p^2}{\frac{1}{6}\pi d_p^3} = \frac{6}{d_p}$). When using

the Eulerian multiphase model, a commonly used equation, as given in Equation (3-40), could be utilized to estimate the effective interfacial area for the liquid droplets in the outer cavity space, which has been built in Fluent ia-symmetric model.

$$A_{e,o} = \frac{6\varepsilon_G\varepsilon_L}{d_{p,o}} \quad (3 - 41)$$

where $A_{e,o}$ is the effective interfacial area in the outer cavity zone, $d_{p,o}$ is the average diameter of the liquid droplets in the outer cavity zone. The ia-symmetric model not only considers the gas and liquid volume fraction, but also takes into account the liquid diameter. In the experimental work of Sang et al. [116], they concluded that the liquid exists in the outer cavity zone mainly in the form of droplets and a correlation of the average droplet diameter in the outer cavity zone has been proposed as follows [116]:

$$d_{p,o} = 0.042We^{-0.272}Re^{0.068}\left(\frac{u_0}{\omega r_o}\right)^{0.098}r_o \quad (3 - 42)$$

$$We = \frac{\rho\omega^2r_o^3}{\sigma}; Re = \frac{\rho\omega r_o^2}{\mu}; q = \frac{u_0}{\omega r_o}; u_0 = \frac{Q_L}{2\pi r_i h} \quad (3 - 43)$$

where We is the Weber number, Re is the Reynolds number with outer packing radius as the characteristic linear dimension, ω is the angular velocity, Q_L is the liquid volumetric flow rate, q is the dimensionless liquid initial velocity, and r_o , r_i and h are the outer radius, inner radius and height of the packing, respectively.

Because the liquid on the casing wall exists in the form of the liquid film instead of the liquid droplet, Equations (3-41)-(3-43), which are developed for the liquid droplets in the outer cavity space, cannot be used for estimating the effective interfacial area between the gas and the liquid film near the casing wall. If the casing wall surface is

fully covered by the liquid film, then the effective interfacial area in the cell next to the casing wall ($a_{e,OW}$) is estimated as follows:

$$A_{e,OW} = \frac{A_{cell,OW}}{V_{cell,OW}} = \frac{1}{\Delta x_{OW}} \quad (3 - 44)$$

where $A_{cell,OW}$ and $V_{cell,OW}$ are the wall area surface and volume in the computational cell next to the casing wall, respectively, and Δx_{OW} is the radial length of the cell normal to the casing wall. For the case studied in Chapter 5, the radial length Δx_{OW} is 0.005 m, thus, the effective interfacial area near the casing wall is no more than 200 m²/m³. According to Equation (3-44), it appears that the maximum effective interfacial area ($A_{e,OW}$) depends on Δx_{OW} . Nevertheless, it should be noted that the unit of the effective interfacial area ($A_{e,OW}$) is m²/m³. The real physical mass transfer area (m²) could be obtained by $A_{OW} = A_{e,OW}V_{cell,OW} = A_{cell,OW}$, which is independent on the first-layer mesh size at the wall.

3.6 Mass transfer model

The two-film theory has by far been the most popular and useful theory for dealing with the CO₂ mass transfer among the phases [111-115]. Generally, based on the two-film model and the Henry law, the overall mass transfer coefficient and enhancement factor are applied to express the mass transfer between the two phases, which can be expressed as follows:

$$S_{m,i} = K_L A_e (C_{CO_2}^* - C_{CO_2}) \quad (3 - 45)$$

$$\frac{1}{K_L} = \frac{RT}{H_{CO_2-MEA} k_G} + \frac{1}{E k_L} \quad (3 - 46)$$

where $S_{m,i}$ is the CO₂ mass transferred through the gas-liquid interface, K_L is the

overall mass transfer coefficient, k_G and k_L are the mass transfer coefficients in the gas and liquid phases, respectively, R is the gas constant, H_{CO_2-MEA} is the Henry constant, E is the enhancement factor, which is defined as the ratio of the absorption rate with and without chemical reaction [153], and $C_{CO_2}^*$ and C_{CO_2} are the CO_2 concentrations on the surface of the liquid and in the liquid bulk flow, respectively. In particular, H_{CO_2-MEA} , E and $C_{CO_2}^*$ have been adequately illustrated in many works [6, 100, 114], so that these factors are expressed in Table 3-1 along with some other important parameters.

Since the CO_2 mass transfer resistance between the gas and liquid is dominated by the liquid side, the CO_2 mass transfer resistance in the gas side, the mass transfer resistance in the gas side is neglected. Therefore, Equation (3-46) may be simplified as the following equation:

$$\frac{1}{K_L} = \frac{1}{Ek_L} \quad (3 - 47)$$

Based on the film theory assumption, the mass transfer coefficient in the film theory is given as follows:

$$k_L = \frac{D_{L,CO_2}}{\delta} \quad (3 - 48)$$

where D_{L,CO_2} is the diffusivity of the CO_2 in the liquid phase, which could be estimated by the N_2O analogy method [154] and given in Table 3-1, and δ is the diffusion layer thickness for the mass transfer.

Table 3-1 Some of the correlations utilized in the current study.

Equation name	Equations	Eq. No.	Refer ence
Diffusivity of the MEA	$D_{L,MEA} = \exp\left(-13.275 - \frac{2198.3}{T} - 0.078142C_{L,MEA}\right)$	T-3-1	[155]
	$D_{L,CO_2} = D_{L,N_2O} \frac{D_{w,CO_2}}{D_{w,N_2O}}$	T-3-2	
Diffusivity of CO ₂ in the MEA solution	$D_{w,CO_2} = 2.35 \times 10^{-6} \exp\left(-\frac{2119}{T}\right)$	T-3-3	
	$D_{w,N_2O} = 5.07 \times 10^{-6} \exp\left(-\frac{2371}{T}\right)$	T-3-4	[154]
	$D_{L,N_2O} = 5.07 + 0.865C_{MEA} + 0.278C_{MEA}^2 \exp\left(-\frac{2371 - 93.4C_{MEA}}{T}\right)$	T-3-5	
Enhancement factor	$E = 1 + ((E_i - 1)^{-1.35} + (E_1 - 1)^{-1.35})^{-\frac{1}{1.35}}$	T-3-6	[156]
	$E_i = 1 + \frac{D_{L,MEA}C_{L,MEA}}{2D_{L,CO_2}C_{L,CO_2}}$	T-3-7	
	$E_1 = \frac{Ha}{\tanh(Ha)}$	T-3-8	[153]
	$Ha = \sqrt{\frac{k_2 D_{L,CO_2} C_{L,MEA}}{(k_L)^2}}$	T-3-9	
	CO ₂ saturation concentration	$C_{L,CO_2}^* = M_{CO_2} \frac{P_{CO_2}}{H_{CO_2-L}}$	T-3-10
Henry constant of the CO ₂	$H_{CO_2-L} = H_{N_2O-L} \left(\frac{H_{CO_2-H_2O}}{H_{N_2O-H_2O}} \right)$	T-3-11	
	$H_{CO_2-H_2O} = \exp\left(145.369 - \frac{8172.355}{T} - 19.303\right)$	T-3-12	
	$H_{N_2O-H_2O} = \exp\left(158.245 - \frac{9048.596}{T} - 20.86 \ln T - 0.00252\right)$	T-3-13	
	$H_{N_2O-MEA} = \exp\left(-9172.5 + \frac{39.598}{T}\right)$	T-3-14	[157]
	$H_{N_2O-L} = H_{N_2O-H_2O} C_{L,H_2O} + H_{N_2O-MEA} C_{L,MEA} + 3524641.533(C_{L,H_2O} C_{L,MEA})^2 \left(1 - \frac{T}{324.718}\right) \exp(-13.219C_{L,MEA})$	T-3-15	

Guo et al. [71] and Munjal et al. [73] proposed the correlations for predicting the film thickness for the RPBs, which are shown in Equations (3-49) and (3-50), respectively.

$$\delta = 4.20 \times 10^8 \frac{Q_L}{2\pi r h} \frac{v_L}{\omega^2 r} \quad (3-49)$$

$$\delta = \left(3 \left(\frac{Q_L}{2\pi r} \right) \frac{v_L}{r \omega^2} \right)^{\frac{1}{3}} \quad (3-50)$$

where r is the radial distance, h is the height of the packing. For the operating condition in the simulations, the enhancement factor (E) is approximately equal to the Hatta number (Ha) when the reaction is in the fast reaction regime ($5 \leq Ha \ll E_i$) due to the high MEA concentration and the small CO_2 partial pressure given by Equations (T-3-6) and (T-3-8) [158-160]. As a result, $K_L = Ek_L \approx E_1 k_L \approx Hak_L = \sqrt{\frac{k_2 D_{L,CO_2} C_{L,MEA}}{(k_L)^2}} k_L = \sqrt{k_2 D_{L,CO_2} C_{L,MEA}}$, which means that the overall mass transfer rate is almost independent of the layer thickness. In addition, this conclusion is consistent with that drawn by Lu et al. [6]. Therefore, either of these equations could be utilized in this work and Equation (3-49) is selected in this thesis as this equation is driven from the wire mesh [71], which is also the experimental packing material used in the experiments [161].

In order to clearly illustrate the calculation process of the amount of the transferred CO_2 , a flowchart is provided to elucidate the application of the above equations.

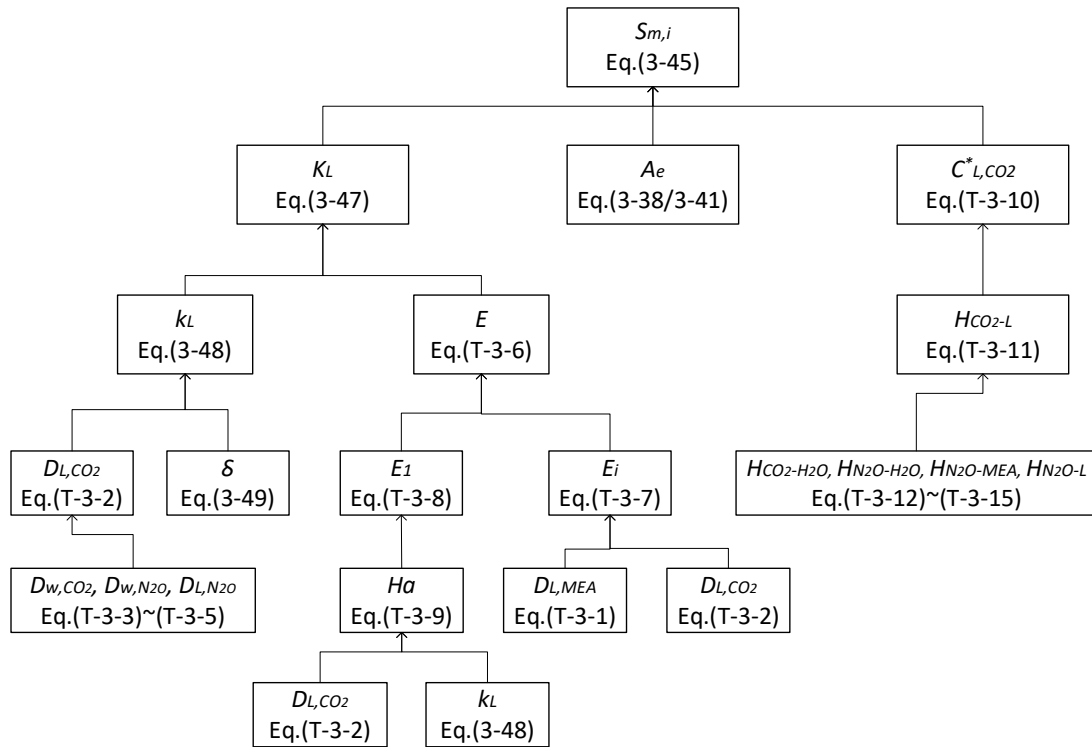


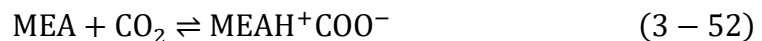
Figure 3-2 The calculation procedure for the mass transfer.

3.7 Chemical reaction rate

The CO₂-MEA chemical system can be described by the zwitterion mechanism [162], and the overall reaction between CO₂ and MEA is expressed as follows [100]:



The above reaction could be separated into two-step reactions. According to the zwitterion mechanism, the zwitterion ion (MEAH⁺COO⁻) is generated as an intermediate product through the reaction between CO₂ and MEA [163]. Then, this zwitterion undergoes deprotonation by a base (MEA) to yield carbamate (MEACOO⁻) [164], and the two-step reactions are as follows:





Reaction (3-53) has a finite rate and can be implemented in Ansys Fluent through the utilization of UDFs as source terms. Reaction (3-53) (i.e. carbamate formation) serves as the controlling step and describes the whole reaction kinetics [153, 165]. It can be regarded as a second-order irreversible reaction, and the reaction rate can be written as [166]:

$$r_{\text{CO}_2} = -k_2[\text{MEA}][\text{CO}_2] \quad (3 - 54)$$

where k_2 is the reaction rate constant. Various reaction rate constants for the CO_2 captured by the MEA solution have been proposed based on various experimental conditions [160, 166-169].

Among them, the reaction rate proposed by Versteeg et al. [170] has been validated by Ying and Eimer [160] and used in many studies [158, 160], which is given as follows:

$$k_2 = 4.4 \times 10^{11} \exp\left(-\frac{5400}{T}\right) \quad (3 - 55)$$

On the other hand, the high temperature may lead to the release of the CO_2 , and the backward reaction and reaction rate constant is given as follows [171]:



$$k_b = 4.8531 \times 10^{23} \exp\left(-\frac{102740}{T}\right) \quad (3 - 57)$$

3.8 Heat transfer model

The transferred heat between the two phases is a function of the temperature difference and the effective interfacial area:

$$Q_{h,GL} = h_{GL}A_e(T_L - T_G) \quad (3 - 58)$$

where $Q_{h,GL}$ is the transferred heat between the gas and liquid, and h_{GL} is the heat transfer coefficient. Here, a commonly used model-Hughmark model [172]-was utilized to calculate the heat transfer coefficient between the gas and the liquid, namely

$$h_{GL} = \frac{\kappa_G Nu_L}{d_p} \quad (3 - 59)$$

$$Nu_L = \begin{cases} 2.0 + 0.6Re_L^{\frac{1}{2}}Pr_G^{\frac{1}{3}} & 0 \leq Re_L < 776.06, 0 \leq Pr_G < 250 \\ 2.0 + 0.27Re_L^{0.62}Pr_G^{\frac{1}{3}} & 776.06 \leq Re_L, 0 \leq Pr_G < 250 \end{cases} \quad (3 - 60)$$

$$Pr_G = \frac{C_{pG}\mu_G}{\kappa_G} \quad (3 - 61)$$

where κ_G is the thermal conductivity of the gas phase, Nu_L is the Nusselt number of the liquid phase, Pr_G is the Prandtl number of the gas phase, and C_{pG} is the specific heat. The heat transfer in the RPB is determined by the heat transfer rate, which is inversely proportional to the liquid droplet diameter according to Equation (3-59). The larger the liquid droplet diameter, the lower is the heat transfer rate, which means that more heat could be retained in the liquid phase. As a result, the liquid temperature changes and the CO₂ capture performance is changed. Therefore, the liquid droplet diameter is a critical parameter for the CO₂ absorption, and this parameter in the packing region and outer cavity zone should be carefully modelled. In particular, the diameter of the liquid droplets in the outer cavity zone [116] are shown in Equation (3-42), whereas the diameter in the packing region has been regressed as two correlations based on the same set of the experimental data [78], namely [71, 75]:

$$d_{p,P} = 0.7284 \left(\frac{\sigma}{\omega^2 r \rho} \right)^{0.5} \quad (3-62)$$

$$d_{p,P} = 12.84 \left(\frac{\sigma}{\omega^2 r \rho} \right)^{0.630} u^{0.201} \quad (3-63)$$

where r is the radial coordinate of the packing from the centre, and u is the liquid flow rate per unit area, which is only included in Equation (3-62). Since the liquid diameter is influenced by the liquid flow rate u , Equation (3-62) could more accurately predict the diameter of the liquid droplets in the packing region. Thus, Equation (3-62) has been utilized in this thesis.

3.9 Conclusion

In this chapter, the Eulerian porous medium method has been introduced for effectively investigating the physical and chemical performance in the RPB. In addition, the governing equations, the drag force models, the dispersion force model, the effective interfacial area models for the non-uniform gas-liquid flows, the reaction-enhancement mass transfer model, and the heat transfer model, have been introduced in order to study the hydrodynamics, thermodynamics, mass transfer inside the entire RPB. In particular, the drag force models, the effective interfacial area models, and the liquid droplet diameter models have been separately illustrated for packing and outer cavity zones to quantitatively evaluate the CO₂ capture in these zones.

To enhance comprehension of the sub-models utilized in the upcoming three chapters, three flowcharts have been incorporated to visually depict the specific sub-models employed in Chapter 4, Chapter 5, and Chapter 6, respectively.

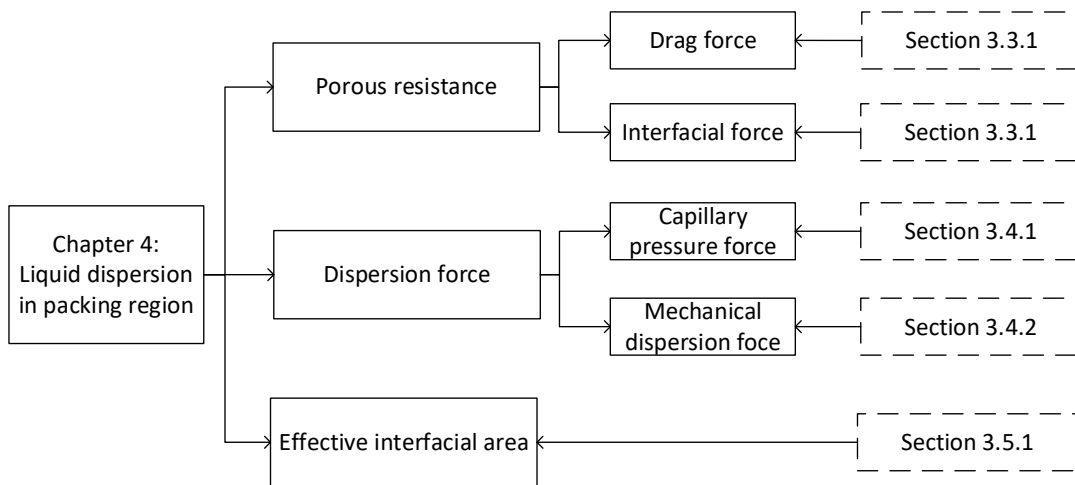


Figure 3-3 The sub-models employed in Chapter 4.

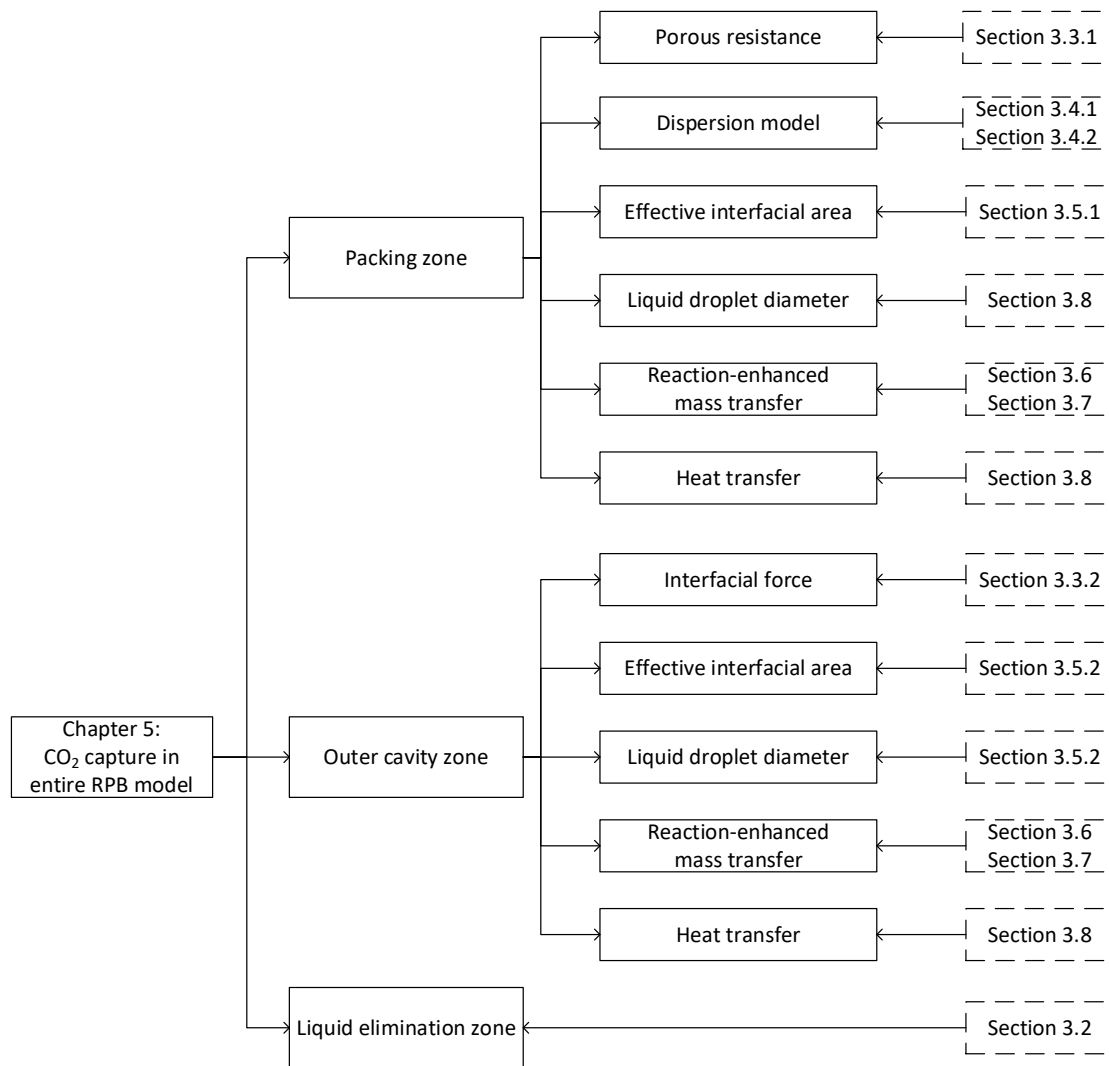


Figure 3-4 The sub-models employed in Chapter 5.

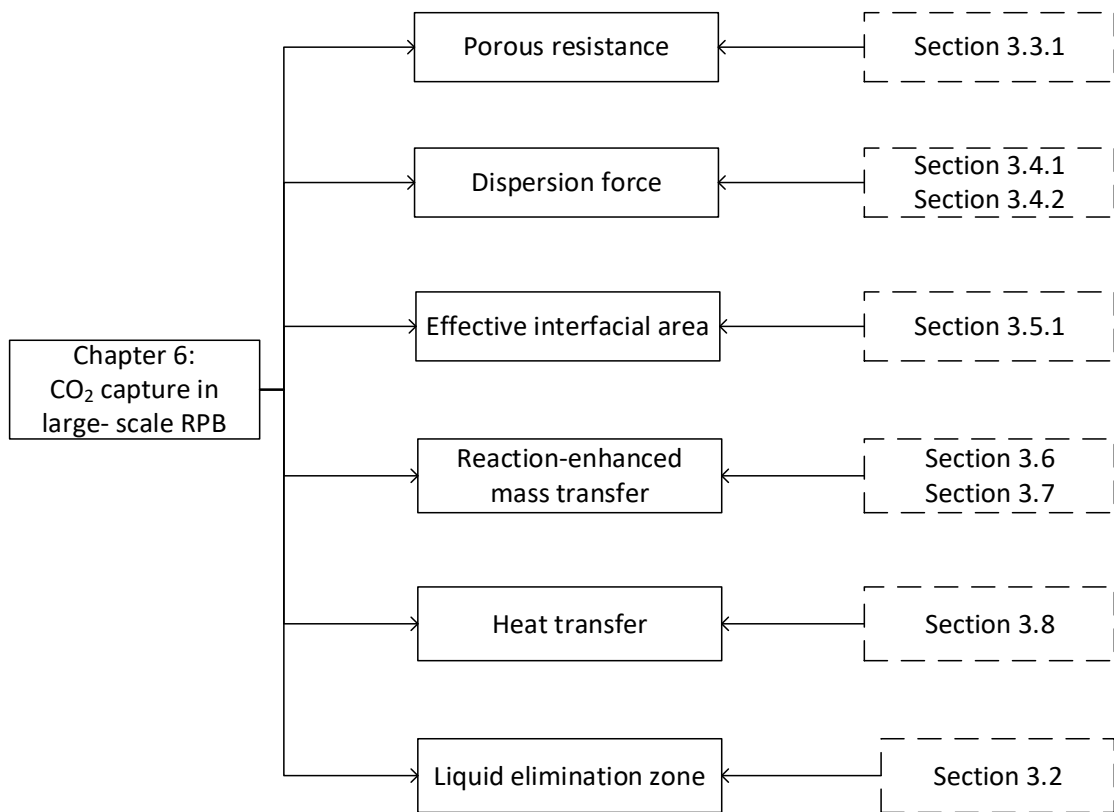


Figure 3-5 The sub-models employed in Chapter 6.

CHAPTER 4 : LIQUID DISPERSION IN A 3D RPB MODEL USING AN EULERIAN POROUS MEDIUM APPROACH

Summary

In this chapter, a 3D Eulerian porous medium model has been utilized coupled with the appropriate interfacial, drag and dispersion forces formulations for investigating the effect of the liquid dispersion in a practical RPB. The simulation results show that the effect of the capillary pressure and mechanical dispersion forces on the liquid flow distribution and holdup in the RPB is clear and important. In addition, the effects of the dispersion force on the liquid holdup under different design and operational parameters have been thoroughly analyzed. The investigation demonstrates that utilizing the Eulerian method can substantially reduce the simulation time and efforts when compared to the pore resolved method, such as the Volume of Fluid method. This provides an accurate and feasible approach to simulate RPBs in full 3D and for RPB technology scaling up and optimizations.

4.1 Introduction

Liquid dispersion plays an important role in determining the liquid flow behaviour in the RPB and it is the predominant reason for the enhancement of the mass transfer in RPBs [18]. Liquid dispersion in the RPBs has been explored previously both

experimentally and computationally using the VOF method [14, 17, 18, 32, 38-40, 77]. However, these studies were only at the stage of observing the phenomenon and the process of the dispersion in RPBs, and no one has evaluated and quantified the dispersion in a RPB. In addition, the VOF method is not suitable for simulations of pilot-scale 2D and 3D RPBs due to the limitations in computer resources, while the Eulerian method using a porous media model is a promising alternative method.

In this chapter, a 3D RPB model was employed based on a practical RPB from the published literature. The packing zone was regarded as a porous media and the Eulerian porous medium method coupled with the interfacial, drag and dispersion force models were employed to study the liquid dispersion in the packing region of the RPB. The sub-models employed in this chapter have been illustrated in a flowchart in Section 3.9. The results have been compared with the available experimental data. The sensitivity of the sub-models and the effect of some important parameters, including the rotational speed, bed porosity, liquid flow rate, liquid nozzle size and number of nozzles have been thoroughly analyzed and discussed. The results show that using the model developed can accurately and effectively reflect the distribution of the liquid holdup in the packing region and the effect of the dispersion force on the liquid holdup under different simulation conditions. Thus, the proposed method has paved the way for the model to be used, with confidence, in the next chapter for simulating the gas-liquid flow and mass transfer in a 3D entire RPB cost effectively and accurately.

4.2 CFD modelling

4.2.1 Geometry of the RPB

In order to develop and validate the CFD model, quality experiment data should be obtained. Among the available experimental studies in the literature on RPBs [20, 60, 64, 173], Yang's experiment [64] has been selected and it is for the following reasons: (i) the relative detailed dimensions of the RPB have been provided, especially the size of the liquid distribution nozzle; (ii) the packing material used in Yang's experiment matches those employed in the development of the drag force model used in this paper so that the accuracy of the model can be ensured; (iii) the liquid holdup with different operational conditions and the distribution of liquid holdup along the radial position are presented in Yang's paper, which could be used to verify the simulation results; and (iv) the experimental data has previously been used by Ouyang et al. [26], Lu et al. [34], Xie et al.[31] and Liu et al. [20] in order to validate their models, thus indicating that the data is reliable.

The 3D geometry of the experimental rig has been reproduced in Figure 3-1. Because the outer cavity zone between the case and the rotating bed has almost no influence on the liquid holdup within the packing region [28, 29], and the objective of this chapter is to study the hydrodynamics in the packing region, then only the rotating bed itself and the location of the liquid nozzle are shown in the figure. The inner diameter, outer diameter and axial length (thickness) of the packing are 42, 82 and 20 mm, respectively. The packing is a wire mesh with a void fraction and a specific area of 0.95 and 497 m^2/m^3 , respectively. The rotational speed of the bed employed in the experiments varied between 500-2500 rpm, and the liquid flow rate ranged from 22.9 - 43 cm^3/s . The liquid

distributing nozzle is rectangular in shape, and its size is 1×15 mm.

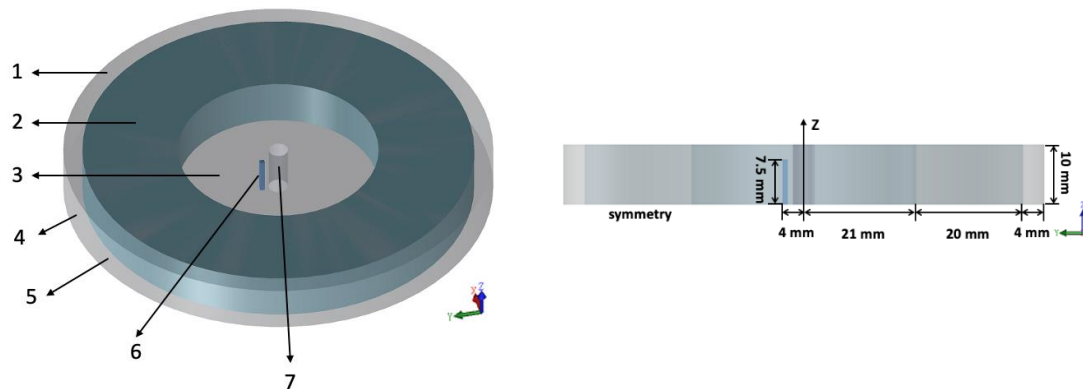


Figure 4-1 Schematic diagram of the 3D RPB and corresponding size (1, outer cavity zone; 2, packing zone; 3, inner cavity zone; 4, pressure outlet; 5, symmetry; 6, liquid inlet; 7, pressure outlet, Z - axis is the axis of rotation).

In the CFD model, due to the symmetry of the packing bed, only half of the bed has been investigated, and the thickness of the packing is 10 mm, as shown in Figure 4-1. In addition, for the purpose of numerical stability, an 8mm extension to the exit of the rotational bed was used. Therefore, the diameter of the model is 90 mm in total.

4.2.2 Assumptions for the model

The main assumptions made for the RPB model are as follows:

- (i) The packing is a homogenous porous medium.
- (ii) The flow is incompressible.
- (iii) The pressure field is shared by the gas and liquid phases.
- (iv) The liquid flow in the packed bed is dominated by the form of the film, and the dispersed droplets.

4.2.3 Solution procedure

The 3D RPB simulations have been performed using the ANSYS Fluent (version 2019R3). The transient based solver is employed in order to solve the governing fluid flow equations discussed in the previous sections, and the UDF has been developed for implementing the extra forces in the momentum equations. The air and water have been selected as the gas and liquid materials, respectively.

It is generally believed that the realizable k - ϵ model is more suitable for RPB than the standard k - ϵ model due to two reasons. Firstly, the realizable k - ϵ model contains a new formulation for the turbulence viscosity: C_μ is not a constant as in the standard model but a variable, and it is a function of the mean strain and rotation rates [174]. The second reason is a new transport equation for the dissipation rate in the realizable k - ϵ model, ϵ , is employed and this is derived from an exact equation for the transport of the mean-square vorticity fluctuation [175]. As a result, the realizable k - ϵ model gives improved predictions for the spreading rate of the jets, a superior ability to capture the mean flow of complex structures and for flows involving rotation, boundary layers under strong adverse pressure gradients, separation and recirculation [119]. In addition, it has been frequently used for the fluid flow simulations in RPBs [21, 90, 176, 177]. Therefore, the realizable k - ϵ turbulence model has been chosen in this thesis.

The pressure-based method and the absolute velocity formulation have been utilized. The time step was set as 3×10^{-4} s, and the maximum iteration number was less than 20 at each time step and the convergence tolerance was 1×10^{-4} . When the simulation achieved the pseudo steady state, the difference of the mass flow rate between the liquid inlet and outlet was less than 0.1%, and the residuals of the mass balance equations and

the other equations were less than 5×10^{-4} and 1×10^{-4} , respectively.

4.2.4 Boundary conditions

The liquid phase is water, and its viscosity is $0.001 \text{ kg}/(\text{m} \cdot \text{s})$. The gas phase is air. It can be seen from Figure 4-1 that the inlet (boundary 6) has been set as a velocity inlet boundary and the liquid velocity ranges from 1.53 to 2.87 m/s according to the experimental settings [64]. In addition, there is no forced gas flows through the packed bed in the experiment [64]. Therefore, the gas velocity is set as 0. Accordingly, the inner and outer surfaces of the RPB (boundary 7 and 4) are set as pressure outlets with a zero gauge pressure. The rotational speeds varies from 500 to 2500 rpm. Since the gravity is relatively small when compared with the high centrifugal force (5.8-286 times that of gravity), the gravity can be neglected in the RPB [25]. As a result, the flow is almost symmetric across the bed from the top to the bottom. Therefore, only half of the bed has been modelled with a symmetric boundary being applied on the central plane perpendicular to the rotating axis in order to minimize the computational time. The porosity of the packing is set as 0.95. The sliding model has been employed to realize the motion of the packing. The wall boundaries have been set as no slip walls.

Table 4-1 The operational conditions employed in the experiments [64].

Liquid flow rate (cm^3/s)	Liquid viscosity ($\text{kg}/(\text{m} \cdot \text{s})$)	Rotational speed (rpm)	Packing porosity	Nozzle size ($\text{mm} \times \text{mm}$)	Number of nozzles
23-43	0.001	500-1500	0.95	15×1	1

4.2.5 Mesh independence

The ANSYS Mesh was employed to generate the grid of the 3D RPB model, see Figure

4-2 for a typical mesh layout. The hexahedral mesh elements formed the 3D computational grid. The average skewness and element quality are 0.09 and 0.91, respectively. The liquid holdup in the packing was tested with many different numbers of cells and meshes in order to obtain a mesh independent solution. It was found the liquid holdup in the packing remained stable until the cell number reached 51,000. As a result, 51,000 cells were employed in order to accurately calculate the flow field.

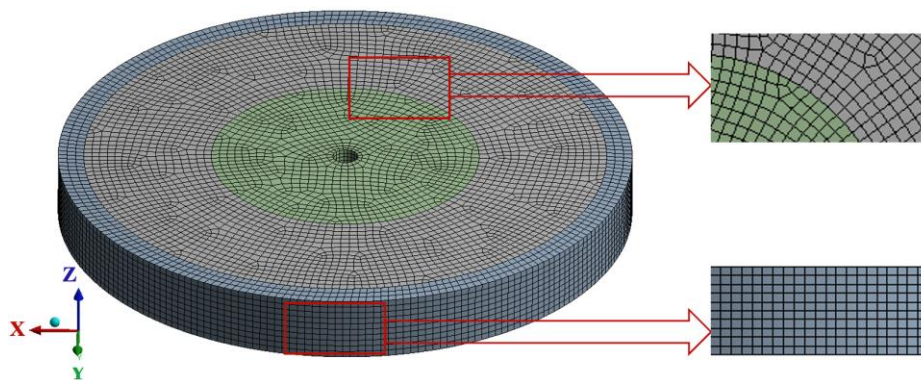


Figure 4-2 Schematic of the mesh in the 3D model.

4.3 Results and discussion

In this section, the model validations have been presented with one of the experimental cases under the rotational speed and liquid flow rate being 1500 rpm and $43 \text{ cm}^3/\text{s}$, respectively. And a total of 96 cases have simulated where the sensitivity of the formula employed for the modelling of the dispersion force and the effect of various design and operational parameters of the RPB on the fluid flows and liquid holdups have been investigated.

4.3.1 Validation and the liquid holdup along the radial direction

In order to validate the CFD model developed, the liquid holdup has been chosen as the

validation parameter because of the following reasons: (i) the liquid holdup is one of the most important parameters in the packed bed design, as it is relevant to the hydraulic and mass transfer property of the bed. It is a result of the balance of various forces including the dispersion force acting on the liquid; (ii) the liquid holdup could indirectly reflect other factors, such as the liquid velocity. For the RPBs, the higher the radial velocity, the lower is the liquid holdup. If the liquid holdup obtained by the simulation matches well with the experimental data, then this indicates that the liquid velocity has a good agreement with the experimental data; (iii) although many parameters, including the liquid holdup, liquid velocity, etc., could be obtained by the simulation, the liquid holdup is much easier to be obtained for most experimental investigations. Therefore, many studies on the flow dynamics in the RPBs have selected the liquid holdup as the validation parameter [16, 20, 26, 28, 31, 34, 38]. The distributions of the liquid holdup, and the fractional effective interfacial area in the RPB have been obtained under the conditions of 1500 rpm rotational speed and 43 cm³/s liquid flow rate, as listed in Figure 4-3. The results obtained are compared with the experimental data obtained from [64].

Figure 4-3(a) shows the experiment observations obtained using X-ray technology, which shows the image of the liquid across the thickness of the bed. Figure 4-3(b) shows the predicted distribution of the liquid holdup on the central plane (plane of symmetry) obtained from the CFD simulation. A liquid stream with a high liquid fraction is presented in Figure 4-3(a) and 4-3(b) at the entrance to the bed due to the significant resistance of the packing. In addition, the liquid begins to flow in the tangential direction followed by the rotational bed and its radial velocity becomes smaller. In the meantime, the liquid spreads and disperses along its flow path, resulting

in a decreasing local liquid fraction and a more uniform liquid distribution as shown in both figures. The liquid volume fraction continues to decrease until the liquid flows out the outer packing region. From the above analysis, it is known that the liquid flow process and the liquid holdup distribution within the RPBs are similar in the simulation results and experimental data. The quantitative comparisons will be given in Figure 4-4(b).

Figure 4-3(c) shows the predicted fractional effective interfacial area on the symmetric plane. Because the effective interfacial area is the interfacial area in contact with the gas and liquid per unit volume of the packing, it can be found that the fractional effective interfacial area is larger where the liquid holdup is higher by comparing with Figures 4-3(b) and 4-3(c).

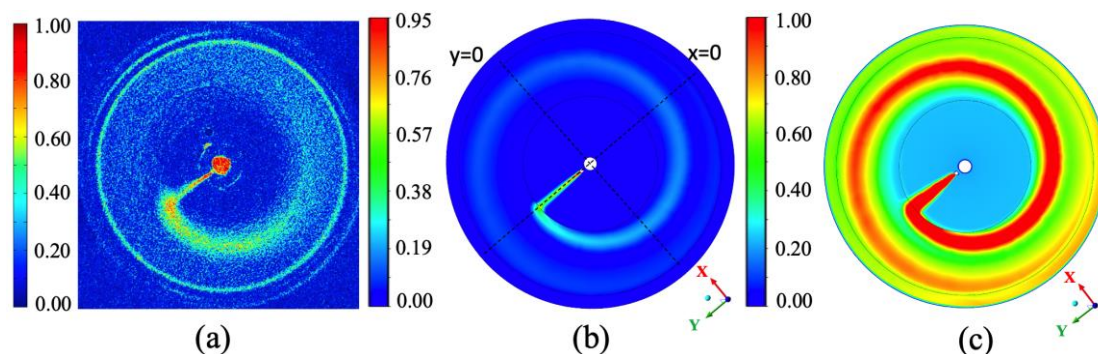


Figure 4-3 (a) Map of liquid holdup from the experiment [64]; contours of (b) liquid holdup from the simulation; and (c) fractional effective interfacial area from the simulation.

Figure 4-4 show the comparison of the liquid holdup between the simulation and the experimental data [64] in terms of (a) the liquid holdup along the radial position and (b) the total liquid holdup as a function of the rotational speed of the bed, together with the

velocity distribution along the radial direction. From Figure 4-4(a), it can be seen that the liquid holdup increases in the inner packing region (end-effect zone) since more and more liquid is dispersed and captured and the liquid radial velocity decreases quickly as is shown on the left of Figure 4-4(c) and this results from the large resistance from the packing. After that, the liquid radial velocity decreases gradually due to the resistance force with the wire mesh packing, and the liquid tangential velocity is close to and almost overlaps with the tangential velocity of the packing because the liquid quickly and largely follows the rotating packing after the liquid enters the packing. In the meantime, the fraction of the liquid volume (liquid holdup) should become smaller with the increase in the flow space in the bulk and outer packing region, thus resulting in a gradually decreasing liquid holdup along the radial direction. This phenomenon has been accurately predicted by the simulation results and also in the experimental data except in the outer packing region where an increase in the holdups is observed in the experiments. As explained by the authors of the experiments [64], the possible reasons of this observed increase are that the outer packing region has a slightly lower porosity relative to the bulk packing and the liquid droplets bounce back to the outer packing region after hitting the casing wall. These two reasons lead to the observed increase in the liquid holdup in the outer packing region. In addition, these reasons could also explain the high liquid holdup in a thin ring observed experimentally at the outer packing in Figure 4-3(a).

Figure 4-4(b) shows the comparison of the liquid holdup in the packing region under different rotational speeds between the simulation results and experimental data. It can be seen that the two curves decrease with the increasing rotational speed due to the

gradually stronger centrifugal force and the two curves are very close to each other. From Figure 4-4(b), the maximum deviation is observed at the lowest tested rotational speed (500 rpm) and the largest liquid flow rate ($43 \text{ cm}^3/\text{s}$). However, for the rest of the test conditions, the deviation is much lower, which could even be as low as 2%. It can be seen from Figure 4-4(a) that the liquid holdup increases in the outer packing region in the experiment, which may be the main reason for the deviation. As explained in the last paragraph, the slightly lower porosity and the liquid droplets that bounce back into the outer packing region lead to the observed increase in the liquid holdup in the experiment [64] and the deviation increases when the rotational speed decreases or the liquid flow rate increases. This could explain why the maximum deviation is observed at the lowest tested rotational speed (500 rpm) and the largest liquid flow rate ($43 \text{ cm}^3/\text{s}$). In addition to the outer spacing region, the difference in the liquid holdup in the inner and bulk packing regions is relatively small. Although only one experimental work has been used to validate the work presented in this chapter, the simulation results were very thoroughly and carefully compared with this set of experimental data. From Figures 4-3(a) and 4-3(b) as well as Figures 4-4(a) and 4-4(b), not only the distribution of the liquid holdup has been visually compared, but also the liquid holdup has been compared along the radial positions and under several different rotational speeds. Therefore, the model developed in this chapter could be used with much confidence to investigate the flow dynamics in the RPBs.

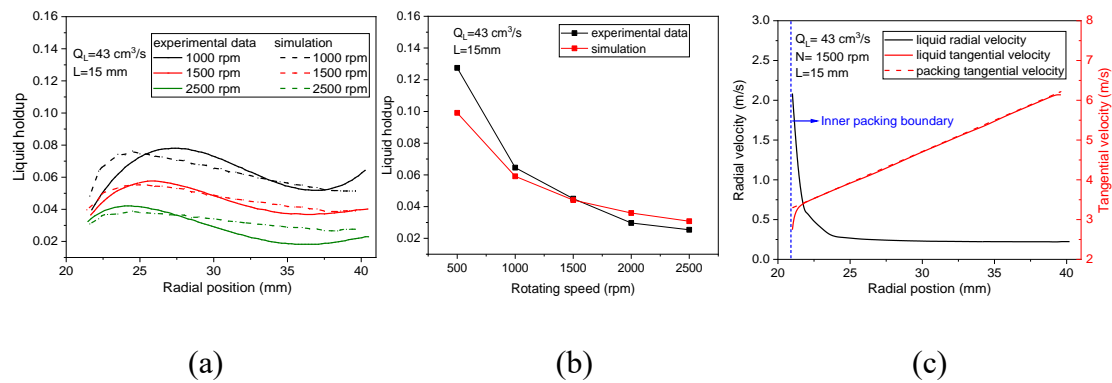


Figure 4-4 Comparison of the experimental data [64] and the simulation results for the liquid holdup (a) along the radial direction; (b) under different rotational speeds; and (c) velocity components along the radial direction.

Figure 4-5 shows the liquid distribution across the thickness of the bed on two different vertical planes (a, $x=0$ and b, $y=0$, see Figure 4-3(b)). It clearly can be seen from Figure 4-5(a) that after the jet flows from the liquid nozzle, the local liquid holdup becomes smaller in the inner cavity zone. When the liquid enters the inner packing, the local liquid holdup increases in the vicinity of the boundary of the inner cavity zone and the packing, and this increase has been shown and explained in Figures 4-3(a) and 4-3(b). After the liquid enters the packing, the liquid achieves its tangential velocity, thus, the liquid “appears and disappears” on these vertical planes as shown in Figures 4-5(a) and 4-5(b). Meantime, the liquid starts to disperse and spread, and as a result, the liquid distribution is relatively uniform in the axial direction in the outer packing region.

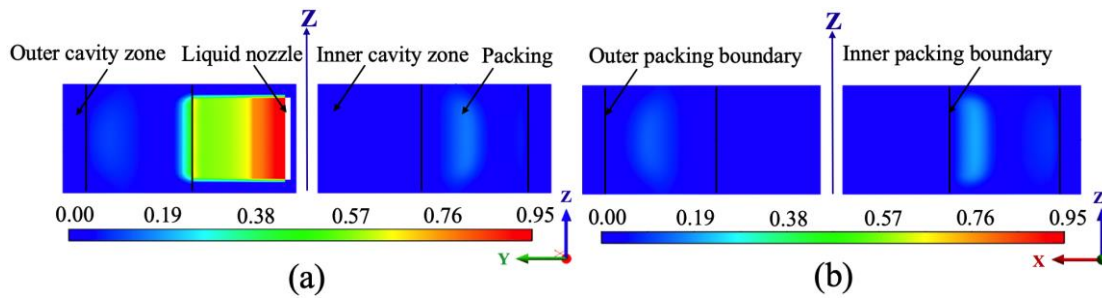


Figure 4-5 Contours of the liquid holdup on the planes (a) $x = 0$ and (b) $y = 0$.

4.3.2 Sensitivity of the simulation results to the dispersion force model

As mentioned in Section 4.1.4, the dispersion forces consist of the capillary pressure force and the mechanical dispersion force. Therefore, different capillary pressure models and the spread factor, S_f in the mechanical dispersion model can influence the magnitude of the modelled dispersion force and subsequently the distribution of the liquid holdup.

In order to demonstrate the degree of the liquid dispersion in all three flow directions, in particular the effect of the nozzle length. Two nozzle lengths, i.e. 15 and 7.5 mm (in the z -direction) have been employed.

4.3.2.1 Capillary pressure model

The Grosser and the Attou and Ferschneider models, which have been introduced in Section 4.4.1.1 were, respectively, employed as a source term ($\vec{F}_{C,L} = \varepsilon_L(1 - f_e)\nabla P_C$) in the momentum equation and their effect on the predicted liquid holdup were compared with those obtained without including the dispersion force term. In general, the liquid will disperse from the region of a higher liquid volume fraction to the region of a lower liquid volume fraction. During this process, the liquid spreads and disperses

into smaller droplets or forms thinner films under the effect of the dispersion force. This subsequently leads to more contact between the liquid and the packing and this increases the drag force from the packing (see Equation (3-14)). Therefore, more liquid is stacked in the packing region and the liquid holdup increases.

Figure 4-6 shows the effect of two different capillary pressure models on the liquid holdup distribution in the packing region for the two nozzle lengths investigated. It can be observed in Figure 4-6 that the Grosser capillary pressure model (Equation (3-29)) has little effect on the liquid holdup for both nozzle lengths. The possible reason is that in this model the capillary pressure force is inversely proportional to the packing porosity and the particle diameter only. Although the diameter of the wire mesh is small, the packing porosity is large, and it is close to 1. In addition, it has been reported that this model has the drawback that may fail to reproduce the steep rise in the capillary pressure as the liquid saturation approaches zero [152]. The above reasons may cause the Grosser capillary model to fail to catch the effect of the capillary pressure force in this RPB model. However, an increase in the liquid holdup is shown in Figure 4-6 after employing the Attou model. This is because that the Attou model is not only related to the packing porosity and diameter of the wire mesh, but also it is a function of the minimum equivalent diameter (d_{min}) and the fluid density ratio. In addition, it can be seen from Figure 4-6 that when the nozzle length is 15 mm, the liquid holdup starts to increase in the inner packing region and this is because the liquid has enough contact area with the packing to disperse due to the relatively uniform liquid distribution at the axial direction (z - direction). However, when the nozzle length is 7.5 mm, which means the liquid concentrates in the central part of the inner packing, the liquid dispersion

cannot increase quickly until it flows into the bulk of the packing where the liquid has occupied enough space to disperse.

From the above analysis, it can be assumed that the Attou model can be used to accurately describe the capillary pressure force on the liquid holdup. In addition, this model can overcome the shortage of the Grosser model and it has been widely validated and used in many works for CPBs [149, 152, 178]. Therefore, the Attou model has been utilized in the following work.

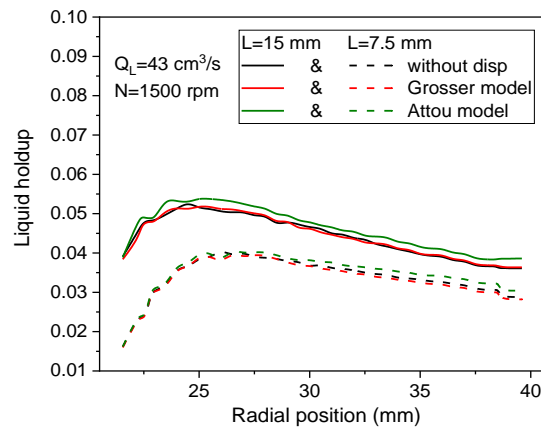


Figure 4-6 The effect of the capillary pressure models on the liquid holdup.

4.3.2.2 Spread factor in the dispersion force model

The spread factor, S_f , which is the only estimated parameter for the mechanical dispersion model, determines the magnitude of the drift velocity and thus influences the dispersion of the liquid. By conducting the tracer experiments of the CPBs, Hoek et al. [179] investigated the effect of the packing particle size on the spread factor and proposed a correlation for the spread factor ($S_f = 0.12d_w$). In addition, the packing particle shape was considered, and the correlation ($S_f = 0.015d_w^{0.5}\phi^{-0.33}$) was suggested by Baldi and Specchia [180]. However, this does not take into account the

liquid surface tension, thus, another correlation ($S_f = 0.231d_w^{0.5}\sigma$) was introduced [181], which is dependent of the particle size and surface tension.

Similar to the capillary pressure force, the mechanical dispersion force is also considered as a source term in the momentum equation. The effect of the different correlations discussed above for the spread factor on the liquid holdup along the radial direction of the RPB has been investigated as shown in Figure 4-7 where only the mechanical dispersion forces have been considered, without including the capillary pressure force. When the nozzle length is 15 mm, the effect of the mechanical dispersion force on the liquid holdup is relatively small. The reason is that the liquid holdup in the packing region is relatively small in three flow directions due to the large nozzle length. This leads to a small spatial gradient of the liquid holdup and a small driving force to cause the liquid to flow from the high liquid fraction region to the low liquid fraction region and subsequently result in a small increase in the liquid holdup due to dispersion. It also can be observed that the red curve increases slightly with respect to the black curve because of the very small spread factor, which is 4.8×10^{-5} . For the nozzle length being 7.5 mm, the blue and olive curves, whose spread factors respectively are 3.0×10^{-4} and 3.3×10^{-4} , are clearly higher than the red curve. Therefore, it can be concluded that the spread factor is a very sensitive quantity for flows with a less uniform and more concentrated distribution, such as those for the case of the nozzle length being 7.5 mm.

It was reported that the correlations of Baldi and Specchia [180] and Onda et al. [180] were more consistent with the experimental data of CPBs [152]. In addition, the distributions of the liquid holdup in the packing region of the RPB are similar when

employing the above two mechanical dispersion models as shown in Figure 4-7, which means that both models can be theoretically utilized in the RPB. Nevertheless, Baldi and Specchia [152] studied the influence of the shape of the packing elements by using beads, Berl saddles and Raschig rings, but not the wire mesh used in this thesis. In addition, the surface tension can affect the liquid dispersion [182], and this factor is considered when the spread factor is estimated using $0.231d_w^{0.5}\sigma$, thus this correlation has been selected in the work presented in the remainder of this thesis.

So far, the suitable capillary pressure and mechanical dispersion models have been assessed. The significance of the capillary pressure force and mechanical dispersion force to the predicted liquid holdup can be assessed by comparing Figures 4-6 and 4-7. It is noted that the influences of the capillary pressure force and mechanical dispersion force on the liquid hold up are in a similar order of magnitude for the case when the nozzle length is 15 mm. When for the nozzle length is 7.5 mm, the predicted liquid dispersion in this RPB is dominated by the mechanical dispersion and the capillary effect is small.

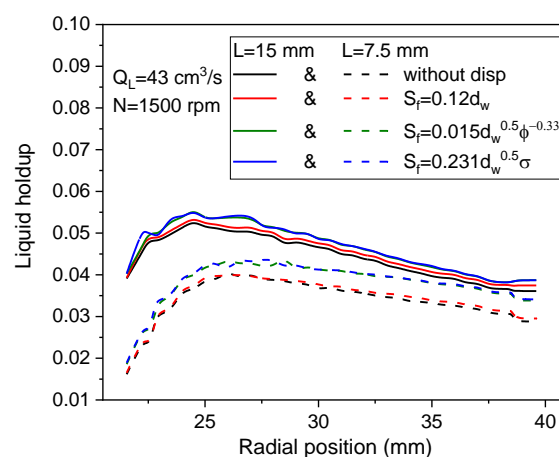


Figure 4-7 The effect of the correlations for the spread factor on the liquid holdup.

4.3.3 Effect of the operational and design parameters on the dispersion force

The effect of the operational parameters on the dispersion force has been investigated in the RPB models with the two liquid nozzle lengths of 15 and 7.5 mm. In addition, the effect of the dispersion forces on the liquid holdup with different operational parameters are similar for both the investigated liquid nozzle lengths. Therefore, in this section only the 7.5 mm nozzle length has been chosen to show the effect of the operational parameters on the dispersion force. In addition, in order to highlight the characteristics of the model when employing dispersion forces, the effect of the dispersion force on the liquid holdup have been analyzed by comparing the results of the liquid holdup predicted from the models with and without employing the dispersion forces.

4.3.3.1 The effect of liquid flow rate

Figure 4-8 illustrates the effect of the liquid flow rate on the liquid holdup in the packing region when the rotating speeds are 500 and 1000 rpm and the liquid flow rate varies from 23 to 43 cm³/s. On taking the rotating speeds of 500 rpm as an example, Figures 4-9 and 4-10 show the predicted contour plots of the liquid holdup and the fractional effective interfacial area on the central/symmetric plane ($z=0.01$ m) without and with considering the dispersion forces. It can be observed, when the liquid flow rate increases, more liquid exists in the packing region as shown in Figures 4-10(a) and 4-10(b), thus, the liquid volume fraction (holdup) becomes higher in the packing as can be seen in Figures 4-8(a) and 4-8(b). It also indicates that more of the packing surface

is covered by the liquid phase. As a result, the effective interfacial area increases, and this is shown in Figures 4-10(c) and 4-10(d).

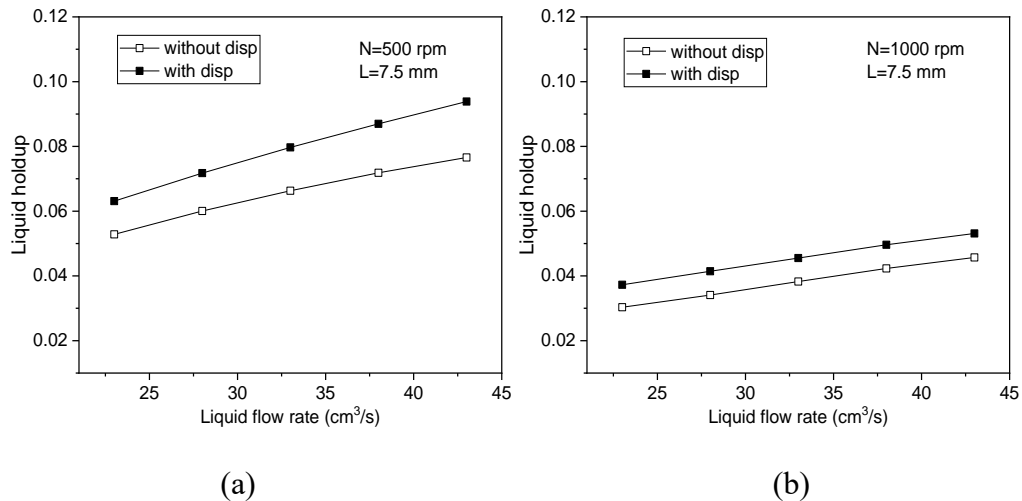


Figure 4-8 The effect of the liquid flow rate on the liquid holdup under different rotational speeds: (a) 500 rpm and (b) 1000 rpm.

Compared with Figures 4-9(a) and 4-10(a) or Figures 4-9(b) and 4-10(b), it is clear that the liquid distributes more uniformly under the influence of the liquid dispersion force. It further leads to a higher effective interfacial area, which is shown by comparing Figures 4-9(c) and 4-10(c) as well as Figures 4-9(d) and 4-10(d). Although it appears that the red area occupied in Figures 4-9(c) and 4-9(d) are larger than that in Figures 4-10(c) and 4-10(d), the fact is that the overall fractional effective interfacial area in Figures 4-10(c) and 4-10(d) increases. This is because the liquid is distributed more uniformly and more liquid covers the packing surface and is in contact with the gas phase due to the dispersion effect. Also, it can be seen from Figure 4-8(a) that the effect of the dispersion forces on the liquid holdup becomes larger with the increase in the liquid flow rate and this is due to the higher spatial gradient in the liquid holdup.

However, the increase in the liquid holdup in Figure 4-8(b) is smaller when compared with that in Figure 4-8(a). The reason is that the liquid spreads into more tiny droplets due to the stronger interaction with packing when employing a higher rotational speed. As a result, the dispersed liquid droplets achieve a larger radial velocity and they are difficult to retain in the packing region.

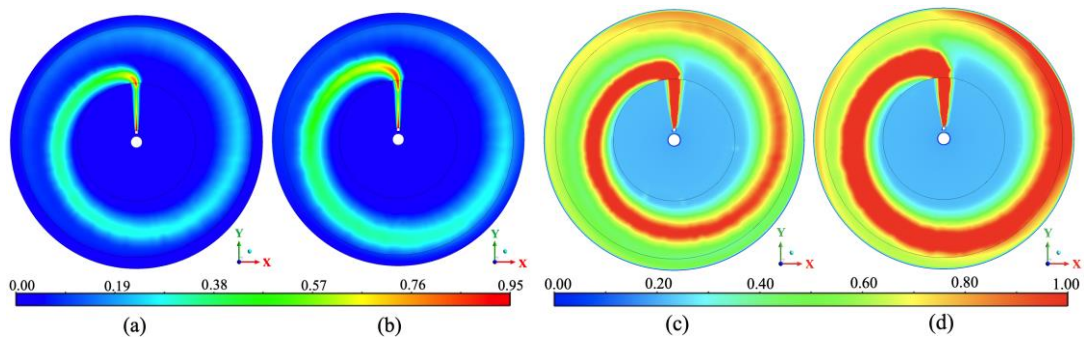


Figure 4-9 The holdup up and fractional effective interfacial area on the symmetric plane before employing the dispersion force with different liquid flow rates: (a) ε_L , 23 cm^3/s ; (b) ε_L , 43 cm^3/s ; (c) f_e , 23 cm^3/s ; and (d) f_e , 43 cm^3/s .

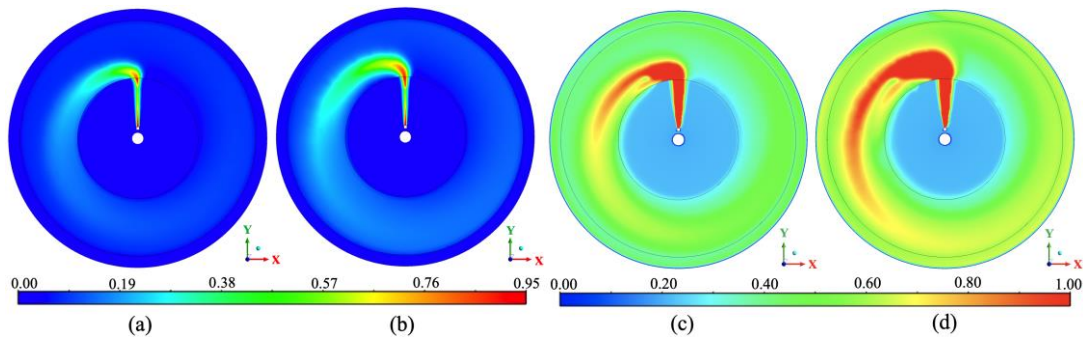


Figure 4-10 The holdup up and fractional effective interfacial area on the symmetric plane after employing the dispersion force with different liquid flow rates: (a) ε_L , 23 cm^3/s ; (b) ε_L , 43 cm^3/s ; (c) f_e , 23 cm^3/s ; and (d) f_e , 43 cm^3/s .

4.3.3.2 Effect of the rotational speed and packing porosity

It has been proven that the rotational speed can influence the liquid flow dynamics and liquid dispersion in the packing region [20, 28, 137]. Thus, the effect of the rotational speed on the liquid holdup is shown in Figure 4-11(a) when the liquid flow rate is $43 \text{ cm}^3/\text{s}$. When the rotational speed increases from 500 to 2500 rpm, the liquid can receive more kinetic energy from the rotating packing, and the liquid is formed into more tiny droplets and fragments, which can improve the liquid distribution and the effective interfacial area [28]. Although the higher effective interfacial area can increase the liquid-solid drag force, the higher liquid radial velocity resulting from the stronger centrifugal force is predominant, thus leading to the liquid holdup reducing as shown in Figure 4-11(a). In addition, the lower liquid holdup and more uniform liquid distribution are caused by the higher rotational speed and this leads to a smaller spatial gradient of the liquid holdup, which causes the smaller liquid dispersion forces. Therefore, the increase in the magnitude of the liquid holdup reduces with the rotational speed increasing.

The packing porosity is an important characteristic for the RPBs and this factor may also affect the liquid holdup and liquid dispersion performance. Figure 4-11(b) shows the liquid holdup with different porosity under the liquid flow rate of $23 \text{ cm}^3/\text{s}$. From Figure 4-11(b), it can be observed that the liquid holdup decreases with the decreasing in the packing porosity. Reducing the packing porosity means that more wire mesh is stacked and occupied in the packing region, thus the fraction of the liquid volume (liquid holdup) would be smaller according to Equation (3-2).

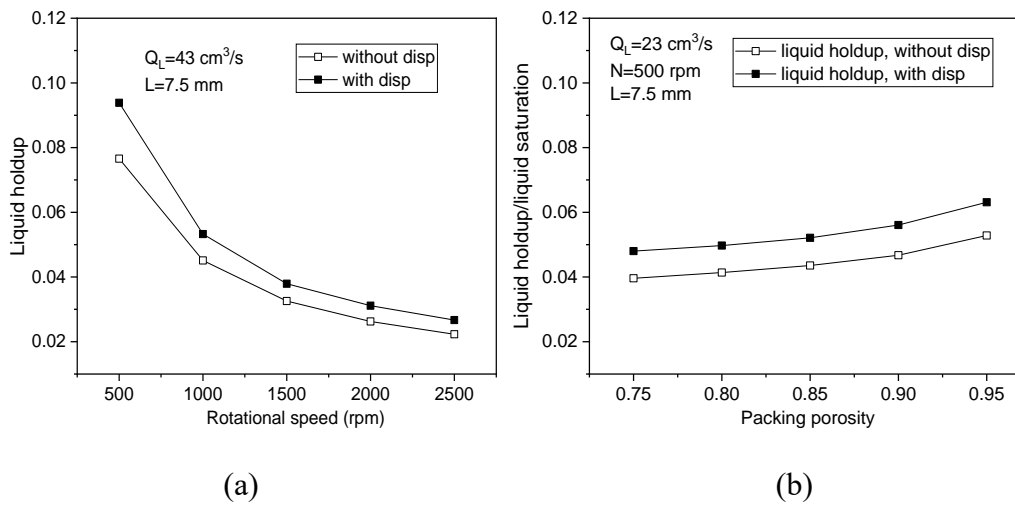


Figure 4-11 The effect of the (a) rotational speed; and (b) packing porosity on the liquid holdup.

4.3.3.3 Effect of the nozzle size and number of nozzles

The nozzle size and the number of nozzles are very important for the initial liquid distribution and dispersion [38]. Thus, Figures 4-12(a), 4-12(b) and 4-12(c) show the effect of the nozzle (axial) length, nozzle width, and number of nozzle(s) on the liquid holdup under the same liquid flow rate and rotational speed of $43 \text{ cm}^3/\text{s}$ and 500 rpm , respectively. In particular, the effect of the nozzle length on the liquid holdup has been rarely studied due to the limitation of the 2D model [38]. However, it can be studied by using the 3D model and its effect on the dispersion force has been investigated.

From Figure 4-12(a), with the increase in the nozzle length, the liquid jet velocity reduces and the liquid holdup distributes more uniformly in the packing region, especially in the axial direction [183]. As a result, the liquid holdup in the packing region increases. In addition, as the nozzle length increases, the effect of the liquid dispersion force on the liquid holdup becomes weaker and this is due to two reasons.

The first reason is the small spatial gradient in the liquid holdup in the packing region that results from the more uniform liquid distribution. The second is that the smaller liquid jet velocity leads to a smaller drift velocity, and the drift velocity is proportional to the mechanical dispersion force. However, the second reason is not the main reason, and this is because the liquid jet velocity would substantially reduce after entering the packing so that it is only significant within a small entrance region although the initial impact on the packing, and thus the dispersion, is still important.

From Figure 4-12(b), the liquid holdup increases slightly with the increase in the nozzle width. The reason is that increasing the nozzle width not only reduces the liquid jet velocity, but also increases the liquid jet area in the horizontal direction, which could increase the liquid holdup. However, the flow in the packing is influenced more by the centrifugal force than the initial liquid jet velocity and jet area. Therefore, the increase of the liquid holdup is very limited. In addition, the slight increase in the liquid holdup results in almost no change in the spatial gradient of the liquid holdup. Therefore, the nozzle width has little effect on the liquid dispersion performance. In addition, it is noted that this conclusion is in contrast to that reported in the work of Zhang et al. [38], where the liquid holdup increases significantly when the width of the nozzle increases. The possible reason is that Zhang et al. [38] used a stationary packing and there is no centrifugal force generated when the liquid passes through the stationary wire mesh.

It can be seen, from Figure 4-12(c), that the liquid holdup increases when the number of nozzles increases. When the number of nozzles increases from one to two and four, the increases in the liquid holdup are 5.3% and 8.0%, respectively. This indicates that the number of the nozzles has a larger influence on the liquid holdup when the number

of nozzles is small. Taking the symmetrical cross-sectional plane as an example, Figure 4-13 shows the distribution of the liquid holdup on this surface. It can be seen that the increasing the number of nozzles could improve the liquid distribution in the radial and circumferential directions. The more uniform is the liquid distribution then this leads to a slightly lower spatial gradient of the liquid volume fraction. Therefore, the relative increase in the liquid holdup reduces slightly with the further increasing number of nozzles.

When compared with Figures 4-12(a) - 4-12(c), it is noted that the liquid holdup is relatively sensitive to the nozzle length and number of nozzles rather than the nozzle width. Therefore, employing a longer nozzle length can increase the liquid holdup, while increasing the number of nozzles could lead to a more uniform liquid distribution, which may be good for the mass transfer performance.

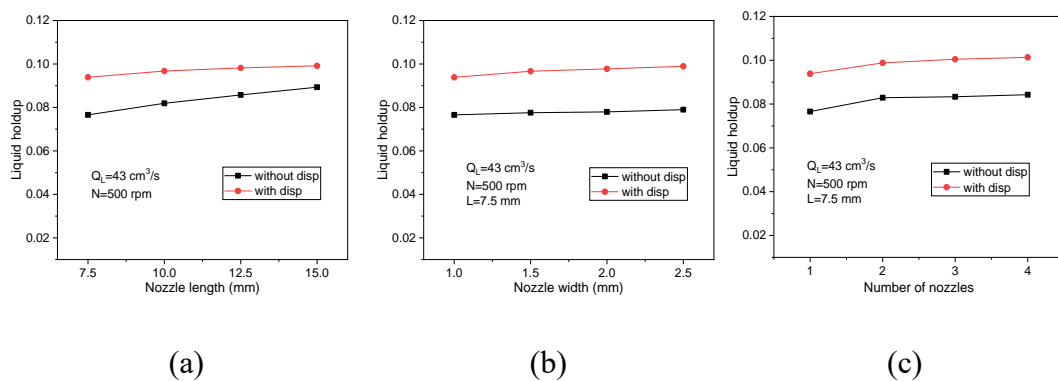


Figure 4-12 The effect of the (a) nozzle length; (b) nozzle width; and (c) number of nozzles, on the liquid holdup.

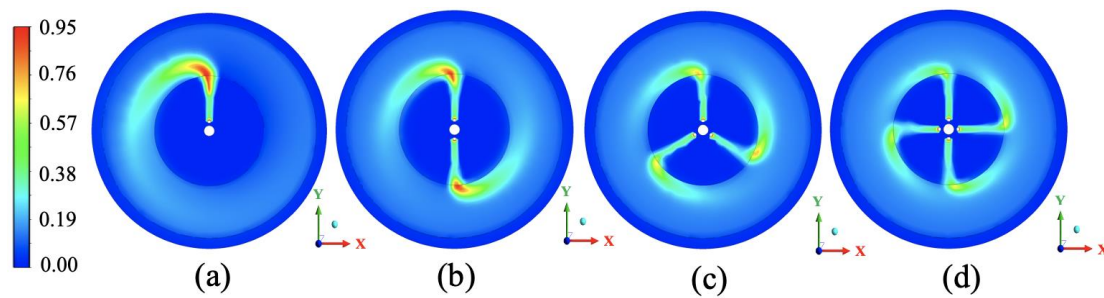


Figure 4-13 The distribution of the liquid holdup on the symmetric cross-sectional surface.

4.4 Comments on the time efficacy of the new Eulerian model

All the simulations presented in this chapter have been performed using a PC with an Intel Core i7-7700k CPU and 8 processors. In general, it takes only 0.5-3 h depending on the rotational speed simulated to finish a full analysis of the 3D RPB. It should be noted that, in a 2D RPB model that is established based on the same experimental rig, a 0.87 M grid is chosen to investigate the flow characteristics when using the VOF method [28] compared with only about a 0.05 M grid being required for the 3D simulation that has been performed in the present work. It is clear that a considerable amount of time and resource can be saved when using the Eulerian method.

4.5 Conclusions

The overall aim of this work is to develop an efficient and accurate modelling approach that can be practically used for the modelling of the physical and chemical processes occurring in a full scale rotational packed bed in the future. The specific objectives of this chapter are to investigate the liquid dispersion in the packing region, and how to accurately model the effects in a RPB. In this chapter, a novel 3D Eulerian porous

medium RPB model has been applied using the CFD software package FLUENT, coupled with the interfacial, drag and dispersion force models, as well as the effective interfacial area model. The influence of the dispersion forces on the liquid holdup was investigated and the sensitivity of the CFD predictions on the dispersion model employed, together with the influence of the design and operational parameters such as the rotational speed, liquid flow rate, etc. have been critically analyzed. Some of the main findings are as follows: (i) the porous medium model with the Eulerian method was successfully used to model the fluid dynamics and liquid dispersion in a 3D RPB. Using this model we can substantially reduce the computational time and efforts; (ii) the new form of the porous resistance model employed for two-phase flows (see Section 3.3.1) could accurately predict the porous resistance in the packing; (iii) the correlation for the gas-liquid effective interfacial area developed in Section 3.5.1 could fit the non-uniform flow and the distribution of the fractional effective interfacial area (f_e) is consistent with the reality. The effective interfacial area is larger where the liquid holdup is higher. In addition, the use of the developed f_e would make the porous medium model more accurate; and (iv) the dispersion force models, for the first time, were employed into the model to simulate the liquid dispersion in a complete packing region in 3D. In the 3D model coupled with the dispersion force models, the effect of liquid dispersion on the liquid holdup could be quantified and more accurate liquid flow performance was achieved.

The simulation results show that the effect of the capillary pressure and mechanical dispersion forces on the liquid holdup are important to consider but showed different levels of significance with different liquid nozzle lengths. The effect of the capillary

pressure force and mechanical dispersion force on the liquid holdup are similar when the nozzle length is 15 mm. While when the nozzle length is 7.5 mm, the liquid dispersion in this RPB model is dominated by the mechanical dispersion and the spread factor is a very sensitive quantity. With the liquid flow rate increasing, the influence of the dispersion force on the liquid holdup are different under different rotational speeds. The effect of the dispersion force on the liquid holdup is almost the same with different nozzle widths and packing porosity. In addition, increasing the number of the liquid nozzles from 1-4 could improve the liquid distribution and liquid holdup in the packing region substantially. However, further increasing the number of nozzles tends to be less effective. Overall, the method proposed and employed in this chapter paves the way for much more efficient simulations of full 3D RPBs in the next chapter.

CHAPTER 5 : CO₂ CAPTURE IN AN ENTIRE 3D RPB MODEL USING AN EULERIAN POROUS MEDIUM APPROACH

Summary

This chapter develops a new, feasible and effective approach to investigate the CO₂ capture processes in an entire RPB. A full 3D CFD model, including the packing and the inner and outer cavity zones, has been established by employing the Eulerian porous medium method. In addition, various sub-models, including the models of the effective interfacial area, drag force, interfacial force, heat transfer, mass transfer, etc., have been introduced for exploring the hydrodynamics, thermodynamics, and reaction-enhanced mass transfer processes in the packing and outer cavity zones. The CO₂ capture performance in the packing and outer cavity zones has been quantitatively analyzed under different operating conditions. The simulation results show good agreement with the experimental data, and the contribution of the outer cavity zone to the CO₂ capture of the RPB is in the range of 28%~42%. This work provides a new approach to efficiently and comprehensively simulate the mass transfer process in the RPB.

5.1 Introduction

The RPB has the potential to enhance the CO₂ capture performance and reduce the packed bed size by applying a high centrifugal force (100-1000 times gravity) [63]. The CO₂ capture processes in the RPB is complex since the flow dynamics, thermodynamics and mass transfer could affect each other. In addition, the flow characteristics and mass transfer in the rotating packing (with a large specific area) are quite different from those in the static outer cavity zone (with a large empty space). Although a few investigations have studied the CO₂ capture process in the RPB, they only focus on the packing region instead of the entire RPB, which also includes the outer cavity zone with a large volume. In the experimental investigations, it has been reported that the mass transfer area and mass transfer of the outer cavity zone could be up to 30% and 13-25% of the overall mass transfer area and total mass transfer in the entire RPB, respectively [42-45]. Therefore, the CO₂ absorption in the outer cavity zone is important to be investigated.

However, the flow characteristics in the packing and outer cavity zones are quite different, thus, the sub-models for the forces (Sections 3.3 and 3.4), the effective interfacial area (Section 3.5) and the liquid droplet diameter (Sections 3.5.2 and 3.8) should be separately employed. Also, the reaction-enhancement mass transfer and heat transfer models (Section 3.6-Section 3.8) were employed in order to examine the mass transfer and heat transfer processes within the RPB. The sub-models employed in this chapter have been illustrated in a flowchart in Section 3.9. On this basis, a comprehensive 3D RPB model, including the packing, inner and outer cavity zones, was built based on a practical pilot-scale RPB coupled with the above-mentioned sub-models. The overall volumetric mass transfer coefficient ($K_L a_e$) and liquid outlet

temperature under various operating conditions were analysed. Furthermore, the ratio of the CO₂ capture performance in the packing zone and outer cavity zone was quantitatively investigated.

5.2 CFD modelling

5.2.1 Geometry of the RPB

In order to establish and validate the 3D RPB model, the detailed information of the experimental rig and quality experimental results are required. Among all the published experimental works on RPBs, the Kolawole's experimental data [161] is suitable to be the comparison data and the RPB model is established based on the experimental rig mentioned in Kolawole's thesis. This RPB rig was a pilot-scale counter-current RPB. The CO₂ capture process was studied in this vertical-oriented RPB using the MEA solution. The RPB was operated under different conditions, including the rotational speed, liquid-gas (L/G) mass flow ratios and MEA concentration. In addition, the overall volumetric mass transfer coefficient, CO₂ capture efficiency, liquid outlet temperature, etc., were obtained. The important information of the operating conditions is shown in Table 5-1 [161].

Table 5-1 The operational conditions of the experiments [161].

MEA concentration (wt%)	Rotational speed (rpm)	L/G mass ratio
30	600	2.7
30	600	3.1
30	600	3.5
30	850	2.7
30	850	3.1
30	850	3.5
30	1150	2.7
30	1150	3.1
30	1150	3.5
50	600	1.8
50	600	2.1
50	600	2.4
50	850	1.8
50	850	2.1
50	850	2.4
50	1150	1.8
50	1150	2.1
50	1150	2.4
70	600	1.3
70	600	1.5
70	600	1.7
70	850	1.3
70	850	1.5
70	850	1.7
70	1150	1.3
70	1150	1.5
70	1150	1.7

Therefore, the advantages for selecting the Kolawole's experimental data are: (i) the relative detailed operating conditions and dimensions of the RPB have been offered, especially the size of the packing and outer cavity zones. (ii) The CO₂ capture performance with different operational conditions is analyzed by various indexes, including the overall mass transfer coefficient, the liquid and gas phase temperatures at the outlets, etc., which could help to validate the simulation results. And (iii) the experimental data has been presented in the published paper [184] and previously utilized by Lu et al. [6] for verifying their models, thus meaning that the experimental data is reliable. In the Kolawole experimental work, the CO₂ capture performance has been investigated under various rotational speeds, MEA concentration, etc., and the CO₂ capture rate and the outlet temperature have been achieved. However, no experimental data related to the flow characteristics (i.e. liquid holdup) has been shown in the thesis [161], thus, the flow dynamics obtained by the experiment and simulation are not compared in this work.

The 3D RPB geometry has been reproduced in Figure 5-1 according to the experimental rig [161]. The inner diameter, outer diameter and height of the wire mesh packing are 80, 300 and 20 mm, respectively, and it is made from stainless steel with an expanded mesh grade 707. The void fraction and specific area of the packing are 0.801 and 663 m²/m³, respectively. The diameter and the estimated height of the RPB casing are 360 and 180 mm, respectively and the space ratio of the outer cavity zone to the packing zone is about 11. There are two gas inlet tubes and one liquid inlet tube with diameters of 60 and 14 mm, respectively. In order to make the mesh in the outer cavity hexahedral and further reduce the mesh number, the shape of the gas inlet tubes and one liquid inlet

tube is simplified to be a rectangle but with the same flow cross-sectional area. In addition, a gas outlet tube is outside the liquid inlet tube with a diameter being 40 mm. A 2-arm liquid distributor is used, and its length and diameter are 22.4 and 7 mm, respectively. In Figure 5-1, only two liquid nozzle outlet holes are presented. In order to save computational time, the liquid flows passing through the liquid inlet tube and 2-arm liquid distributor has not been modelled. Initially, a liquid pressure outlet boundary was built at the bottom of the RPB to ensure that the liquid phase flows out from the RPB. However, after the simulation, we found that a large amount of the gas phase would flow out from this boundary at the same time. Thus, an elimination zone is employed at the bottom of the RPB to remove the liquid phase but to retain the gas phase, and the appropriate source equations for this zone can be found in Section 3.2 [6].

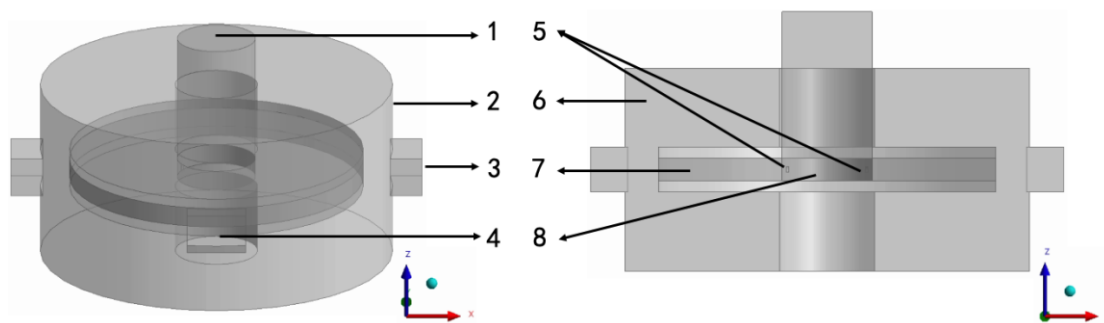


Figure 5-1 Schematic diagram of the 3D RPB (1, gas outlet; 2, case; 3, gas inlet; 4, liquid elimination zone; 5, liquid inlet; 6, outer cavity zone; 7, packing zone; 8, inner cavity zone).

5.2.2 Assumptions for the model

The main assumptions of the RPB model are as follows:

- (i) The wire mesh packed bed is a homogenous porous medium.
- (ii) The gas is incompressible.
- (iii) The pressure field is shared by the gas and liquid phases.
- (iv) The liquid phase exists in the form of the film and droplets in the packing and outer cavity zone.
- (v) The casing wall is adiabatic.

5.2.3 Properties of the fluids and boundary conditions

The gas phase comprises 12% CO₂ and 88% air. It is assumed that the gas phase consists only of CO₂, N₂, and O₂, and the component mole concentrations are detailed in Table 5-2. The liquid phase is the MEA solution with a CO₂ preloading of 0.1 mol CO₂/ mol MEA before injection into the RPB, but the preloaded CO₂ is then assumed to undergo a reaction with the MEA component, leading to the formation of MEAH⁺ and MEACOO⁻ in the solutions. Thus, the liquid phase is composed of MEA (HOC₂H₄NH₂), MEAH⁺ (HOC₂H₄NH₃⁺), MEACOO⁻ (HOC₂H₄NHCOO⁻) and water, and their mass concentrations are listed in Table 5-3. The correlations of the surface tension and viscosity for the MEA solution are present in Table 5-4 [185, 186]. In addition, the liquid density, thermal conductivity and specific heat of the two phases are evaluated by the mixing law based on every species in each phase.

Table 5-2 The mole fraction of each component in the gas phase.

CO ₂	N ₂	O ₂
0.12	0.6952	0.1848

Table 5-3 The mass fraction of each component in the MEA solutions.

MEA concentration	MEA $\text{HOC}_2\text{H}_4\text{NH}_2$	MEA H^+ $\text{HOC}_2\text{H}_4\text{NH}_3^+$	MEA COO^- $\text{HOC}_2\text{H}_4\text{NHC}\text{OO}^-$	H_2O
30% MEA	0.2349	0.0298	0.0501	0.6852
50% MEA	0.3861	0.0491	0.0823	0.4826
70% MEA	0.5331	0.0677	0.1136	0.2856

Table 5-4 The viscosity and surface tension of the MEA solutions [185, 186].

Liquid properties	Equation	Number	Reference
Viscosity of the MEA solution	$\mu_{0.3} = 0.3083 - 0.00262T + 7.4882 \times 10^{-6}T^2 - 7.17293 \times 10^{-9}T^3$	T-5-1	[185]
	$\mu_{0.5} = 0.7963 - 0.006744T + 1.915 \times 10^{-5}T^2 - 1.821 \times 10^{-8}T^3$		
	$\mu_{0.7} = 2.398 - 0.02056T + 5.897 \times 10^{-5}T^2 - 5.657 \times 10^{-7}T^3$		
Surface tension of the MEA solution	$\sigma_{\text{H}_2\text{O}} = 0.18548(1 - \frac{T}{647.13})^{(2.717+3.554(\frac{T}{647.13})+2.047(\frac{T}{647.13})^2)}$	T-5-2	
	$\sigma_{\text{MEA}} = 0.09945(1 - \frac{T}{614.45})^{(1.067)}$	T-5-3	[186]
	$\sigma_L = \sigma_{\text{MEA}} + \frac{2.129(1 - y_{\text{MEA}})}{(1 + (2.129 - (1 - y_{\text{MEA}})))(\sigma_{\text{H}_2\text{O}} - \sigma_{\text{MEA}})}$	T-5-4	

In the experiment conducted by Kolawole [161], all MEA solutions were preloaded to 0.1 mol CO_2 /mol MEA before the MEA solution was fed into the RPB. The same MEA

loading is employed in the CFD model. The gas flow rate is fixed at 42 kg/h with an inlet temperature of 40 °C according to the experimental settings and the gas outlet boundary is set as the pressure-outlet with a zero gauge pressure. In terms of the reverse flow at the gas outlet boundary, the CO₂ fraction on the inner packing surface is used as the CO₂ fraction in the gas outlet, which has been performed iteratively. In addition, different L/G mass ratios, e.g. L/G = 2.7, 3.1, 3.5 for 30% MEA, are tested in the model. Accordingly, the liquid inlet velocity ranges from 0.20 to 0.54 m/s with a temperature fixed at 40 °C and the liquid disappears after entering the liquid elimination zone. The species and their concentrations in the gas and liquid phases are presented in Table 5-2 and Table 5-3, respectively. The gravity force is set as 9.8 m/s² and in the -Y direction. The packing material is steel, with specific area and porosity values of 663 m²/m³ and 0.801, respectively. The rotating speeds employed in the experiment, including 600, 850 and 1150 rpm are used in the simulations. The sliding model has been performed to achieve the motion of the packing. The wall boundaries have been set as no slip and adiabatic.

5.2.4 Solution procedure

The 3D transient simulations have been performed using the ANSYS Fluent 2021 R1 in a double precision mode based on the High Performance Computing cluster in the University of Sheffield. The governing equations of the mass, momentum, energy and species were solved to investigate the hydrodynamics, thermodynamics and mass transfer in the RPB. The UDF has been developed for defining the properties of the MEA solution, implementing the extra forces in the momentum equations, and calculating the transferred CO₂ in the mass equations, etc. The equilibrium thermal

model was selected to calculate the heat transfer between the fluid and solid phases in the porous medium zone. The Phase Coupled SIMPLE method was applied, and the pressure equations were discretized by the second-order scheme. The pressure-based method and the absolute velocity formulation have been utilized. The time step was set as 5×10^{-4} s, and a maximum of 35 iterations was employed per time step, and the convergence tolerance was 1×10^{-5} . The simulation case can be assumed to be the pseudo steady state when the CO₂ concentration at the gas outlet and the liquid outlet temperature were reduced to within 0.1% in ten seconds, and the governing equations' residuals were less than 5×10^{-5} . Particularly, the energy residual was less than 5×10^{-7} .

For the RPB model, the realizable $k - \varepsilon$ turbulence model is more suitable for the RPB than the standard $k - \varepsilon$ model, and the reasons have been illustrated in last chapter [140].

5.2.5 Grid independence

Figure 5-2(a) shows the outside and inside mesh layouts of the 3D pilot-scale RPB model generated by the ANSYS Mesh. In addition to the packing region, the flow characteristics change evidently in the middle of the outer cavity zone and the inner cavity zone, the meshes in these areas are finer compared with the top and bottom cavity zones. To reduce the number of cells and improve the calculation accuracy [53], the structured hexahedral grids were generated in the whole RPB except in the inner cavity zone. Various numbers of the grid cell were tested with total cells of 0.16 M, 0.26 M, 0.42 M and 0.76 M in order to obtain a mesh independent solution, which is shown in Figure 5-2(b). According to Figure 5-2(b), after a grid of 0.42 M cells is employed, the CO₂ capture rate and liquid outlet temperature reached a stable solution. Therefore, the

grid of 0.42 M cells, including 0.05 M cells in the packing zone and 0.28 M cells in the outer cavity zone, was applied. The minimum and largest mesh volumes are 1.4×10^{-10} and $3.3 \times 10^{-7} \text{ m}^3$, respectively, and the average skewness and element quality are 0.11 and 0.85, respectively.

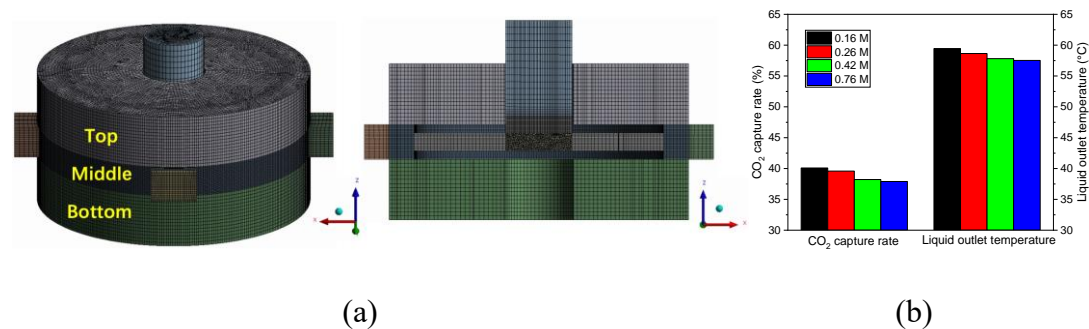


Figure 5-2 (a) Schematic of the mesh in the 3D model and (b) predicted CO₂ capture rate and liquid outlet temperature using different grids.

5.3 Results and discussion

In order to validate the CFD model developed, 27 simulation cases have been compared with various experimental cases based on the operating conditions shown in Table 5-1, and all the major variables have been critically analyzed. After that, the effects of various operational parameters on the mass transfer process have been investigated. In addition, the ratio of the CO₂ captured in the outer cavity zone to that in the entire RPB has been investigated.

5.3.1 Validation and the distribution of variables

For validating the developed 3D RPB model, the obtained CO₂ mole fraction in the gas outlet and the liquid temperature at the liquid outlet, which could reflect the mass and heat transfer performance, are compared with the experimental results in the Kolawole

thesis [161]. The important operating conditions are listed in Table 5-1. Although the flow dynamics may be compared via the liquid holdup, unfortunately, this parameter has not been measured in the experimental investigation.

Figure 5-3 presents a comparison of the CO₂ fractions in the gas outlet and the liquid outlet temperatures obtained from the experiments and simulations under various operating conditions, including the MEA concentration, rotational speed and the L/G mass ratio. From Figure 5-3(a), it is observed that all relative deviations of the CO₂ mole fraction are within 15%. In addition, the CO₂ fraction for the 50% MEA solution has a better agreement with the experimental data, whose relative deviations are less than 6%. According to Figure 5-3(b), most of the relative deviations of the liquid outlet temperature are less than 10% and only a few points for the 70% MEA solution with a lower rotational speed of 600 rpm are larger than 10%. The difference between the simulations and experimental results may mainly result from the difficulties and uncertainties in measuring the variables since the experiments have been conducted in a relatively small reactor [6]. In addition, the employed empirical correlations may not be suitable for this RPB model since these correlations were derived from different RPB sizes, operating conditions, etc. For example, the correlation for the liquid droplet diameter in the packing and outer cavity zones does not account for the influence of the packing properties and structure, including the number of layers and shape of the wire mesh, which may lead to an inaccurate prediction for the heat transfer, as evident in Equations (3-42) and (3-62). This discrepancy may account for the higher predicted liquid outlet temperature observed in Figure 5-5(b). Also, the phase properties, such as the surface tension and viscosity of the MEA solution, might become challenging to

accurately evaluate using the corresponding correlations as the temperature and CO₂ loading increase. It can be found that the average absolute relative deviations in the CO₂ fraction and liquid outlet temperature are smaller than 7% and 6%, respectively, thus indicating that the effective interfacial area, mass and heat transfer models could describe the thermodynamics and mass transfer processes within the RPB. Furthermore, the same sub-models, such as the hydrodynamics, including the interfacial, drag, capillary pressure and mechanical dispersion force models, have been verified in the previous model that was derived in Chapter 4 using a smaller RPB model. Therefore, it can be concluded that the developed 3D RPB model gives a good match to the experimental results, and, with confidence, it can be employed to investigate the CO₂ capture process within this RPB. It should be noted that although the overall CFD results agree with the experimental data for this RPB, further validation may be required when applying the sub-models to other RPBs, in particular when different packings are employed.

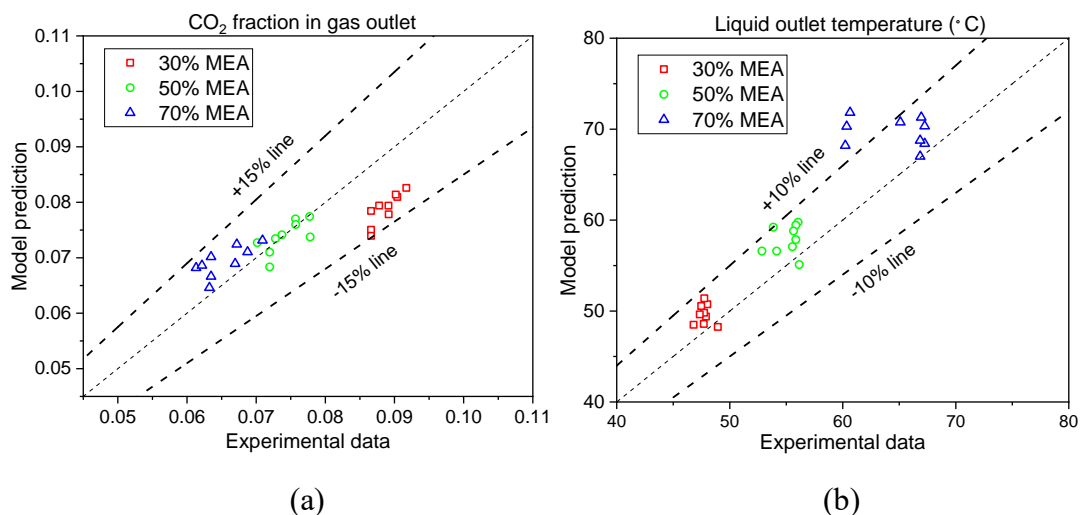


Figure 5-3 Comparison of the (a) CO₂ mole fraction in the gas outlet; (b) liquid outlet temperature [161].

In addition, the distributions of some important variables are presented in order to analyze the hydrodynamics, thermodynamics, and reaction-enhancement mass transfer within the RPB. Figure 5-4 presents the predicted variables for the MEA solutions with the lowest (30%) and highest (70%) concentrations. Also, the cases are performed with the rotational speed being 850 rpm and the L/G ratios being 3.1 and 1.5 for 30% and 70% MEA solutions, respectively, whose relative deviations are relatively small as shown in Figure 5-3. Since the vectors of the gas and liquid velocities are similar for the 30% and 70% MEA solution, only the vectors for the 30% MEA solution in half of the RPB cut from the central plane is presented in Figures 5-4(a) and 5-4(b) in order to observe them clearly. Figure 5-4(a) shows that the liquid flows tangentially due to the interaction with the packing and its velocity gradually increases on the way outwards through the packing. Near the outer packing surface, the liquid velocity reaches a maximum and then the liquid velocity suddenly reduces in the outer cavity zone due to the interfacial force between the gas and liquid phases. In addition, the liquid also rotates with a small velocity in the bottom outer cavity zone. From Figure 5-4(b), it is observed that the gas phase that radially flows from the gas inlet, begins to rotate after entering the outer cavity zone under the effect of the rotational packing. Its motion is in rapid synchronization with the rotating packing in the outer packing zone and it reacts with the MEA solution when passing through the packing region. It is worth mentioning that although the vectors of the phase velocity in Figures 5-4(a) and 5-4(b) look very similar, the radial flow directions of the gas and liquid phases are in the opposite directions.

In order to clearly observe the liquid holdup in the packing region, the maximum value

of the scale in Figure 5-4(c) is set as 0.1 instead of 1.0. According to Figure 5-4(c), it is observed that the liquid holdup gradually reduces along the radial direction in the packing zone and this is due to the increasing flow space. Although the liquid holdup data is not available in the Kolawole's thesis, this phenomenon has been accurately predicted by other simulation and experimental investigators [34, 60]. After flowing out from the packing region, the liquid radial velocity suddenly increases without the restriction of the porous resistance, thus causing the liquid fraction to become quite small in the outer cavity zone. Subsequently, the liquid droplets collide on the casing wall and flow downwards under the influence of the gravitational force. Thus, the liquid with a higher volume fraction may be observed on the casing wall surface.

Also, it can be found that the liquid holdup for the 30% MEA solution is clearly larger than that for the 70% MEA solutions as the ratio of the liquid flow rate for 30% to 70% MEA is 2.1. However, the ratio of the liquid holdup in the packing regions for 30% to 70% MEA is about 1.6, which is smaller than the ratio of the liquid flow rate of 2.1, meaning that the 70% MEA solution is more likely to retain in the packing region. Due to the higher viscosity of the 70% MEA solution, the thickness of the liquid film increases and the velocity of the liquid flow decreases [31]. As a result, the effective interfacial area for the 30% MEA solution is larger, see Figure 5-4(d), since more liquid is attached to the wire mesh packing surface, or it is split into numerous small droplets in the packing zone [63, 64]. This means that the contact area between the gas and liquid phases is larger, thus indicating that the 30% MEA solution has more chance to interact with the CO₂.

Although the liquid holdup and contact area are larger for the 30% MEA solution

resulting from the larger liquid flow rate, the CO₂ fraction in the gas outlet is higher and this may be seen by comparing the two illustrations in Figures 5-4(e) and 5-4(g). This is because the CO₂ capture performance is not only related to the liquid holdup and contact area, but also it is affected by some other parameters, such as the MEA concentration, liquid temperature and residence time. Clearly the MEA concentration is the dominant factor in determining the CO₂ capture process. For the CO₂-MEA absorption system, the heat will be released when the CO₂ is captured in the MEA solution, thus leading to an increasing liquid temperature. Simultaneously, some heat is taken away by the opposing gas flow via the heat transfer and the rest of the heat remains in the liquid phase. This could be the reason why the liquid temperature for the 70% MEA solution is higher than that for the 30% MEA solution, see Figures 5-4(f) and 5-4(h), because more active MEA participates in the reaction and releases more heat to the already smaller flow rate of the liquid phase [187]. This phenomenon is clearer in the top and bottom outer cavity zones, where the liquid fraction is quite low and the liquid temperature could be even up to 89 °C. In return, the chemical reaction is faster when the phase temperature is higher. In addition, the phase temperature could also influence the physical properties, including the viscosity and density, which further has an impact on the flow dynamics, such as the liquid holdup and residence time. Thus, this indicates that the liquid holdup, CO₂ capture rate, and liquid temperature could affect each other in this system. The predicted variables can be made accurate and stable only when all the parameters related to the flow dynamics, mass and heat transfer are set properly and these processes reach a balance within the whole RPB.

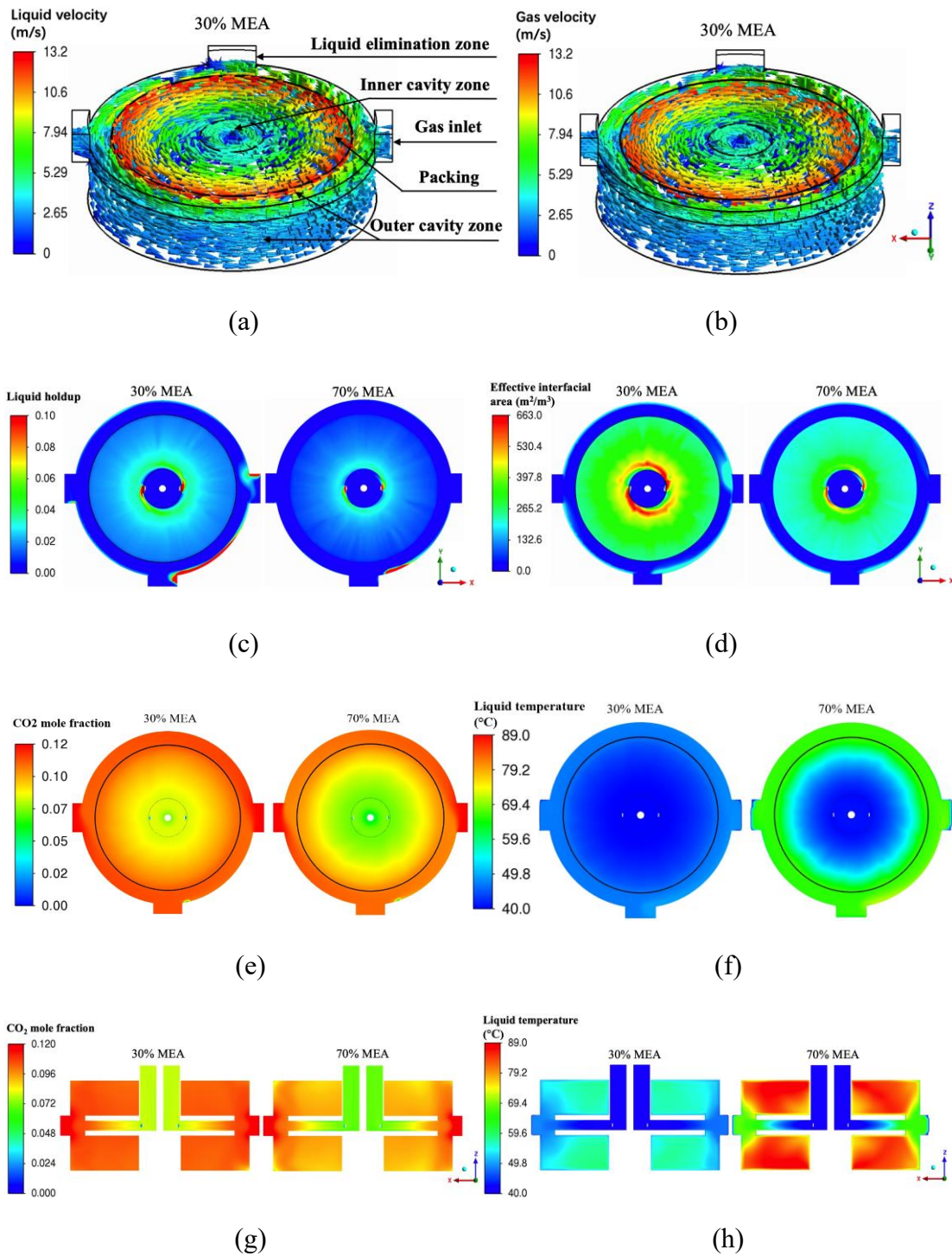


Figure 5-4 Vectors of the (a) liquid velocity; (b) gas velocity; contours of the (c) liquid holdup; (d) effective interfacial area on the planes $z = 0.01$; (e) CO_2 fraction in the gas phase; (f) liquid temperature on the planes on the planes $z = 0.01$; (g) CO_2

fraction in the gas phase; and (h) liquid temperature on the planes $y=0$ for 30% and 70 % MEA.

5.3.2 Mass transfer in different zones in the RPB

As we know, the CO₂ absorption within a RPB mainly occurs in two zones: packing and outer cavity zones. Based on the newly developed 3D entire RPB model, the CO₂ capture process in the packing and outer cavity zones is separately analyzed by using the CFD method.

Taking the 50% MEA solution with a L/G ratio of 2.1 in Section 5.3.1 as an example, Figures 5-5(a), 5-5(b) and 5-5(c) show the circumferentially averaged liquid holdup and effective interfacial area (per unit, m^2/m^3), liquid velocity, as well as the CO₂ mole fraction in the gas phase and the liquid temperature along the radial direction, respectively. For $r_i \leq r \leq r_o$, these parameters are only circumferentially averaged in the packing region rather than including the top and bottom cavity zones. When flowing into the inner packing zone, with a radial velocity only, the liquid violently collides with the rotational packing and it is quickly dispersed, thus generating numerous very small tiny droplets, or forming thin films on the wire mesh surface. Due to the small flow space in the inner periphery of the packing, a large effective interfacial area could be observed in Figure 5-5(a), which is defined as the “end-effect zone” - a zone where excellent micromixing occurs due to the strong interaction and liquid dispersion [13, 188]. Although the phase surface renewal is fast and the effective interfacial area (m^2/m^3) is large in the end-effect zone, the physical mass transfer area (m^2) is small because the volume of this zone is too small. In addition, the liquid temperature and local CO₂ fraction in the gas phase flow are relatively low in this zone. As a result, a

sharp decrease in the CO₂ fraction is not observed in Figure 5-5(c).

Soon after entering the bulk of the packing zone, the liquid starts to synchronize with the rotating packing, and its tangential velocity almost coincides with the packing rotational velocity in Figure 5-5(b). Consequently, the liquid dispersion is relatively weak, thus the effective interfacial area decreases along with the radial position in Figure 5-5(a) [18]. Since smaller droplets and thinner film are formed in this region, the liquid radial velocity gradually decreases due to the larger interfacial and drag forces, which is shown in Figure 5-5(b). In this packing region, most of the CO₂ is captured and a large amount of heat is released, and this is due to the large contact area and the enhanced surface renewal of the phases [14]. Therefore, the CO₂ fraction in the gas phase reduces and the liquid temperature increases on their way through the packing as shown in Figure 5-5(c).

After flowing out from the outer edge of the packing, the liquid droplets with large velocity pass through the cavity space, causing a sudden decrease in the effective interfacial area and liquid holdup as shown in Figure 5-5(a). Despite the relatively low average effective interfacial area (m^2/m^3) in the outer cavity zone, the volume of this zone (m^3) is large. Therefore, the gas-liquid contact area (m^2) within the zone is substantial, and the contribution of the outer cavity zone to the total mass transfer can still reach 34%. Without the interaction with the packing, the liquid flow direction is almost unchanged in the outer cavity space, thus causing the liquid radial velocity component to increase and the tangential velocity component to decrease as shown in Figure 5-5(b). As a result, the difference between the gas and liquid radial velocity increases, which leads to an increase in the interfacial force between the two phases and

a decrease in the total liquid velocity. In addition, an increase in the liquid temperature can be observed in Figure 5-5(c) due to the high liquid temperature in the top and bottom regions of the outer cavity zone (see Figure 5-4(f)). Then the liquid droplets collide on the inner casing wall, generating the liquid film and a large number of splashing droplets [42]. These phenomena have been modelled well with a steep increase in the liquid holdup and effective interfacial area, see Figure 5-5(a). The liquid film on the casing wall reacts with the CO₂, releasing reaction heat into the liquid phase. However, due to the smaller area available for gas-liquid heat transfer compared to the liquid droplets, more heat remains in the liquid phase. As a result, there is another sharp increase in the liquid temperature near the casing wall, as shown in Figure 5(c).

In general, the outer cavity zone's volume is much larger than the packing region. For instance, the volume of the outer cavity zone to the packing region is about 11 for the present employed RPB model. However, most of the CO₂ is captured in the packing region instead of the outer cavity zone, which means that the larger the volume of the packing occupied in the fixed entire RPB, the more effective is the CO₂ absorption.

Based on the validation cases under various operating conditions shown in Figure 5-3, it is found that the outer cavity zone takes up 25%~40% of the total mass transfer area and the effect of the outer cavity zone on the mass transfer could range from 28% to 42% for this case study. From the wide range of the contribution of the mass transfer and mass transfer area in the outer cavity zone, it is known that the CO₂ capture process in the packing and outer cavity zones are quite different under various operating conditions. With the aim of providing some useful and important suggestions for RPB design and scaling up, the contribution of the CO₂ removal and mass transfer area in

different zones has been investigated, which is presented in the following section.

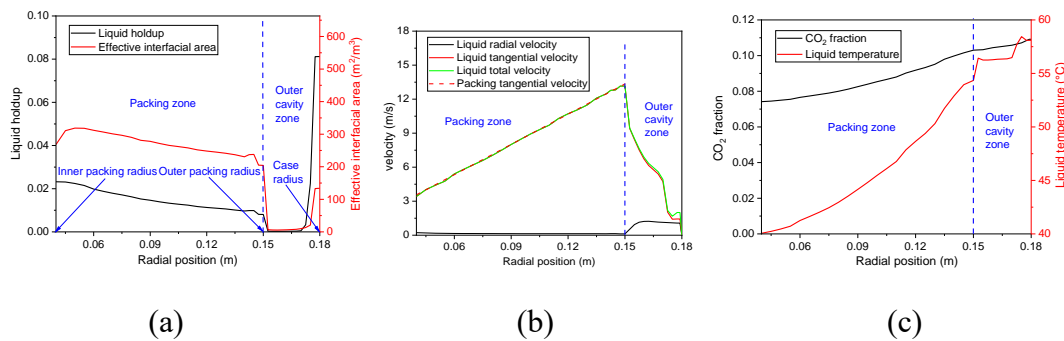


Figure 5-5 The circumferentially averaged (a) liquid holdup and effective interfacial area; (b) liquid and rotating packing velocities and (c) CO₂ mole fraction in the gas phase and liquid temperature along the radial direction.

5.3.3 Effect of the operating parameters

Among the three MEA concentrations investigated, the relative deviation of the CO₂ fraction in the gas outlet between the experiment and simulation for the 50% MEA solution is small, as discussed in Section 5.3.1. Thus, the 50% MEA solution is selected as the baseline case for discussion, and its operating conditions are listed in Table 5-5.

Table 5-5 The operational conditions for the baseline case.

MEA concentration (%)	L/G ratio	Rotational speed (rpm)	Liquid inlet temperature (°C)	Gas flow rate (kg/h)
50	2.1	850	40	42

For evaluating the CO₂ absorption performance in the entire RPB, the overall volumetric mass transfer coefficient ($K_L a_e$), a parameter that may determine the rate at which a gaseous compound (CO₂) can transfer from the gas phase to the MEA solution, is introduced along with the liquid temperature at the liquid outlet. The equation for $K_L a_e$ is shown in Equation (6-1). $K_L a_e$ becomes larger when the CO₂ fraction in the

gas outlet (y_{o,CO_2}) is lower, indicating a better CO₂ capture performance.

$$K_L a_e = \frac{Q_G}{\pi(r_o^2 - r_i^2)h} \ln\left(\frac{y_{i,CO_2}}{y_{o,CO_2}}\right) \quad (6-1)$$

The ratios of the captured CO₂ (r_c) and the mass transfer area (r_e) in the outer cavity zone to those in the whole RPB are examined in order to analyze the mass transfer in different zones. The expression for r_c and r_e are given as follows:

$$r_c = \frac{y_{i,CO_2} - y_{op,CO_2}}{y_{i,CO_2} - y_{o,CO_2}} \quad (6-2)$$

$$r_e = \frac{\int_o a_e dV}{\int_p a_e dV + \int_o a_e dV} \quad (6-3)$$

5.3.3.1 Effect of the MEA concentration

It is known that the CO₂ capture efficiency increases when using the solution with a higher MEA concentration. In terms of the flow dynamics, the liquid phase can lead to early flooding or abnormal distribution in the packing of a CPB due to the large viscosity of the liquid phase. However, one of the advantages of applying the RPB is that a higher MEA concentration solution with larger viscosity can fluently pass through the packing due to the higher gravitational environment.

Figure 5-6(a) illustrates the influence of the MEA concentration on the CO₂ absorption and thermodynamics in the RPB in terms of $K_L a_e$ and liquid temperature at the liquid outlet. In this case study, the MEA concentration varies from 30 to 70% while keeping all the other operating conditions consistent with the base case. It can be observed that the magnitude of the increased $K_L a_e$ and liquid outlet temperature significantly becomes larger when using a higher MEA concentration solution since the increased

active MEA available in the solution could remove more CO₂ from the gas phase and more reaction heat would be generated at the same time [189]. Although the solution with a higher MEA concentration favors for the CO₂ absorption, the greater trend for corrosion, degradation and foaming should be carefully considered before the PCC industrial application.

Figure 5-6(b) illustrates the ratios of the CO₂ capture and mass transfer area in the outer cavity zone to the whole RPB under the same operating conditions as Figure 5-6(a). On one hand, the mass transfer area mainly depends on the liquid flow rate and rotational speed instead of the MEA concentration. On other hand, the increasing temperature shown in Figure 5-6(a) affects the phase properties, such as the density and viscosity. As a results, the r_e changes only slightly in Figure 5-6(b).

On considering Figure 5-6(b), the liquid temperature approximately reaches the maximum after entering the outer cavity zone, which means that the average liquid temperature is relatively high in the outer cavity zone compared with that in the packing zone. The higher liquid temperature benefits the reaction rate. Therefore, the proportion of the CO₂ removed in the outer cavity zone (r_c) increases as the MEA concentration increases. From the above analysis, it is indicated that the higher MEA concentration could enhance the CO₂ capture in the full RPB, and more proportions of CO₂ are captured in the outer cavity zone.

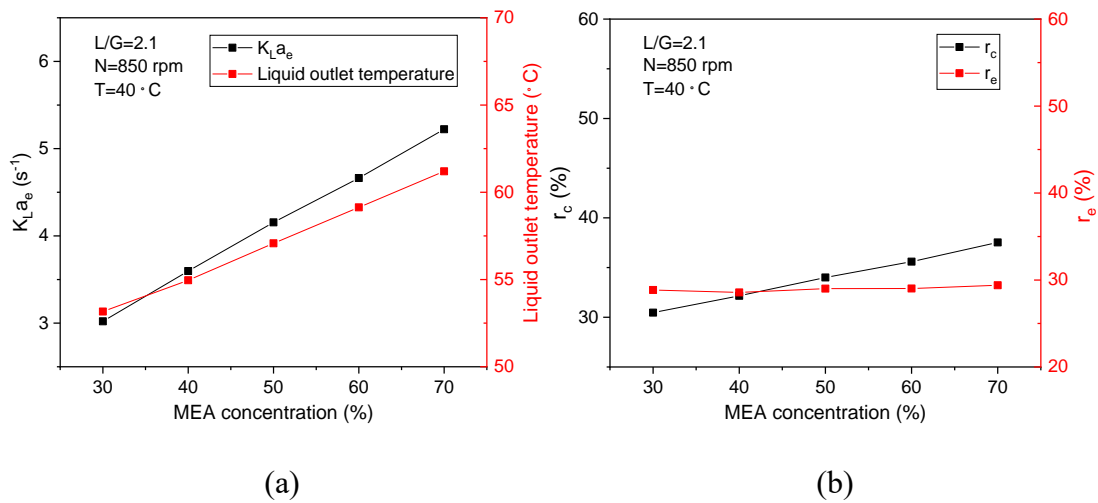


Figure 5-6 The effect of the MEA concentration on (a) $K_L a_e$ and the liquid outlet temperature and (b) ratio of the contribution of CO₂ capture and mass transfer area in the outer cavity zone.

5.3.3.2 Effect of the liquid flow rate

For post-combustion capture using the CPB, it is reported that the liquid outlet temperature and CO₂ capture level increase when the L/G ratio increases due to the larger amount of free amine molecules and the higher effective interfacial area [190]. However, a reduced liquid outlet temperature is observed in the RPB from the experimental work [161]. Therefore, it is worth exploring the difference in the CO₂ capture processes under various L/G ratios within the CPB and RPB.

Figure 5-7(a) presents the predicted impact of the L/G ratio on $K_L a_e$ and liquid outlet temperature with the L/G ratio ranging from 1.5 to 2.7 while keeping the gas flow rate unchanged. As the L/G ratio increases, more CO₂ is captured resulting from the larger amount of free amine molecules and also the mass transfer resistance is reduced due to the enhanced gas-liquid mixing [109] and liquid film refreshing. In addition, the

increasing L/G ratio leads to a higher effective interfacial area. These factors increase $K_L a_e$, but this increase tends to slow down as L/G increases. Although the increasing number of tiny droplets could be generated, the increase in the effective interfacial area is limited at the higher range of the liquid flow rate [191]. Similarly, although more heat is generated as the L/G ratio increases, the heat generation is not high enough to increase the liquid temperature due to the large sensible heat of the liquid phase. In addition, this may explain the decreasing liquid outlet temperature in Figure 5-7(a), which is consistent with Kolawole's experimental results [161]. This is different from that typically observed in a CPB because the liquid flow rate in a CPB is the dominant factor that could significantly increase the mass transfer area leading to the significantly increased mass transfer and heat generation. From the above analysis, the increased liquid flow rate and mass transfer area as well as the decreased liquid temperature together cause $K_L a_e$ to increase more slowly [192].

Figure 5-7(b) shows the ratios of the CO₂ capture and mass transfer area in the outer cavity zone to the whole RPB for L/G ratio from 1.5 to 2.1. The r_c and r_e slightly change with changing the L/G ratios, but it is noted that a critical point is observed in Figure 5-7(b). As the L/G ratio increases from 1.5 to 2.1, more liquid concentrates in the outer cavity zone and the temperature in this zone is relatively higher. As a result, both r_c and r_e increase. While the L/G ratio continues to increase, the liquid turbulence is dominant in the packing region and the liquid temperature continues to decrease in the outer cavity zone. As a result, the CO₂ that is captured in the packing increases, thus leading to a reduced value of r_c and r_e .

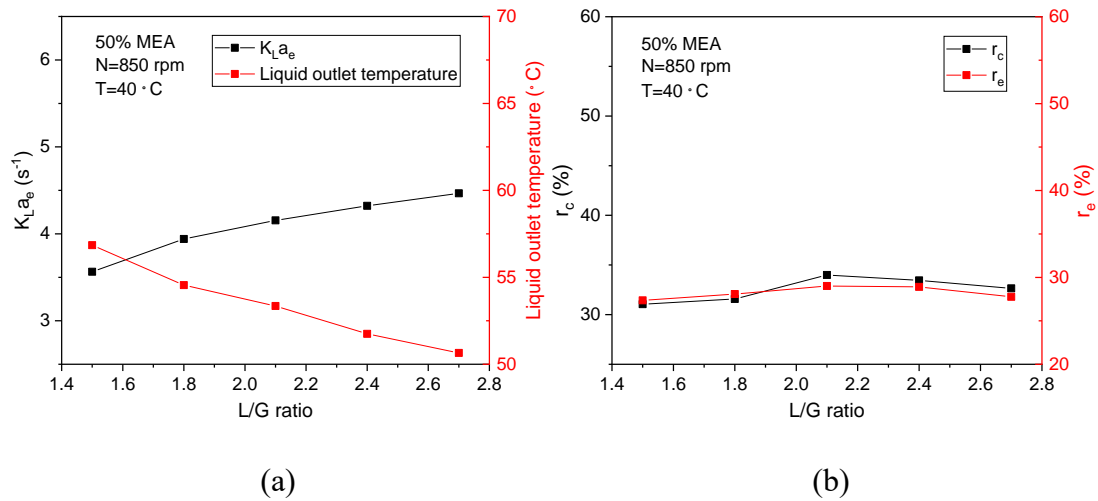


Figure 5-7 The effect of the L/G ratio on (a) $K_L a_e$ and liquid outlet temperature and (b) ratios of the contribution of CO₂ capture and mass transfer area in the outer cavity zone.

5.3.3.3 Effect of the rotational speed

In the previous chapter, it was reported that the rotational speed has a considerable impact on the liquid holdup and liquid distribution, thus it will further affect the CO₂ capture in the RPB absorber. In addition, the rotational speed could directly affect the effective interfacial area and the reaction time between the liquid and gas phases. Thus, it is a key parameter for the PCC in a RPB.

Figure 5-8(a) presents the impact of the rotational speed on the $K_L a_e$, the liquid outlet temperature of the entire RPB and the liquid temperature at the outer packing boundary. Figure 5-8(b) illustrates the ratios of the CO₂ captured and mass transfer area in the outer cavity zone to the whole RPB under various rotational speeds. As the rotational speed increases, the liquid holdup in the packing region reduces due to the stronger centrifugal force. However, more tiny liquid droplets are formed among the packing

region, which results in an improved effective interfacial area [140], although the magnitude of the improvement is very limited. On the other hand, the liquid fraction in the outer cavity zone becomes larger because the liquid accumulation in the outer cavity zone relies on the gravitational force to remove out of the RPB. In addition, more liquid is more likely to attach the casing wall and retain in the bottom of the casing when employing a higher rotational speed, which leads to a significant increase in the mass transfer area in the outer cavity zone. Thus, the r_e in Figure 5-8(b) gradually increases as the rotational speed increases. In addition, the increasing mass transfer area in both the packing and outer cavity zones makes the $K_L a_e$ increase as shown in Figure 5-8(a). From Figure 5-8(a), the liquid temperature flowing out the packing region (blue line) increases with the rotational speed increasing and it is always lower than the liquid outlet temperature (red line). However, the liquid outlet temperature reduces when the rotational speed increases from 600 to 850 rpm. The possible reason is that in the outer cavity zone, the liquid fraction increases more significantly compared with the increase in the mass transfer area when the rotational speed increases from 600 to 850 rpm. Also, the reaction heat generated in this zone at 850 rpm cannot significantly increase the temperature of the liquid. Therefore, the liquid outlet temperature at 850 rpm slightly reduces from the value at 600 rpm.

In addition, r_e increases as the rotational speed increases, thus, r_c is expected to increase accordingly. However, r_c reduces in the range of 300 to 850 rpm as observed in Figure 5-8(b). The possible reason is that the micromixing performance in the packing region improves significantly at the lower rotational speed [193]. As a result, the packing region captures more CO₂ compared with the outer cavity zone when the

rotational speed increases from 300 to 850 rpm. Overall, the $K_L a_e$ and r_e increase with the increase in the rotational speed, and r_c decreases first and then increases.

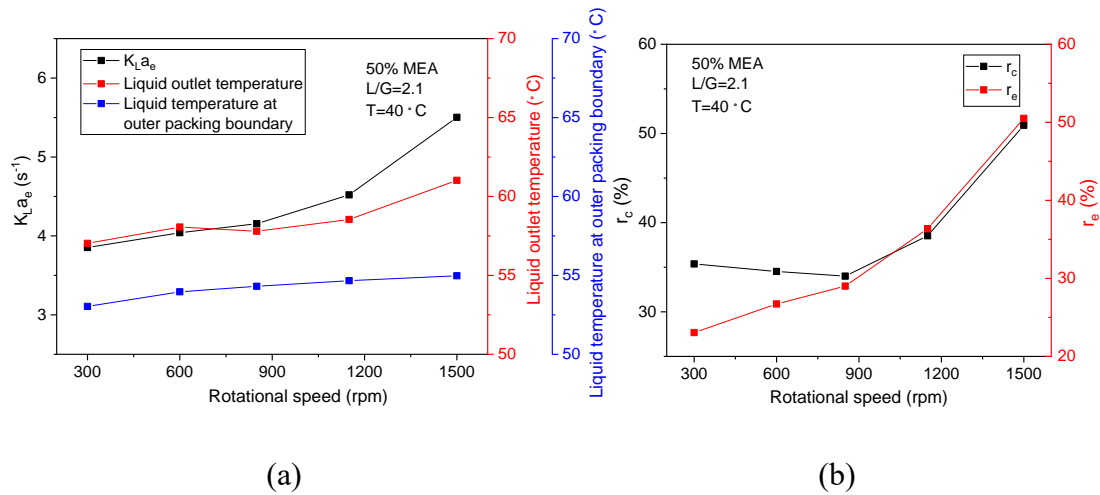


Figure 5-8 The effect of the rotational speed on the (a) $K_L a_e$ and liquid temperatures at the liquid outlet and outer packing boundary and (b) ratios of the contribution of CO_2 capture and mass transfer area in the outer cavity zone.

5.4 Conclusions

This chapter has established a new and important full 3D RPB model using the Eulerian porous medium approach, and the physical and chemical processes occurring in the packing and outer cavity zone of a pilot scale RPB have been modelled. The overall CFD results agree with the experimental data. Nonetheless, further validation may be required when applying the sub-models to other RPBs, in particular when different packings are employed. The main findings of this chapter are as follows:

- (i) A new completed 3D Eulerian porous medium RPB model was established based on a pilot scale RPB model. By using the Eulerian porous medium modelling method, the CO_2 absorption performance within a whole RPB could

be effectively investigated due to the significantly reduced computational cost.

- (ii) The force, effective interfacial area, heat transfer, mass transfer models were coupled with the Eulerian RPB model, thus, the hydrodynamics, thermodynamics and mass transfer processes could be thoroughly analyzed.
- (iii) The effective interfacial area, force and even liquid droplet diameter models were introduced separately for the packing region and the outer cavity zone for predicting the CO₂ capture performance inside the full RPB, and the CO₂ absorption processes in these zones were quantitatively evaluated under various operating conditions by the CFD method for the first time.

The predicted simulation results are in good agreement with the experimental data by comparing the CO₂ fraction in the gas outlet and liquid outlet temperature. In addition, the end-effect zone is observed near the inner packing region where a strong micromixing occurs due to the liquid dispersion and strong interaction between the liquid and packing. However, the amount of the CO₂ transferred between the phases is small in the end-effect zone due to the small local CO₂ fraction in the gas phase and the low liquid temperature.

The outer cavity zone has an effect on the CO₂ capture inside the RPB. The contributions of the outer cavity zone to the total mass transfer area and CO₂ capture are in the ranges of 25%~40% and 28%~42%, respectively, in the RPB investigated in this work. However, of course, these values may be different for different designs. Also, the simulation results show that the CO₂ captured in the outer cavity zone becomes more as the MEA concentration increases, however, the MEA concentrations have little

effect on the ratio of the mass transfer area in the outer cavity zone to the whole RPB. The contributions of the outer cavity zone to the mass transfer area and the CO₂ capture change slightly with the L/G ratio increasing. With the increase in the rotational speed, the ratio of the mass transfer area in the outer cavity zone to the whole RPB increases, however, the ratio of the CO₂ capture in the outer cavity zone to the whole RPB first decreases slightly and then increases significantly.

The RPB model developed in this chapter can successfully and effectively predict the CO₂ capture process in the whole RPB, and this demonstrates the substantial potential of the model, with further validation, to be used for process optimization and design of the large-scale RPB for industrial PCC. There are two limitations of the CFD model proposed in this study. The first is that using the porous media approach, the details of the fluid flows are not resolved, and therefore the characteristics of the formation of liquid droplets/films are unable to be revealed. Secondly, the accuracy of the model is highly dependent on the applicability of the sub-models employed and therefore, careful validation of the model should be considered, especially when a very different packing is employed for the RPB.

CHAPTER 6 : CRITICAL COMPARISON BETWEEN THE LARGE-SCALE RPB AND CPB FOR PCC

Summary

This chapter introduced a method to critically compare the CPB and RPB for the post-combustion carbon capture. A large-scale RPB has been computationally established according to the experimental parameters from a CPB pilot plant and the design procedure. The Eulerian porous medium method and various sub-models have been employed in order to effectively and extensively investigate the CO₂ capture processes. In addition, the process optimization of the CO₂ capture has been quantitatively performed. The simulation results show that compared with the CPB, the volume of the packed bed could be reduced by 80% using the RPB. In addition, the liquid flow rate could be saved 40% when using the 50% MEA concentration solution. This study provides very valuable and important information for the scaling up and operation of RPBs for post-combustion carbon capture.

6.1 Introduction

The RPB has shown many remarkable advantages over the CPB, such as the large effective interfacial area and small footprint. Thus, it has been utilized in many industries in order to improve the mass transfer performance. The RPB has been rarely

employed for commercial CO₂ capture and this is mainly due to three reasons.

The first reason is that the design procedures for the large-scale RPB have not, as yet, been proposed for PCC. Although a general design procedure has been mentioned in the works of Agarwal et al. [13] and Sudhoff et al. [133], it may not be suitable for the PCC process. In their design procedure, some overall volumetric mass transfer correlations that are derived from various absorption systems are utilized to determine the packing size [194]. However, they cannot be used since these general correlations may be not suitable for the CO₂-amine system. Therefore, systematic design procedures for the large-scale RPB should be carefully considered for the carbon capture.

Secondly, even though the large-scale RPB has been constructed for industrial CO₂ capture, how to operate a CO₂ capture plant with the RPB absorber is another issue. In fact, the effect of the operating parameters on the hydrodynamics and CO₂ capture performance have been investigated by using the experimental and simulation approaches [6, 25, 31, 53, 75, 89, 102, 134, 135]. However, these investigations have been conducted based on the lab-scale or pilot-scale RPBs with the outer packing diameter being smaller than 0.3 m. It is unknown whether the conclusions drawn by these small RPBs are still suitable for the large-scale RPB since the CO₂ capture processes in multi-scale RPBs may be different. Therefore, the sensitivity of the operating parameters on the CO₂ capture processes inside a large-scale RPB should be more thoroughly investigated in order to provide more important information on the operating and process optimization.

Finally, the advantage of the RPB over the CPB has not been thoroughly and clearly established. Currently, almost all the results published in the literature indicate that the

RPB has a much better mass transfer performance than the CPB based on both the lab-scale and pilot-scale facility size [83, 136-139]. However, the mass transfer rate will decrease with the increase in the radial length of the packing because the interaction between the liquid phase and the packing becomes weaker, especially in a large-scale RPB [140], which is different from the CPB. In addition to the capture level, the equipment size for the RPB would be reduced, which results in a smaller capital cost. However, it is difficult to determine whether the RPB is more cost-effective when considering the extra energy demanded by the rotor, although it has shown that the energy required by the motor is extremely smaller than regeneration energy in the work of Chamchan et al. [141]. More importantly, the regeneration energy would be significantly saved if the liquid flow rate required by the RPB could be reduced. Overall, the RPB and CPB should be more thoroughly compared when employing them for CO₂ capture.

In order to establish the large-scale RPB model and critically compare the RPB and CPB, the CPB experiments for CO₂ capture that were previously conducted by our research group [195, 196] are utilized as the reference data. The experimental campaign was performed at the Pilot-scale Advanced Capture Technology (PACT, now the TERC) facilities in Sheffield with a CO₂ capture capacity of one ton per day. The reasons why choosing this set of experimental data as the reference data are as follows. Firstly, the detailed dimensions of the CPB is presented, which could help to compare the volume ratio between the CPB and RPB. Secondly, the CO₂ capture performance was fully investigated under various operating conditions, and the important indexes, such as the CO₂ capture rate, CO₂ rich loading, liquid temperature distribution, etc., were given,

thus indicating that the CO₂ capture process in the RPB and CPB could be comprehensively compared. Thirdly, the experimental data has been utilized to validate the model established by using Aspen HYSYS, which indicates that the experimental data is reliable. Most importantly, an RPB experimental rig is being established based on this CPB experimental data, thus, this work may provide some suggestion for operation of the RPB.

Within the CPB absorber, the 30% MEA solution flows in a counter-current manner to the flue gas. The CPB is packed with a random stainless-steel packing- INTALOX Metal Tower Packing (IMTP25). Its porosity and specific area are 0.971 and 242.8 m²/m³. The diameter and height of the packing are 0.3 and 8 m, respectively. The CPB experiments are performed under a fixed gas flow rate of 210 m³/h and with a CO₂ mole concentration of 9.9%, and to achieve a 90% CO₂ capture level, the liquid flow rate of the MEA solution requires 721 kg/h. The inlet temperature of the liquid phase is 40 °C, and the CO₂ loading in the lean MEA solution is 0.204 mol CO₂ /mol MEA. The detailed information on the CPB experiment is listed in Table 6-1.

Table 6-1 The experimental data from the CO₂ capture plant using CPBs in the PACT facilities [196].

Packing diameter and height (m)	CO ₂ inlet concentration (%)	Gas flow rate (m ³ /h)	Liquid flow rate (kg/h)	Lean solvent concentration (wt %)	Lean loading (mol CO ₂ /mol MEA)	CO ₂ capture level (%)
0.3, 8	9.9	210	721	30.5	0.204	90.8

Based on the operating conditions of the CPB experimental investigation, a large-scale RPB was simulated by employing the Eulerian porous medium model to explore the

CO₂ capture processes. Also, hydrodynamics, thermodynamics and mass transfer were investigated by employing various sub-models, and the sub-models employed in this chapter have been illustrated in a flowchart in Section 3.9. Then, the CPB and RPB are quantitatively compared under various operating parameters for the CO₂ capture. This work quantitatively demonstrates the advantages of using RPB for the carbon capture and provides some very useful and important suggestions for RPB scaling up and plant operation.

6.2 Design procedure for the RPB

In this section, the large-scale RPB size is determined based on a design procedure [197] and the operating condition from the CPB experiments [196]. Since the mass transfer mainly occurs in the packing region, only the packing region is designed. In addition, in order to deal with the same large flue gas employed in the CPB, the packing size should be carefully considered.

The order to determine the size of the RPB is summarized as follows: (i) the inner packing radius is first obtained according to the proper gas withdrawal; (ii) the packing width is fixed based on the flooding point; and (iii) the outer packing radius is finally calculated in terms of the desired capture rate. In addition, the processes for determining the liquid distributor and packing are also included in this section.

6.2.1 Inner packing radius

In order to achieve the equipment's compactness, the inner packing radius should be as small as possible. However, a small inner packing radius may cause a large pressure drop because of the space occupied by the liquid distribution. In addition, the liquid

phase may be taken away by the gas flow with a large radial velocity resulting from the small cross-sectional flow area, and the ratio of the liquid to gas kinetic energy should be above three [197]. Therefore, the kinetic energy of the exit gas should be in the same order of magnitude as that of the liquid jet's kinetic energy. The inner packing radius is given as follows [197]:

$$r_i = \left(\frac{Q_G}{\pi v_{jet}(1 - f_d)} \right)^{0.5} \left(\frac{\rho_G p}{\rho_L} \right) \quad (6 - 1)$$

where Q_G is the gas flow rate, ρ_G and ρ_L are the density of the gas and liquid phases, respectively, f_d is fraction of the space of the inner cavity zone occupied by the liquid distributor, which is recommended as 0.33 [197], p is the kinetic energy ratio of the liquid jet to the exit gas, which is recommended as 2 [197], and v_{jet} the liquid jet velocity, which is set as around 2 m/s in this study. After calculation, it is found that r_i is 0.03 m.

6.2.2 Packing width

When the gas phase flows into the inner packing area, where the flooding is most likely to occur, its radial gas superficial velocity is almost the highest. In order to prevent flooding, the packing width should be sufficiently wide. However, it cannot be excessively large, as this may lead to portions of the packing surfaces remaining unwetted near the top and bottom of the packing. To ensure optimal operation, the packing width should be selected in a manner that ensures process operation at design conditions remains just slightly below flooding, which is determined by the superficial gas velocity near flooding as follows [197]:

$$h = \frac{Q_G}{2\pi r_i U_G} \quad (6-2)$$

$$U_G = \left[\frac{130 N_g^{0.43} \alpha_S^{-0.93} (\rho_L - \rho_G)^{0.25}}{\rho_G^{0.5} + 1.51 \left(\frac{Q_L}{\varphi Q_G} \right)^{0.5} \rho_L^{0.5}} \right]^2 \quad (6-3)$$

where U_G is the superficial gas velocity near flooding, α is the RPB flooding correlation fitting parameter, which is set between 0.7 and 0.9, N_g is the ratio of the centrifugal to gravitational acceleration, α_S is the specific area of the packing, Q_L is the liquid flow rate, h is the packing width, and r_i is the inner packing radius obtained in last section. According to the operating conditions employed in the CPB experiments (Table 6-1), the packing thickness is 0.1 m.

6.2.3 Outer packing radius

As we know, the mass transfer between the gas and liquid phases mainly occurs in the packing region. If the outer packing radius is larger, the gas and liquid flows have more time and area to be in contact and react with each other, which results in a higher mass transfer performance. As a result, the outer packing radius is mainly determined by the desired CO₂ capture rate, and the equation for the outer packing radius is given as follows [161]:

$$r_o = \left[\frac{Q_G}{K_L a_e \pi h} \ln \left(\frac{y_{i,CO_2}}{y_{o,CO_2}} \right) + r_i^2 \right]^{0.5} \quad (6-4)$$

where r_o is the outer packing radius, $K_L a_e$ is the overall volumetric mass transfer rate, and y_{i,CO_2} and y_{o,CO_2} are the CO₂ mole fraction in the gas inlet and outlet, respectively. In this case, the desired CO₂ capture rate is 90.8% (the CO₂ capture rate in the CPB

experiment), thus, the ratio of y_{o,CO_2} to y_{i,CO_2} is 10.87. In addition, $K_L a_e$ is difficult to accurately determine since its value is related to the unknown packing outer radius. In the work of Agarwal et al. [197], the semi-empirical correlations of the mass transfer rate have been utilized to calculate $K_L a_e$. However, these correlations are derived from various packings and systems, and they may not be able to accurately predict $K_L a_e$ for the amine-based absorption system. In the last chapter, a pilot-scale RPB model with an outer packing diameter of 0.3 m has been developed, and $K_L a_e$ can be estimated by using this RPB model under the same operating conditions as the CPB and the lowest employed rotational speed of 300 rpm in this case. Based on the pilot-scale RPB, $K_L a_e$ is 1.26 s^{-1} . Therefore, the outer packing radius is calculated to be 0.6 m.

6.2.4 Other parameters

The liquid jet velocity is recommended as 2 m/s [197] when determining the inner packing radius. In order to make the liquid evenly jet from the liquid nozzle in the axial directly, the number of the liquid nozzle is one and the shape of the liquid nozzle is rectangular with the size being $0.001 \times 0.1 \text{ m}$.

In addition, the packing type could also influence the CO_2 capture performance. For the RPB, the wire mesh and metal foam are the most commonly used packing types due to its higher porosity and low frictional pressure drop. Considering the metal foam being cost expensive, the wire mesh packing with porosity and specific surface area of 0.801 and $663 \text{ m}^2/\text{m}^3$, respectively, is selected, which has been used in the last chapter.

Overall, the main information of the RPB model is shown in Table 6-2.

Table 6-2 The information of the large-scale RPB model.

D_i (m)	h (m)	D_o (m)	Liquid distributor (m)	Packing type	Porosity	Specific area of packing (m^2/m^3)
0.06	0.1	1.2	0.001×0.1	Wire mesh	0.801	663

6.3 CFD modelling

6.3.1 Geometry of the RPB

Based on designed RPB size presented in Table 6-2, a large-scale RPB model can be established. Because the heights of the liquid distributor and the packing are the same, which means the layout of the designed 3D RPB remains identical in the axial direction, including the gas and liquid inlets and the gas outlet. Therefore, the 3D RPB may be simplified into a 2D RPB model to save the computing resources, which is shown in Figure 6-1. Therefore, this 2D model is used to investigate the CO₂ capture performance in the study.

In this model, the liquid nozzles are located in the center of the packing. Because the length of the liquid distributor is the same as the packing height, the liquid could be distributed evenly in the axial direction. Since the gas inlet and liquid outlet cannot overlap outside the packing, an elimination zone is built with an extension outside the packing in order to remove the liquid phase but retain the gas phase. In order to save the mesh grids, the extension cannot be too long, and an elimination zone with a radial length of 0.05 m is established. The appropriate source equations for this zone can be found in Section 3.2. The gas inlet is set on the outer boundary of the elimination zone and the gas is assumed to enter uniformly in the circumferential directions. Since the gas flow almost rotates in sync with the packing near the outer packing, the gas inlet

boundary is set at the same rotational speed as the packing.

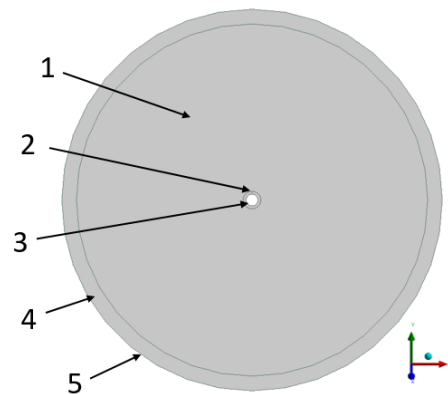


Figure 6-1 Schematic diagram of the 2D RPB ((1, packing; 2, liquid inlet; 3, gas inlet; 4, liquid elimination zone; 5, gas outlet).

6.3.2 Assumptions for the model

The main assumptions of the RPB model are as follows:

- (i) The wire mesh packed bed is a homogenous porous medium.
- (ii) The gas is incompressible.
- (iii) The pressure field is shared between the gas and liquid phases.
- (iv) The liquid phase exists in the form of the film and droplets within the packing zone.
- (v) The mass transfer occurs in the packing zone only.

6.3.3 Solution procedure

The 2D transient simulations were conducted using ANSYS Fluent 2021 R1 with double precision mode on the High Performance Computing cluster at the University of Sheffield. The governing equations of the mass, momentum, energy and species were

solved to investigate the hydrodynamics, thermodynamics and mass transfer in the RPB. The UDF was developed to define the properties of the MEA solution, apply additional forces in the momentum equations, and calculate the transferred CO₂ in the mass equations. The equilibrium thermal model was selected to calculate the heat transfer between the fluid and solid phases in the porous medium zone. The Phase Coupled SIMPLE method was employed and the pressure equations were discretized using a second-order scheme. The pressure-based method and the absolute velocity formulation were also utilized. A time step of 4×10^{-4} s was set and a maximum of 35 iterations per time step were used with a convergence tolerance of 5×10^{-5} . The simulation was considered to reach pseudo steady-state when the CO₂ concentration at the gas outlet and the liquid outlet temperature differed by less than 1% within ten seconds, and the residuals of the energy equation and other governing equations were below 5×10^{-7} and 1×10^{-4} , respectively.

For the RPB model, the realizable $k - \varepsilon$ turbulence model has been frequently used [33, 90, 177] and the advantages of using this model are illustrated in Section 4.2.2, thus, this model has been employed in the section.

6.3.4 Boundary conditions

The gas phase comprises 9.9% CO₂ and 90.1% air. It is assumed that the gas phase consists only of CO₂, N₂, and O₂, and the component mole fractions are detailed in Table 6-3. The liquid phase contains CO₂, MEA (HOC₂H₄NH₂), MEAH⁺ (HOC₂H₄NH₃⁺), MEACOO⁻ (HOC₂H₄NHCOO⁻) and water. Similar to the CPB experiments, all MEA solutions were preloaded (0.204 mol CO₂/mol MEA) before the MEA solution was fed into the RPB and the mass fraction of each species in the 30%

MEA solution is presented in Table 6-4. The correlations of the surface tension and viscosity for the MEA solution can be found in Table 5-4 [185, 186]. In addition, the liquid density, thermal conductivity and specific heat of the two phases are evaluated by the mixing law based on every species in each phase.

Table 6-3 The mole fraction of each component in the gas phase.

CO ₂	N ₂	O ₂
0.099	0.7118	0.1892

Table 6-4 Mass fraction of the each components in the 30% MEA solutions.

MEA (C ₂ H ₇ ON)	MEAH ⁺ (C ₂ H ₈ ON ⁺)	MEACOOH ⁻ (C ₃ H ₆ O ₃ N ⁻)	H ₂ O
0.1698	0.0596	0.1002	0.6704

According to the experimental parameters [196], the gas flow rate is maintained at 210 m³/h with a fixed temperature of 40 °C at the gas inlet. The inlet CO₂ concentration is 9.9%. The gas outlet boundary is set as the pressure-outlet condition with a zero gauge pressure. The liquid is introduced with a fixed velocity of 2.0 m/s and a temperature of 40 °C and the liquid disappears after entering the liquid elimination zone. The species and their concentrations in the gas and liquid phases are presented in Table 6-3 and Table 6-4, respectively. The gravitational force acts in the negative Y direction with a gravitational acceleration of magnitude of 9.8 m/s⁻², indicating a vertically oriented RPB. The material of the packing is steel with specific area and porosity values of 663 m²/m³ and 0.801, respectively. Rotational speeds ranging from 300-800 rpm are utilized in the simulations, with the sliding model employed to replicate the motion of the packing. The conditions on the wall boundaries are defined as adiabatic.

6.3.5 Grid independence

The ANSYS Mesh was employed to generate the grid of the large-scale RPB model. The hexahedral mesh elements formed the 2D computational grid. In order to get a mesh independence solution, various cases with different mesh numbers ranging from 0.05 M to 0.18 M were tested. Finally, the outlet CO₂ mole fraction reaches stability until the mesh number was 0.15 M, see Figure 6-2(a). The packing region was evenly divided into 720, 180 parts in the circumferential, radial directions, respectively, which is shown in Figure 6-2(b).

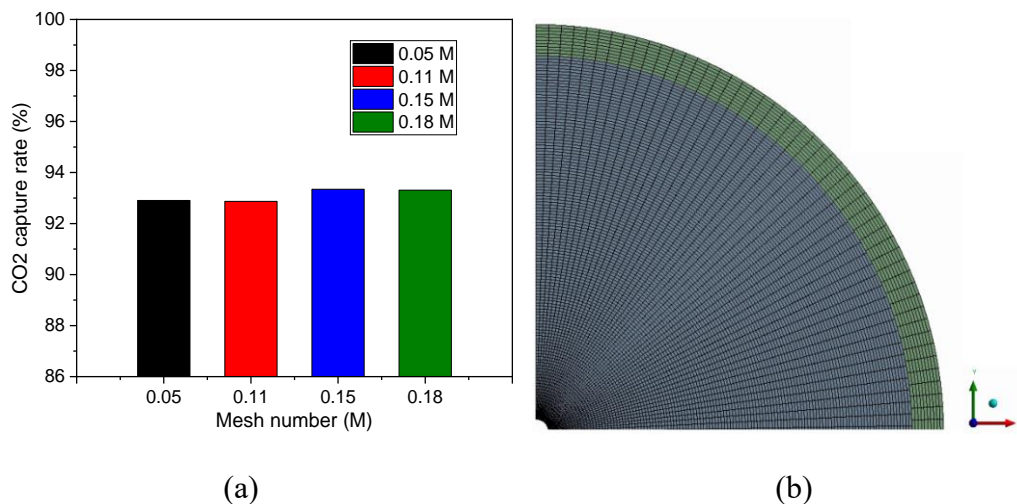


Figure 6-2 (a) The predicted CO₂ capture rate with different grids, and (b) schematic of the mesh in the 2D model.

6.4 Results and discussion

In this section, the CO₂ capture processes, including the hydrodynamics, thermodynamics and mass transfer, have been analyzed in the established large-scale RPB using the operating conditions from the CPB experiments. Subsequently, the process optimization of the operating parameters, including the liquid flow rate, MEA

concentration, etc., has been investigated. The obtained simulation results have been quantitatively compared with the CPB experimental data.

For evaluating the CO₂ capture performance in the RPB, the CO₂ capture rate is introduced as follows:

$$r_{CO_2} = \frac{y_{i,CO_2} - y_{o,CO_2}}{y_{i,CO_2}} \times 100\% \quad (6 - 5)$$

Where r_{CO_2} is the CO₂ capture rate, and y_{in,CO_2} and y_{out,CO_2} are the CO₂ mole fractions at the inlet and outlet, respectively.

6.4.1 Comparison between the CPB and RPB with various rotational speeds

In order to investigate the effect of the rotational speed and compare the CPB and RPB, the CO₂ capture processes in the RPB were simulated under the same operating conditions as the CPB experiments except for the rotational speed. The rotational speed employed in this work ranged from 300 to 800 rpm.

Figure 6-3 shows the CO₂ capture rate and liquid outlet temperature under various rotational speeds. Taking the 300 and 800 rpm as an example, Figures 6-4 (a-f) present the distribution of the liquid holdup, effective interfacial area, CO₂ fraction in the gas phase, MEA mass fraction, liquid specific heat, and liquid temperature, respectively. Figure 6-3 reveals that the CO₂ capture performance improves while the liquid outlet temperature decreases with the increase in the rotational speed. As the rotational speed increases, the liquid holdup decreases due to the larger centrifugal force, as shown in Figure 6-4(a). Furthermore, stronger interaction between the liquid phase and packing

leads to the formation of more tiny liquid droplets and thin liquid films, thus leading to a slightly higher effective interfacial area, which is shown in Figure 6-4(b). As a result, the CO₂ and MEA solution have more chance to react for 800 rpm, thus enhancing the CO₂ capture performance, see Figures 6-3(a) and 6-4(c). Since the mass transfer area in the outer packing region is large and most of the CO₂ is captured in this region at 800 rpm, the MEA mass fraction experiences a significant reduction in the outer packing region, as shown in Figure 6-3(d). In addition, in theory, a higher degree of reaction would result in greater heat release in the liquid phase, and as a consequence, the liquid temperature should be higher at 800 rpm. However, a lower liquid temperature could be observed in Figure 6-3(f). This is because with a higher product concentration (MEAH⁺ and MEACOOH⁻), the specific heat of the liquid phase for 800 rpm is higher than that for 300 rpm (Figure 6-3(e)), which means more energy is required to raise the temperature by one degree at 800 rpm.

In Section 6.2, the desired CO₂ capture rate (90.8%) and the $K_L a_e$ obtained in the pilot-scale RPB under 300 rpm were used to determine the outer packing diameter, with the expectation that the CO₂ capture rate in the large-scale RPB should be 90.8% when using 300 rpm. However, according to Figure 6-3, the predicted CO₂ capture rate is found to be lower than 90.8%, indicating a lower $K_L a_e$ in the large-scale RPB. This can be attributed to the smaller local liquid holdup in the outer packing region, which results in less MEA molecules being available. Another important reason is that the interaction between the liquid and packing becomes weaker as the liquid starts to synchronize with the rotating packing in the bulk of the packing, particularly in a large-scale RPB. Therefore, the effective interfacial area becomes smaller and the surface renewal

frequency becomes lower, leading to a decrease in mass transfer rate along the radial direction in the packing region.

Based on the results shown in Figure 6-3, it can be observed that when the rotational speed is higher than 600 rpm, the CO₂ capture performance in the RPB is significantly superior to that in the CPB, which has a capture rate of 90.8%. In order to reduce the sensible heat of the regeneration process, which is directly proportional to the liquid flow rate, it is essential to optimize the process parameters while maintaining the CO₂ capture rate above 90.8%. On the other hand, when the rotational speed remains at 500 rpm or below, the CO₂ capture rate in the RPB is only slightly higher or even lower than that in the CPB. To enhance the CO₂ capture performance in RPBs, increasing the MEA concentration can be considered a promising strategy, which may also allow for a reduction in the liquid flow rate. Therefore, using the RPB with the appropriate operation parameters can provide a more energy-efficient solution for CO₂ capture.

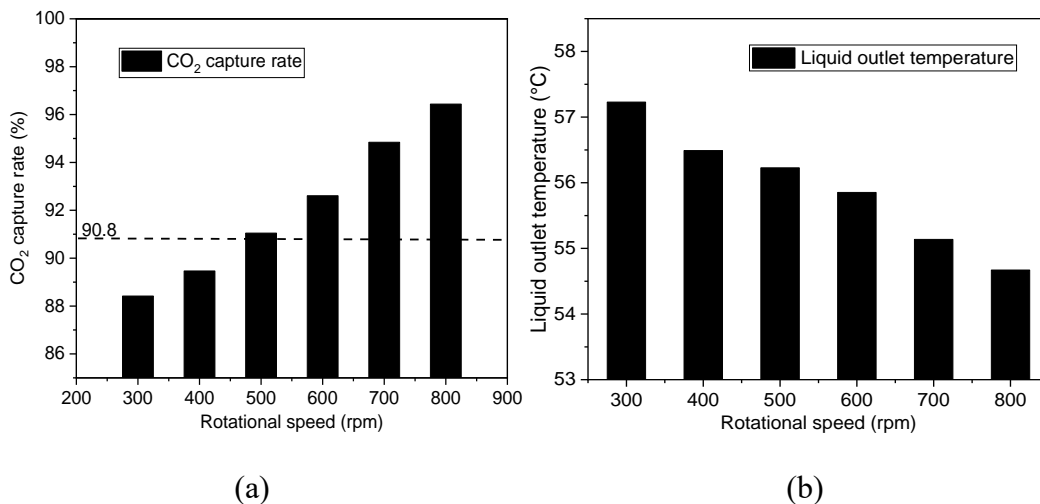


Figure 6-3 The (a) CO₂ capture rate and (b) liquid outlet temperature under various rotational speeds.

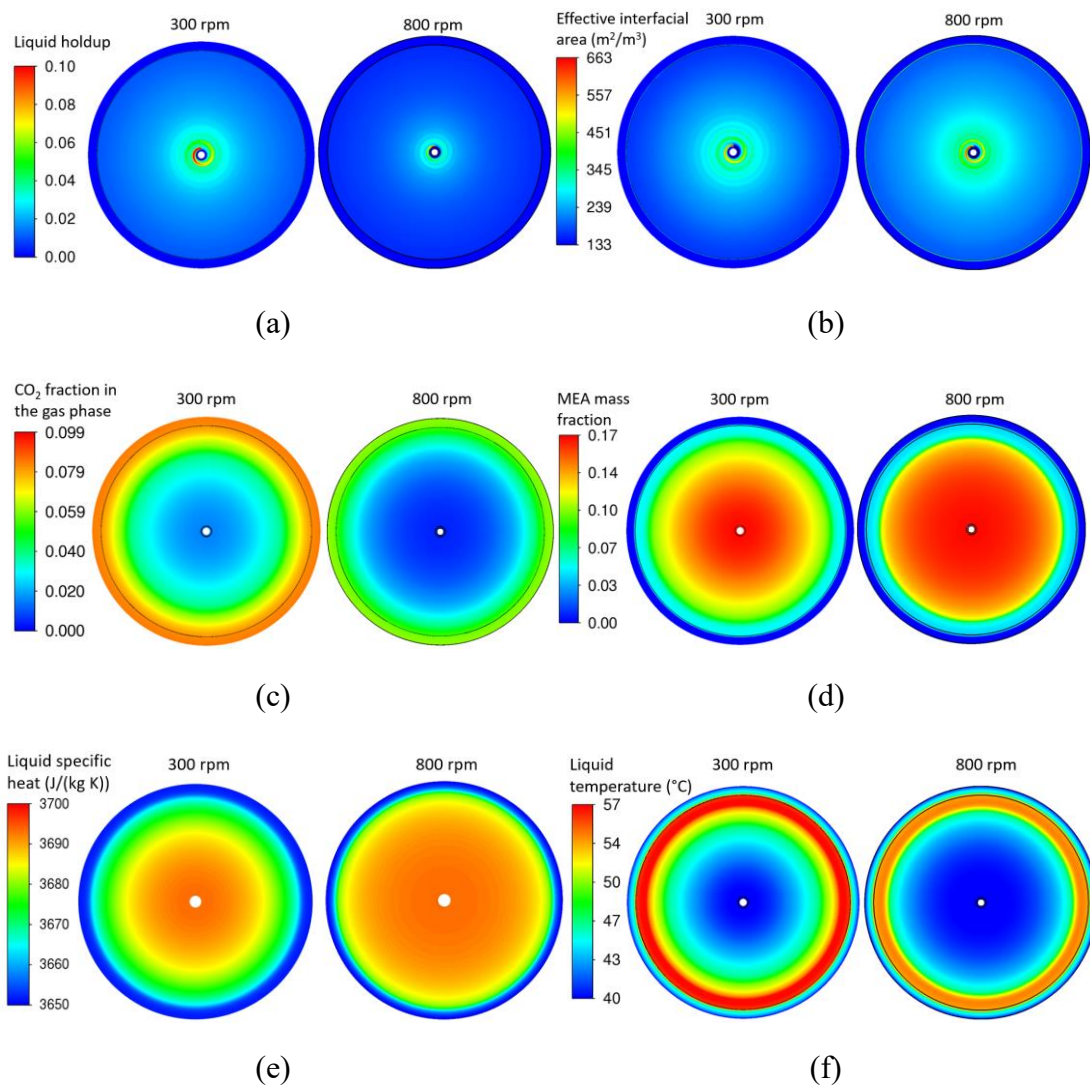


Figure 6-4 The distributions of the (a) liquid holdup; (b) effective interfacial area; (c) CO_2 fraction in the gas phase; (d) MEA mass fraction; (e) liquid specific heat; and (f) liquid temperature for 300 and 800 rpm.

6.4.2 Comparison between the CPB and RPB under various flow rates

Figure 6-5 illustrates the CO_2 capture performance and liquid outlet temperature under various rotational speeds and liquid ratios (the ratio of the liquid flow rate employed in the RPB model over the liquid flow rate used in the CPB experiment). According to Figure 6-5(a), an increase in the liquid flow rate ratio from 0.6 to 0.8 leads to a

significant rise in both CO₂ capture rate and liquid outlet temperature. This is attributed to the generation of a higher effective interfacial area, resulting from an increased number of tiny droplets as the liquid ratio rises. In addition, a larger amount of free MEA molecules becomes available with higher liquid flow rates, enhancing the capacity to capture CO₂. An increase in the reaction rate results in higher reaction heat. Consequently, this leads to an increase in the liquid outlet temperature, as demonstrated in Figure 6-5(b). In turn, the elevated liquid temperature positively influences the reaction rate.

However, it is worth noting that when comparing liquid ratios of 0.6 and 0.7 across various rotational speeds, the CO₂ capture rates appear to be similar. This observation could be attributed to the fact that nearly all the MEA molecules in the liquid phase have already reacted with the CO₂. According to previous reports, the absorbing capacity of MEA is 0.565 CO₂ mole/mole MEA (equivalent to 407 g CO₂/kg MEA) [198]. In this case study, if the CO₂ could be fully absorbed by the MEA solution with 0.565 CO₂ mole/mole MEA loading, the liquid flow rate ratio should be at least 0.78. It suggests that the MEA solution has already reached its maximum capacity for CO₂ absorption for the liquid flow rate ratio being 0.6 and 0.7, and the rotation speed has little effect on the CO₂ capture rate. Taking the rotational speed of 600 rpm as an example, Figure 6-6 shows the MEA molecules in the liquid phase when the liquid flow rate ratios are 0.6, 0.7, 0.9. From Figures 7(a) and 7(b), it can be observed that for the liquid flow rate ratios being 0.6 and 0.7, the MEA fraction is close to zero at the outer or even the middle packing region. Therefore, it is important to optimize the operation parameters of the RPB to ensure a sufficient amount of MEA while minimizing the

liquid flow rate.

It can be also found that when the liquid flow rate ratio is no less than 0.8, the CO₂ capture rate reaches a steady state (refer to Figure 6-5(a)). This is because when the liquid ratio increases from 0.8 to 1.0, a larger contact area could be generated and more MEA molecules are available. However, the increase in the mass transfer area is limited at a higher range of the liquid flow rate and rotational speed, and this phenomenon is consistent with the findings of previous experimental studies [39, 191, 199]. Furthermore, when the liquid flow rate ratio exceeds 0.8, the available MEA molecules are sufficient to capture the most CO₂, resulting in a similar CO₂ capture rate. Therefore, further increases in the liquid flow rate ratio do not result in significant improvements in CO₂ capture rate. And the RPB can achieve a higher CO₂ capture rate than the CPB when the rotational speed is higher than 600 rpm, allowing a 20% reduction in the liquid flow rate.

From Figure 6-5(b), it is noted that the liquid outlet temperature decreases as the liquid flow rate ratio increases from 0.8 to 1.0. Within this range, the CO₂ capture rate remains consistent, indicating a similar amount of released reaction heat. However, the reduction in liquid temperature can be attributed to the significant sensible heat of the liquid phase as the liquid flow rate ratio increases. Also, this decrease in the liquid outlet temperature has been observed in the experimental study [161] and Section 5.3.3.2. In turn, the decreased liquid temperature may be another reason for the steady CO₂ capture rate observed in Figure 6-5(a).

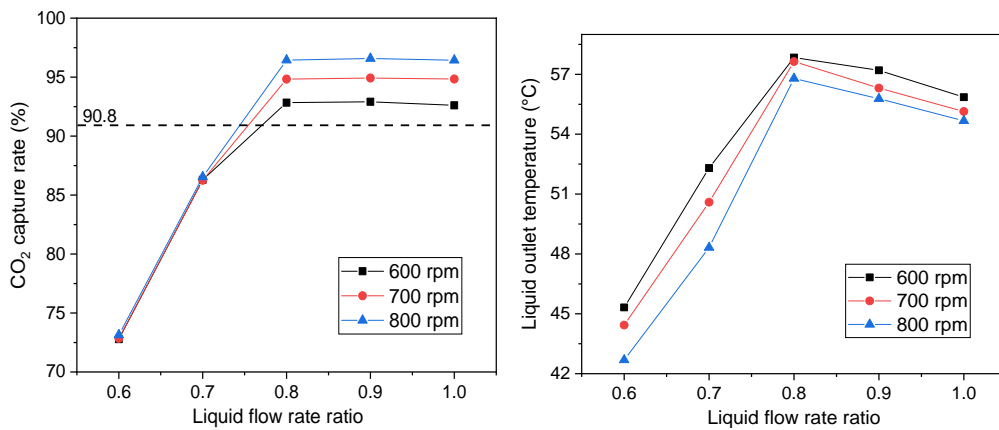


Figure 6-5 The (a) CO₂ capture rate and (b) liquid outlet temperature under various rotational speeds and liquid flow rates.

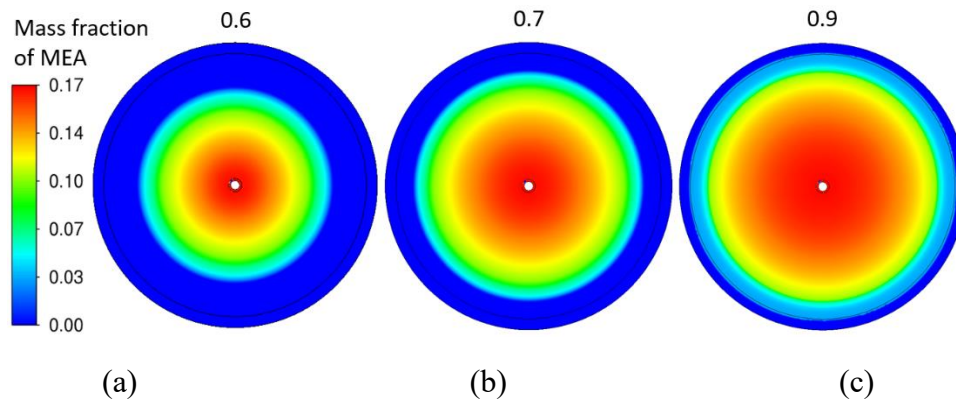


Figure 6-6 The MEA fraction in the liquid phase when the liquid flow rate ratios are (a) 0.6; (b) 0.7; and (c) 0.9 for 600 rpm.

6.4.3 Comparison between the CPB and RPB under various MEA concentrations

Increasing the MEA concentration could improve the absorption performance and reduce the liquid flow rate, and subsequently save the regeneration power energy. Figure 6-7 shows the CO₂ capture rate under lower rotational speeds and higher MEA concentrations. In Figure 6-7, it can be observed that the CO₂ capture rate gradually

increases as the MEA concentration increases, owing to the availability of more free MEA molecules. In addition, the liquid viscosity will increase as the MEA concentration increase, leading to an increase in the residence time, which favors for the CO₂ absorption. Also, higher MEA concentration generates more reaction heat, leading to a higher liquid temperature that enhances the chemical reaction rate. Therefore, by optimizing the MEA concentration, it is possible to reduce the liquid flow rate while maintaining similar CO₂ capture performance.

As an example, taking the rotational speed of 300 rpm, Figure 6-8 displays the CO₂ capture performance under different MEA concentrations and liquid ratios. For the highest MEA concentration of 50%, the CO₂ capture rate in the RPB is higher than that in the CPB, as long as the liquid ratio is higher than 0.6. Remarkably, the liquid flow rate can be decreased by 40% compared to the CPB experimental data when using a 50 % MEA solution, even under the lowest rotational speed. These results indicate that optimizing the operating conditions such as MEA concentration and liquid flow rate can significantly save the liquid flow rate required by the RPBs and further reduce the regeneration energy in the CO₂ capture plant.

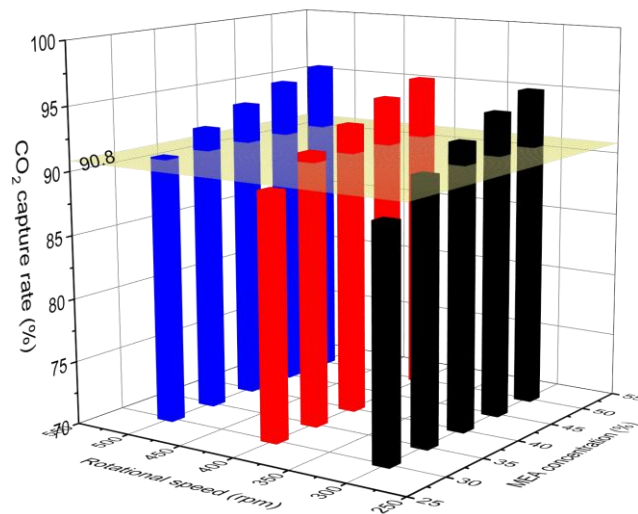


Figure 6-7 The CO₂ capture rate under various rotational speeds and MEA concentrations.

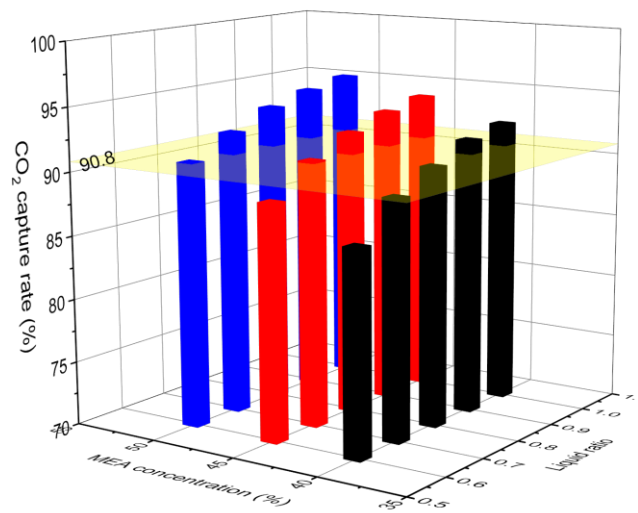


Figure 6-8 The CO₂ capture rate under various MEA concentrations and liquid ratios for 300 rpm.

6.5 Comments on the use of the RPB for post-combustion CO₂ capture

In this case study, a large-scale RPB with an outer packing diameter of 1.2 m has been

established and its volume is only 20% compared with the CPB's volume. Due to the high gravitational environment in the RPB (rotational speed higher than 600 rpm), the liquid flow rate could be reduced by 20% without sacrificing the CO₂ capture performance, which may further reduce the regeneration power consumption. Even under the lowest employed rotational speed (300 rpm), the liquid flow rate could be saved 40% if using a higher MEA concentration. Overall, the study shows that the RPB has advantages over the traditional CPB for CO₂ capture in terms of reducing the required liquid flow rate, increasing the CO₂ capture rate, and decreasing the unit size.

6.6 Conclusions

A large-scale RPB model has been established by employing the Eulerian porous medium method coupled with various sub-models. The hydrodynamics, thermodynamics and reaction-enhanced mass transfer have been investigated and process optimization of the CO₂ capture in this RPB has been quantitatively explored. The main findings of this work are as follows: (i) a 2D large-scale RPB model with the outer packing diameter of 1.2 m was established according to the design procedure. This is the first time that an investigation has been performed of the CO₂ capture processes in such a large RPB model by using the CFD method; (ii) the Eulerian porous medium approach has been employed in the large-scale RPB. It has been shown that it is feasible and effective to study the carbon capture in this large-scale RPB through utilizing the Eulerian porous medium modelling method since the required computational resources could be significantly saved. Thus the present new method is computationally accurate and efficient; (iii) coupled with the sub-models, the hydrodynamics, thermodynamics and mass transfer processes could be thoroughly and

accurately analyzed and the process optimization of the CO₂ capture process could be conducted.

The simulation results show that although the CO₂ capture rate for 800 rpm is larger than that for 300 rpm, the liquid outlet temperature for 300 rpm is higher due to the smaller heat transfer between the phases and specific heat. When using a higher rotational speed (over 600 rpm), the liquid flow rate could be reduced by 20% while keeping the CO₂ capture rate higher than that in the CPB. Even under the lowest employed rotational speed, the liquid flow rate could be reduced by 40% when using the MEA solution with 50% concentration compared with that employed in the CPB experiment. Furthermore, under the same carbon capture rate, the required volume of the packing in RPB is only 20% compared with the packing volume in the CPB.

In conclusion, this new and important investigation not only demonstrates the feasibility and effectiveness of using the CFD method to study such large-scale RPB model, but also shows the potential for the RPB to be industrially employed for PCC. There are two limitations of the CFD model proposed in this study. The first is that the model is limited to a 2D RPB geometry, and the design optimization of the liquid distribution on the CO₂ capture cannot be studied. Secondly, only the CO₂ capture performance and required liquid flow rate in the RPB reactor has been explored, and the regeneration consumption associated with the use of the RPB is not considered in this section.

CHAPTER 7: CONCLUSIONS AND FUTURE WORK

The RPB has shown much potential for post-combustion carbon capture due to the high mass transfer performance and the small area occupied. The detailed CO₂ capture processes within the RPB have been effectively studied by employing the CFD approach. In this thesis, the flow characteristics (especially the liquid dispersion), thermodynamics and reaction-enhanced mass transfer have been thoroughly explored in the multi-scale RPBs. The findings and conclusions are outlined in Section 7.1, and possible avenues for future research are deliberated in Section 7.2.

7.1 Conclusions

7.1.1 Liquid dispersion in the RPB

Liquid dispersion is very important for the modelling of liquid flow in a RPB when the Eulerian porous medium approach is employed. For investigating the effect of the liquid dispersion in a practical RPB, a 3D Eulerian porous medium model has been established in Chapter 4 coupled with the appropriate interfacial, drag and dispersion forces formulations. The main important findings are as follows: (i) the porous medium model with the Eulerian method has been successfully developed and used to accurately and efficiently model the fluid dynamics and liquid dispersion in a 3D RPB. Using this model can substantially reduce the computational time and efforts; (ii) a new form of

the porous resistance model has been developed for two-phase flows and this model could accurately predict the porous resistance in the packing; (iii) the correlation for the gas-liquid effective interfacial area has been developed to fit the non-uniform flow. After the modification, the distribution of the fractional effective interfacial area (f_e) is consistent with the reality. The effective interfacial area is larger where the liquid holdup is higher. In addition, the use of the developed f_e would make the porous medium model more accurate; and (iv) the dispersion force models, for the first time, are added into the model to accurately and efficiently simulate the liquid dispersion in a complete packing region in 3D. In the 3D model coupled with the dispersion force models, the effect of liquid dispersion on the liquid holdup could be quantified and more accurate liquid flow performance was achieved.

In addition, the simulation results show that the effect of the capillary pressure and mechanical dispersion forces on the liquid holdup are important to consider but showed different levels of significance with different liquid nozzle lengths. The effect of the capillary pressure force and mechanical dispersion force on the liquid holdup are similar when the nozzle length is larger. While when the nozzle length is smaller, the liquid dispersion in this RPB model is dominated by the mechanical dispersion and the spread factor is a very sensitive quantity. With the liquid flow rate increasing, the influence of the dispersion force on the liquid holdup is different under different rotational speeds. The effect of the dispersion force on the liquid holdup is almost the same with different nozzle widths and packing porosity. In addition, increasing the number of liquid nozzles from 1 to 4 could improve the liquid distribution and liquid holdup in the packing region substantially. However, further increasing the number of

nozzles tends to be less effective. In general, it takes only 0.5-3 h depending on the rotational speed simulated to finish a full analysis of the 3D RPB by using the Eulerian porous medium method. Overall, the new method proposed and employed in this thesis paves the way for much more efficient simulations of full 3D RPBs in the future.

7.1.2 CO₂ capture processes in the RPB

RPB technology shows great potential for post-combustion capture. However, the capture process inside the full RPB is difficult to simulate and this is due to the complexity of the CO₂ capture process in the outer cavity zone. Therefore, in Chapter 5, a new 3D CFD model, including the packing and the inner and outer cavity zones, has been established by employing the Eulerian porous medium method coupled with various sub-models, such as the models of the interfacial force, drag force, dispersion forces, effective interfacial area, heat transfer, and mass transfer. The CO₂ capture performance both in the packing and in the outer cavity zones has been quantitatively analyzed under different operating conditions.

The simulation results show that (i) a new completed 3D Eulerian porous medium RPB model has been established based on a pilot scale RPB model. By using the Eulerian porous medium modelling method, the CO₂ absorption performance within a whole RPB could be effectively investigated due to the significantly reduced computational cost; (ii) the force, effective interfacial area, heat transfer, mass transfer models have been coupled with the Eulerian RPB model, thus, the hydrodynamics, thermodynamics and mass transfer processes could be thoroughly analyzed; (iii) the effective interfacial area, force and even liquid droplet diameter models have been introduced separately for the packing region and the outer cavity zone for predicting the CO₂ capture

performance inside the whole RPB, and the CO₂ absorption processes in these zones are quantitatively evaluated under various operating conditions by the new CFD method for the first time.

The predicted simulation results are in good agreement with the experimental data by comparing the CO₂ fraction in the gas outlet and liquid outlet temperature. In addition, the end-effect zone is observed near the inner packing region where a large effective interfacial area occurs due to the liquid dispersion and strong interaction between the liquid and packing. However, the amount of the CO₂ transferred between the phases is small in the end-effect zone due to the small mass transfer area and local CO₂ fraction in the gas phase as well as the low liquid temperature.

The outer cavity zone has an effect on CO₂ capture inside the RPB. The contributions of the outer cavity zone to the mass transfer area and CO₂ capture are respectively in the ranges of 25%~40% and 28%~42% in the investigated RPB as presented in Chapter 5. These values may be different for different designs. Also, the simulation results show that the CO₂ captured in the outer cavity zone becomes more as the MEA concentration increases, however, the MEA concentrations have little effect on the ratio of the mass transfer area in the outer cavity zone to the whole RPB. The contributions of the outer cavity zone to the mass transfer area and CO₂ capture change slightly with the L/G ratio increasing. With the increase in the rotational speed, the ratio of the mass transfer area in the outer cavity zone to the whole RPB increases, however, the ratio of the CO₂ capture in the outer cavity zone to the whole RPB first decreases slightly and then increases significantly because the micromixing performance in the packing region improves significantly at the lower rotational speed. Overall, the new developed RPB

model can successfully and effectively predict the CO₂ capture process in the whole RPB, and this demonstrates the substantial potential of the model, with further validation, to be used for process optimization and design of the large-scale RPB for industrial PCC.

7.1.3 Comparison between the RPB and CPB for PCC

The RPB has been utilized in many industries, however, it has been rarely employed commercially for carbon capture due to a lack of understanding of how to operate a carbon capture plant with a large-scale RPB and the advantages over CPBs. Thus, a large-scale RPB with the outer packing diameter of 1.2 m has been computationally established in Chapter 6 according to the experimental parameters from a CPB pilot plant in order to compare with the CPB. The Eulerian porous medium method and various sub-models have been employed in order to effectively and extensively investigate the CO₂ capture processes, including the hydrodynamics, thermodynamics and mass transfer in the RPB. In addition, the CO₂ capture performance has been quantitatively compared in the RPB and CPB under different operation conditions.

The simulation results show that the CO₂ capture rate increases, but the liquid temperature decreases with the increase in the rotational speed due to the higher liquid specific heat and larger gas-liquid heat transfer resulting from the smaller liquid droplet diameter. At rotational speeds exceeding 600 rpm, the liquid flow rate could be decreased by 20% compared to that used in the CPB, all while maintaining a higher CO₂ capture rate than what is achieved in the CPB. Even under the lowest employed rotational speed of 300 rpm, the liquid flow rate could be reduced by 40% when using the MEA solution with 50% concentration. In addition, under the same carbon capture

rate, the required volume of the packing in the RPB is only 20% when compared with the packing volume in the CPB. In conclusion, this new and important investigation not only demonstrates the feasibility and effectiveness of using the CFD method to study such large-scale RPB model, but also shows the advantages for the RPB to be industrially employed for PCC.

7.1.4 Overall conclusion

In order to pave the way for the RPB deployment for PCC, this thesis proposes a new and important approach for effectively modelling the complete CO₂ capture processes in the multiscale and multiphase flows in the RPB using the Eulerian porous medium approach.

In this thesis, the dispersion force models, including the capillary pressure and mechanical dispersion force models, have been developed in order to explore the effect of the liquid dispersion. Various sub-models have been employed along with the Eulerian method for effectively analyzing the CO₂ capture processes, including the hydrodynamics, thermodynamics, and mass transfer, within a RPB. In specific, the effective interfacial area and the forces acting on the phases are separately introduced for the packing and the outer cavity zones. Also, based on the experimental data from a pilot plant using CPB, an important large-scale RPB has been established and operated under different conditions in order to quantitatively compare the CPB and RPB and provide useful information for the operation of the industrial RPB.

It is shown that the use of the Eulerian porous medium approach could significantly save the computational resources and simulation time. Clearly, the dispersion force

could influence the liquid holdup within the RPB and the mechanical dispersion force is more sensitive to the length of the liquid nozzle when compared with the capillary pressure force. In addition, the operating and design parameters could affect the liquid dispersion. For instance, the liquid distribution and liquid holdup in the packing region could improve with the number of liquid nozzles increasing from 1 to 4. However, further increasing the number of nozzles tends to be less effective. The CO₂ capture inside the whole RPB model has been comprehensively predicted, and the end-effect zone is observed near the inner packing region. However, the captured CO₂ is small in this zone due to the small mass transfer area and local CO₂ fraction in the gas phase as well as the low liquid temperature. The contribution of the outer cavity zone to the CO₂ capture is in the ranges of 28%~42% in the investigated RPB and these values may be dependent on the RPB sizes and designs. The effect of the operating parameters on the CO₂ capture in the packing and outer cavity zone have been examined. For example, the simulation results show that the CO₂ captured in the outer cavity zone increases as the MEA concentration increases, however, the MEA concentrations have little effect on the ratio of the mass transfer area in the outer cavity zone to the whole RPB. Also, the CO₂ capture processes have been investigated in a large-scale RPB with an outer packing diameter of 1.2 m and this has been compared with the CPB. The results show that when using a higher MEA concentration solution (50%), the liquid flow rate could be reduced by 40% even under the lowest employed rotational speed compare with that used in the CPB. Also, the packing volume in the RPB is only 20% of that in the CPB, which could substantially reduce the capital cost and the area occupied.

In conclusion, the main contributions of this thesis include: (i) the proposed new and

important method effectively models the liquid dispersion in the 3D RPBs. This could pave the way for modelling the industrial RPB model for PCC; (ii) various sub-models have been separately developed for thoroughly analyzing the physical and chemical processes in the packing and outer cavity zone, and this could accurately predict the CO₂ capture performance; (iii) the process optimization of a large-scale RPB is performed and the quantitative comparison between the CPB and RPB is conducted, which would provide some valuable guidance for commercial application and operation of RPBs.

7.2 Future work

(i) This thesis mainly focuses on the CO₂ capture processes using the RPB, and the regeneration process has not been considered. As a result, the energy consumption for the solution regeneration cannot be obtained. In order to better understand the RPB for CO₂ capture process and compare with the CPB, the regeneration process should be considered in the future work.

(ii) Due to the strong centrifugal force, the MEA solutions with a higher concentration can fluently pass through the packing, which have been utilized in the RPB. Although the solution with a higher MEA concentration favors the CO₂ absorption, the greater trend for corrosion, degradation and foaming should be carefully considered before the PCC industrial application.

(iii) The accuracy of the RPB model is highly dependent on the applicability of the sub-models employed and therefore, careful validation of the model should be considered, especially when a very different packing is employed for the RPB.

(iv) The dynamic contact angle (β) in the the effective interfacial area model is determined by comparing the simulation results and the experimental data in this thesis. However, this parameter is related to the material texture of the packing surface, solution properties, rotational speed, etc. In order to obtain a more accurate prediction, this angle should be further investigated.

(v) Only the wire mesh packing is taken into consideration, and a porous resistance model customized for this particular type of packing is introduced in this thesis. However, other packing types, such as the foam packing, should be considered and the corresponding porous resistance models should be developed.

Reference

- [1] IPCC, *Climate Change 2014: Synthesis Report*. Tech. Rep., 2014.
- [2] Nadeau, K.C., I. Agache, M. Jutel, I. Annesi Maesano, M. Akdis, V. Sampath, G. D'Amato, L. Cecchi, C. Traidl-Hoffmann, and C.A. Akdis, *Climate change: A call to action for the united nations*. 2021, Wiley Online Library.
- [3] Wu, X., M.H. Wang, P.Z. Liao, J. Shen, and Y.G. Li, *Solvent-based post-combustion CO₂ capture for power plants: A critical review and perspective on dynamic modelling, system identification, process control and flexible operation*. *Applied Energy*, 2020. **257**.
- [4] Garba, M.U., *Prediction of ash deposition for biomass combustion and coal/biomass co-combustion*. 2012: University of Leeds.
- [5] *UK becomes first major economy to pass net zero emissions law*. 2019; Available from: <https://www.gov.uk/government/news/uk-becomes-first-major-economy-to-pass-net-zero-emissions-law>.
- [6] Lu, X., P. Xie, D.B. Ingham, L. Ma, and M. Pourkashanian, *Modelling of CO₂ absorption in a rotating packed bed using an Eulerian porous media approach*. *Chemical Engineering Science*, 2019. **199**: p. 302-318.
- [7] Lawal, A., M.H. Wang, P. Stephenson, and O. Obi, *Demonstrating full-scale post-combustion CO₂ capture for coal-fired power plants through dynamic modelling and simulation*. *Fuel*, 2012. **101**: p. 115-128.
- [8] Liao, P.Z., X. Wu, Y.G. Li, M.H. Wang, J. Shen, A. Lawal, and C.L. Xu, *Application of piece-wise linear system identification to solvent-based post-combustion carbon capture*. *Fuel*, 2018. **234**: p. 526-537.

- [9] Akinola, T.E., E. Oko, Y.L. Gu, H.L. Wei, and M.H. Wang, *Non-linear system identification of solvent-based post-combustion CO₂ capture process*. Fuel, 2019. **239**: p. 1213-1223.
- [10] Aromada, S.A. and L. Øi. *Simulation of improved absorption configurations for CO₂ capture*. in *Proceedings of the 56th Conference on Simulation and Modelling (SIMS 56), October, 7-9, 2015, Linköping University, Sweden*. 2015. Linköping University Electronic Press.
- [11] Schäffer, A., K. Brechtel, and G. Scheffknecht, *Comparative study on differently concentrated aqueous solutions of MEA and TETA for CO₂ capture from flue gases*. Fuel, 2012. **101**: p. 148-153.
- [12] Khan, A.A., G.N. Halder, and A.K. Saha, *Carbon dioxide capture characteristics from flue gas using aqueous 2-amino-2-methyl-1-propanol (AMP) and monoethanolamine (MEA) solutions in packed bed absorption and regeneration columns*. International Journal of Greenhouse Gas Control, 2015. **32**: p. 15-23.
- [13] Cortes Garcia, G.E., J. van der Schaaf, and A.A. Kiss, *A review on process intensification in HiGee distillation*. Journal of Chemical Technology & Biotechnology, 2017. **92**(6): p. 1136-1156.
- [14] Wang, Y., Y.B. Li, M.J. Su, G.W. Chu, B.C. Sun, and Y. Luo, *Liquid droplet dispersion in a rotating packed bed: Experimental and numerical studies*. Chemical Engineering Science, 2021. **240**: p. 116675.
- [15] Luo, Y., G.W. Chu, H.K. Zou, F. Wang, Y. Xiang, L. Shao, and J.F. Chen, *Mass transfer studies in a rotating packed bed with novel rotors: chemisorption of CO₂*.

- Industrial & Engineering Chemistry Research, 2012. **51**(26): p. 9164-9172.
- [16] Ouyang, Y., K.L. Tang, Y. Xiang, H.K. Zou, G.W. Chu, R.K. Agarwal, and J.F. Chen, *Evaluation of various turbulence models for numerical simulation of a multiphase system in a rotating packed bed*. Computers & Fluids, 2019. **194**: p. 104296.
- [17] Guo, T.Y., K.P. Cheng, L.X. Wen, R. Andersson, and J.F. Chen, *Three-dimensional simulation on liquid flow in a rotating packed bed reactor*. Industrial & Engineering Chemistry Research, 2017. **56**(28): p. 8169-8179.
- [18] Zhang, J.P., Y. Luo, G.W. Chu, L. Sang, Y. Liu, L.L. Zhang, and J.F. Chen, *A hydrophobic wire mesh for better liquid dispersion in air*. Chemical Engineering Science, 2017. **170**: p. 204-212.
- [19] Guo, T.Y., X. Shi, G.W. Chu, Y. Xiang, L.X. Wen, and J.F. Chen, *Computational fluid dynamics analysis of the micromixing efficiency in a rotating-packed-bed reactor*. Industrial & Engineering Chemistry Research, 2016. **55**(17): p. 4856-4866.
- [20] Liu, Y., Y. Luo, G. Chu, F. Larachi, H. Zou, and J. Chen, *Liquid microflow inside the packing of a rotating packed bed reactor: Computational, observational and experimental studies*. Chemical Engineering Journal, 2020. **386**: p. 121134.
- [21] Liu, Y., Y. Luo, G.W. Chu, J.Z. Luo, M. Arowo, and J.F. Chen, *3D numerical simulation of a rotating packed bed with structured stainless steel wire mesh packing*. Chemical Engineering Science, 2017. **170**: p. 365-377.
- [22] Guo, J., W. Jiao, G. Qi, Z. Yuan, and Y. Liu, *Applications of high-gravity technologies in gas purifications: A review*. Chinese Journal of Chemical Engineering, 2019. **27**(6): p. 1361-1373.

- [23] Joel, A.S., M.H. Wang, and C. Ramshaw, *Modelling and simulation of intensified absorber for post-combustion CO₂ capture using different mass transfer correlations*. Applied Thermal Engineering, 2015. **74**: p. 47-53.
- [24] Duan, X.F., Z.G. Yuan, Y.Z. Liu, H.T. Li, and W.Z. Jiao, *Numerical simulation and experimental study of the characteristics of packing feature size on liquid flow in a rotating packed bed*. Chinese Journal of Chemical Engineering, 2021. **34**: p. 22-31.
- [25] Ouyang, Y., S.W. Wang, Y. Xiang, Z.M. Zhao, J.X. Wang, and L. Shao, *CFD analyses of liquid flow characteristics in a rotor-stator reactor*. Chemical Engineering Research & Design, 2018. **134**: p. 186-197.
- [26] Ouyang, Y., H.K. Zou, X.Y. Gao, G.W. Chu, Y. Xiang, and J.F. Chen, *Computational fluid dynamics modeling of viscous liquid flow characteristics and end effect in rotating packed bed*. Chemical Engineering and Processing-Process Intensification, 2018. **123**: p. 185-194.
- [27] Shi, X., Y. Xiang, L.X. Wen, and J.F. Chen, *CFD analysis of liquid phase flow in a rotating packed bed reactor*. Chemical Engineering Journal, 2013. **228**: p. 1040-1049.
- [28] Xie, P., X. Lu, X. Yang, D. Ingham, L. Ma, and M. Pourkashanian, *Characteristics of liquid flow in a rotating packed bed for CO₂ capture: A CFD analysis*. Chemical Engineering Science, 2017. **172**: p. 216-229.
- [29] Yang, Y.C., Y. Xiang, G.W. Chu, H.K. Zou, B.C. Sun, M. Arowo, and J.F. Chen, *CFD modeling of gas-liquid mass transfer process in a rotating packed bed*. Chemical Engineering Journal, 2016. **294**: p. 111-121.
- [30] Wu, W., Y. Luo, G.W. Chu, M.J. Su, Y. Cai, H.K. Zou, and J.F. Chen, *Liquid flow*

behavior in a multiliquid-inlet rotating packed bed reactor with three-dimensional printed packing. Chemical Engineering Journal, 2020. **386**: p. 121537.

[31] Xie, P., X.S. Lu, H.B. Ding, X. Yang, D. Ingham, L. Ma, and M. Pourkashanian, *A mesoscale 3D CFD analysis of the liquid flow in a rotating packed bed.* Chemical Engineering Science, 2019. **199**: p. 528-545.

[32] Xu, Y.C., Y.B. Li, Y.Z. Liu, Y. Luo, G.W. Chu, L.L. Zhang, and J.F. Chen, *Liquid jet impaction on the single-layer stainless steel wire mesh in a rotating packed bed reactor.* AIChE Journal, 2019. **65**(6): p. e16597.

[33] Yang, W., Y. Wang, J. Chen, and W. Fei, *Computational fluid dynamic simulation of fluid flow in a rotating packed bed.* Chemical Engineering Journal, 2010. **156**(3): p. 582-587.

[34] Lu, X., P. Xie, D.B. Ingham, L. Ma, and M. Pourkashanian, *A porous media model for CFD simulations of gas-liquid two-phase flow in rotating packed beds.* Chemical Engineering Science, 2018. **189**: p. 123-134.

[35] Martínez, E.L., R. Jaimes, J.L. Gomez, and R.M. Filho, *CFD simulation of three-dimensional multiphase flow in a rotating packed bed,* in *22nd European Symposium on Computer Aided Process Engineering.* 2012. p. 1158-1162.

[36] Yang, Y.C., Y. Xiang, Y.G. Li, G.W. Chu, H.K. Zou, M. Arowo, and J.F. Chen, *3D CFD modelling and optimization of single-phase flow in rotating packed beds.* Canadian Journal of Chemical Engineering, 2015. **93**(6): p. 1138-1148.

[37] Zhang, W., P. Xie, Y. Li, and J. Zhu, *Modeling of gas-liquid flow in a rotating packed bed using an Eulerian multi-fluid approach.* AIChE Journal, 2022. **68**(4): p.

e17561.

[38] Zhang, W., P. Xie, Y.X. Li, L. Teng, and J.L. Zhu, *CFD analysis of the hydrodynamic characteristics in a rotating packed bed with multi-nozzles*. Chemical Engineering and Processing-Process Intensification, 2020. **158**: p. 108107.

[39] Lu, Y.Z., W. Liu, Y.C. Xu, Y. Luo, G.W. Chu, and J.F. Chen, *Initial liquid dispersion and mass transfer performance in a rotating packed bed*. Chemical Engineering and Processing-Process Intensification, 2019. **140**: p. 136-141.

[40] Su, M.J., Y. Luo, G.W. Chu, Y. Cai, Y. Le, L.L. Zhang, and J.F. Chen, *Dispersion behaviors of droplet impacting on wire mesh and process intensification by surface micro/nano-structure*. Chemical Engineering Science, 2020. **219**: p. 115593.

[41] Ma, C., M. Su, Y. Luo, G. Chu, B. Sun, and J. Chen, *Wetting behavior of the stainless steel wire mesh with Al₂O₃ coatings and mass transfer intensification in a rotating packed bed*. Industrial & Engineering Chemistry Research, 2019. **59**(3): p. 1374-1382.

[42] Sang, L., Y. Luo, G.W. Chu, Y.Z. Liu, X.Z. Liu, and J.F. Chen, *Modeling and experimental studies of mass transfer in the cavity zone of a rotating packed bed*. Chemical Engineering Science, 2017. **170**: p. 355-364.

[43] Guo, K., Z.Z. Zhang, H.J. Luo, J.X. Dang, and Z. Qian, *An innovative approach of the effective mass transfer area in the rotating packed bed*. Industrial & Engineering Chemistry Research, 2014. **53**(10): p. 4052-4058.

[44] Yang, K., G.W. Chu, H.K. Zou, B.C. Sun, L. Shao, and J.F. Chen, *Determination of the effective interfacial area in rotating packed bed*. Chemical Engineering Journal,

2011. **168**(3): p. 1377-1382.

[45] Sang, L., Y. Luo, G.W. Chu, B.C. Sun, L.L. Zhan, and J.F. Chen, *A three-zone mass transfer model for a rotating packed bed*. *AIChE Journal*, 2019. **65**(6): p. e16595.

[46] Burns, J.R. and C. Ramshaw, *Process intensification: Visual study of liquid maldistribution in rotating packed beds*. *Chemical Engineering Science*, 1996. **51**(8): p. 1347-1352.

[47] Liu, Y., W. Wu, Y. Luo, G.W. Chu, W. Liu, B.C. Sun, and J.F. Chen, *CFD simulation and high-speed photography of liquid flow in the outer cavity zone of a rotating packed bed reactor*. *Industrial & Engineering Chemistry Research*, 2019. **58**(13): p. 5280-5290.

[48] Li, Y.B., Z.N. Wen, B.C. Sun, Y. Luo, K.J. Gao, and G.W. Chu, *Flow patterns, liquid holdup, and wetting behavior of viscous liquids in a disk-distributor rotating packed bed*. *Chemical Engineering Science*, 2022. **252**: p. 117256.

[49] Chen, W.C., Z.H. Liu, G.W. Chu, L.L. Zhang, and J.F. Chen, *Dynamics of liquid dispersion in a rotating packed bed with single-layer wire mesh*. *AIChE Journal*, 2023. **69**(8): p. e18106.

[50] Wen, Z., Y. Li, H. Xu, Y. Xu, B. Sun, H. Zou, and G. Chu, *Liquid flow behavior in the concentric mesh packing with novel fiber cross-sectional shape in a rotating packed bed*. *Chemical Engineering Journal*, 2023. **451**: p. 139094.

[51] Sun, Z., H. Liao, L. Wang, L. Jiang, X. Zhang, B. Wang, G. Chu, and Y. Luo, *Liquid flow and breakage behaviors of two liquid jets impacting on the wire mesh with different impinging angles*. *Chemical Engineering Journal*, 2023. **454**: p. 140036.

- [52] Su, M.J., Y. Le, G.W. Chu, Y.B. Li, L.L. Zhang, and Y. Luo, *Intensification of droplet dispersion by using multilayer wire mesh and its application in a rotating packed bed*. Industrial & Engineering Chemistry Research, 2020. **59**(8): p. 3584-3592.
- [53] Zhang, W., P. Xie, Y. Li, L. Teng, and J. Zhu, *3D CFD simulation of the liquid flow in a rotating packed bed with structured wire mesh packing*. Chemical Engineering Journal, 2022. **427**: p. 130874.
- [54] Dančová, P., J. Elcner, O. Hajek, M. Jicha, J. Novosád, and J. Pulec, *2D numerical investigation of liquid dispersion in rotating packed bed and its comparison with experimental measurements using high-speed camera*. EPJ Web of Conferences, 2022. **264**: p. 01012.
- [55] Liu, Z.H., H.Z. Xu, W.C. Chen, Y.B. Li, L.L. Zhang, and G.W. Chu, *Dispersion characteristics of liquid jet impacting on the rotating single-layer wire mesh with different surface wettabilities*. Chemical Engineering Science, 2022. **251**: p. 117495.
- [56] Wen, Z., Y. Li, W. Liu, Y. Luo, L. Zhang, and G. Chu, *Flow behavior in a rotating packed bed reactor with single-layer mesh: Effect of fiber cross-sectional shape*. Chemical Engineering Science, 2022. **248**: p. 117147.
- [57] Liao, H.L., Y. Ouyang, J.P. Zhang, H.K. Zou, G.W. Chu, and Y. Luo, *Numerical studies of a liquid droplet impacting on single-layer hydrophilic and hydrophobic wire meshes*. Industrial & Engineering Chemistry Research, 2022. **61**(20): p. 7154-7162.
- [58] Guo, K., F. Guo, Y.D. Feng, J.F. Chen, C. Zheng, and N.C. Gardner, *Synchronous visual and RTD study on liquid flow in rotating packed-bed contactor*. Chemical Engineering Science, 2000. **55**(9): p. 1699-1706.

- [59] Guo, K., J. Wen, Y. Zhao, Y. Wang, Z. Zhang, Z. Li, and Z. Qian, *Optimal packing of a rotating packed bed for H₂S removal*. Environ Sci Technol, 2014. **48**(12): p. 6844-9.
- [60] Burns, J.R., J.N. Jamil, and C. Ramshaw, *Process intensification: operating characteristics of rotating packed beds - determination of liquid hold-up for a high-voidage structured packing*. Chemical Engineering Science, 2000. **55**(13): p. 2401-2415.
- [61] Sebastia-Saez, D., S. Gu, and M. Ramaioli, *Effect of the contact angle on the morphology, residence time distribution and mass transfer into liquid rivulets: A CFD study*. Chemical Engineering Science, 2018. **176**: p. 356-366.
- [62] Vlahostergiosa, Z., D. Misirlisb, A.I. Papadopoulosc, and P. Seferlisd, *Investigation of the flow field development inside a rotating packed bed with the use of CFD*. Chemical Engineering, 2020. **81**.
- [63] Liu, Y.Z., Y. Luo, G.W. Chu, W. Liu, L. Shao, and J.F. Chen, *Liquid holdup and wetting efficiency in a rotating trickle-bed reactor*. AIChE Journal, 2019. **65**(8): p. e16618.
- [64] Yang, Y.C., Y. Xiang, G.W. Chu, H.K. Zou, Y. Luo, M. Arowo, and J.F. Chen, *A noninvasive X-ray technique for determination of liquid holdup in a rotating packed bed*. Chemical Engineering Science, 2015. **138**: p. 244-255.
- [65] Liu, W., G.W. Chu, Y. Luo, Y.Z. Liu, F.Y. Meng, B.C. Sun, and J.F. Chen, *Mass transfer in a rotating packed bed reactor with a mesh-pin rotor: Modeling and experimental studies*. Chemical Engineering Journal, 2019. **369**: p. 600-610.

- [66] Lin, C.C., Y.S. Chen, and H.S. Liu, *Prediction of liquid holdup in countercurrent-flow rotating packed bed*. Chemical Engineering Research & Design, 2000. **78**(A3): p. 397-403.
- [67] Chen, Y.H., C.Y. Chang, W.L. Su, C.C. Chen, C.Y. Chiu, Y.H. Yu, P.C. Chiang, and S.I.M. Chiang, *Modeling ozone contacting process in a rotating packed bed*. Industrial & Engineering Chemistry Research, 2004. **43**(1): p. 228-236.
- [68] Bašić, A. and M.P. Duduković, *Liquid holdup in rotating packed beds: examination of the film flow assumption*. AIChE Journal, 1995. **41**(2): p. 301-316.
- [69] Zhang, W., P. Xie, Y.X. Li, L. Teng, and J.L. Zhu, *Hydrodynamic characteristics and mass transfer performance of rotating packed bed for CO₂ removal by chemical absorption: A review*. Journal of Natural Gas Science and Engineering, 2020. **79**: p. 103373.
- [70] Burns, J.R., C. Ramshaw, and R.J. Jachuck, *Measurement of liquid film thickness and the determination of spin-up radius on a rotating disc using an electrical resistance technique*. Chemical Engineering Science, 2003. **58**(11): p. 2245-2253.
- [71] Guo, F., C. Zheng, K. Guo, Y. Feng, and N.C. Gardner, *Hydrodynamics and mass transfer in cross-flow rotating packed bed*. Chemical Engineering Science, 1997. **52**(21-22): p. 3853-3859.
- [72] Rauscher, J.W., R. Kelly, and J.D. Cole, *An asymptotic solution for the laminar flow of a thin film on a rotating disk*. 1973: p. 43-47.
- [73] Munjal, S., M.P. Duduković, and P. Ramachandran, *Mass-transfer in rotating packed beds-I. Development of gas-liquid and liquid-solid mass-transfer correlations*.

- Chemical Engineering Science, 1989. **44**(10): p. 2245-2256.
- [74] Woyuan, L., W. Wei, Z. Haikui, C. Guangwen, S. Lei, and C. Jianfeng, *Process intensification of VOC removal from high viscous media by rotating packed bed*. Chinese journal of chemical engineering, 2009. **17**(3): p. 389-393.
- [75] Yi, F., H.K. Zou, G.W. Chu, L. Shao, and J.F. Chen, *Modeling and experimental studies on absorption of CO₂ by Benfield solution in rotating packed bed*. Chemical Engineering Journal, 2009. **145**(3): p. 377-384.
- [76] Liu, W., Y. Luo, Y.Z. Liu, and G.W. Chu, *Scale-up of a rotating packed bed reactor with a mesh-pin rotor: (I) hydrodynamic studies*. Industrial & Engineering Chemistry Research, 2020. **59**(11): p. 5114-5123.
- [77] Gao, Z.M., S.G. Ma, D.T. Shi, J.N. Wang, Y.Y. Bao, and Z.Q. Cai, *Droplet characteristics and behaviors in a high-speed disperser*. Chemical Engineering Science, 2015. **126**: p. 329-340.
- [78] Zhang, J., *Experiment and modelling of liquid flow and mass transfer in rotating packed bed*. 1996, Beijing University of Chemical Technology.
- [79] Chu, G.W., Y. Luo, C.Y. Shan, H.K. Zou, Y. Xiang, L. Shao, and J.F. Chen, *Absorption of SO₂ with ammonia-based solution in a cocurrent rotating packed bed*. Industrial & Engineering Chemistry Research, 2014. **53**(40): p. 15731-15737.
- [80] Sandilya, P., D. Rao, A. Sharma, and G. Biswas, *Gas-phase mass transfer in a centrifugal contactor*. Industrial & engineering chemistry research, 2001. **40**(1): p. 384-392.
- [81] Neumann, K., S. Hunold, M. Skiborowski, and A. Gorak, *Dry pressure drop in*

- rotating packed beds-systematic experimental studies*. Industrial & Engineering Chemistry Research, 2017. **56**(43): p. 12395-12405.
- [82] Singh, S.P., J.H. Wilson, R.M. Counce, J.F. Villiersfisher, H.L. Jennings, A.J. Lucero, G.D. Reed, R.A. Ashworth, and M.G. Elliott, *Removal of volatile organic-compounds from groundwater using a rotary air stripper*. Industrial & Engineering Chemistry Research, 1992. **31**(2): p. 574-580.
- [83] Zhao, B., W. Tao, M. Zhong, Y. Su, and G. Cui, *Process, performance and modeling of CO₂ capture by chemical absorption using high gravity: A review*. Renewable and Sustainable Energy Reviews, 2016. **65**: p. 44-56.
- [84] Liu, X.W., M.J. Jing, S.H. Chen, and L.L. Du, *Experimental study of gas pressure drop in rotating packed bed with rotational-stationary packing*. Canadian Journal of Chemical Engineering, 2018. **96**(2): p. 590-596.
- [85] Lin, C.C. and G.S. Jian, *Characteristics of a rotating packed bed equipped with blade packings*. Separation and Purification Technology, 2007. **54**(1): p. 51-60.
- [86] Lin, C.C. and B.C. Chen, *Characteristics of cross-flow rotating packed beds*. Journal of Industrial and Engineering Chemistry, 2008. **14**(3): p. 322-327.
- [87] Liu, H.S., C.C. Lin, S.C. Wu, and H.W. Hsu, *Characteristics of a rotating packed bed*. Industrial & Engineering Chemistry Research, 1996. **35**(10): p. 3590-3596.
- [88] Ghadyanlou, F., A. Azari, and A. Vatani, *A review of modeling rotating packed beds and improving their parameters: gas-liquid contact*. Sustainability, 2021. **13**(14): p. 8046.
- [89] Llerena-Chavez, H. and F. Larachi, *Analysis of flow in rotating packed beds via*

CFD simulations-Dry pressure drop and gas flow maldistribution. Chemical Engineering Science, 2009. **64**(9): p. 2113-2126.

[90] Wu, W., Y. Luo, G.W. Chu, Y. Liu, H.K. Zou, and J.F. Chen, *Gas flow in a multiliquid-inlet rotating packed bed: three-dimensional numerical simulation and internal optimization*. Industrial & Engineering Chemistry Research, 2018. **57**(6): p. 2031-2040.

[91] Onda, K., H. Takeuchi, and Y. Okumoto, *Mass transfer coefficients between gas and liquid phases in packed columns*. Journal of chemical engineering of Japan, 1968. **1**(1): p. 56-62.

[92] Kang, J.L., K. Sun, D.S.H. Wong, S.S. Jang, and C.S. Tan, *Modeling studies on absorption of CO₂ by monoethanolamine in rotating packed bed*. International Journal of Greenhouse Gas Control, 2014. **25**: p. 141-150.

[93] Kang, J.L., D.S.H. Wong, S.S. Jang, and C.S. Tan, *A comparison between packed beds and rotating packed beds for CO₂ capture using monoethanolamine and dilute aqueous ammonia solutions*. International Journal of Greenhouse Gas Control, 2016. **46**: p. 228-239.

[94] Rajan, S., M. Kumar, M.J. Ansari, D.P. Rao, and N. Kaistha, *Limiting gas liquid flows and mass transfer in a novel rotating packed bed (HiGee)*. Industrial & Engineering Chemistry Research, 2011. **50**(2): p. 986-997.

[95] Luo, Y., G.W. Chu, H.K. Zou, Z.Q. Zhao, M.P. Dudukovic, and J.F. Chen, *Gas-liquid effective interfacial area in a rotating packed bed*. Industrial & Engineering Chemistry Research, 2012. **51**(50): p. 16320-16325.

- [96] Luo, Y., J.Z. Luo, G.W. Chu, Z.Q. Zhao, M. Arowo, and J.F. Chen, *Investigation of effective interfacial area in a rotating packed bed with structured stainless steel wire mesh packing*. Chemical Engineering Science, 2017. **170**: p. 347-354.
- [97] Tsai, C.Y. and Y.S. Chen, *Effective interfacial area and liquid-side mass transfer coefficients in a rotating bed equipped with baffles*. Separation and Purification Technology, 2015. **144**: p. 139-145.
- [98] Joel, A.S., M.H. Wang, C. Ramshaw, and E. Oko, *Process analysis of intensified absorber for post-combustion CO₂ capture through modelling and simulation*. International Journal of Greenhouse Gas Control, 2014. **21**: p. 91-100.
- [99] Joel, A.S., M.H. Wang, C. Ramshaw, and E. Oko, *Modelling, simulation and analysis of intensified regenerator for solvent based carbon capture using rotating packed bed technology*. Applied Energy, 2017. **203**: p. 11-25.
- [100] Borhani, T.N., E. Oko, and M. Wang, *Process modelling and analysis of intensified CO₂ capture using monoethanolamine (MEA) in rotating packed bed absorber*. Journal of Cleaner Production, 2018. **204**: p. 1124-1142.
- [101] Borhani, T.N., E. Oko, and M. Wang, *Process modelling, validation and analysis of rotating packed bed stripper in the context of intensified CO₂ capture with MEA*. Journal of Industrial and Engineering Chemistry, 2019. **75**: p. 285-295.
- [102] Qian, Z., L.B. Xu, H.B. Cao, and K. Guo, *Modeling study on absorption of CO₂ by aqueous solutions of N-methyldiethanolamine in rotating packed bed*. Industrial & Engineering Chemistry Research, 2009. **48**(20): p. 9261-9267.
- [103] Oko, E., C. Ramshaw, and M. Wang, *Study of intercooling for rotating packed*

- bed absorbers in intensified solvent-based CO₂ capture process*. Applied Energy, 2018. **223**: p. 302-316.
- [104] Xie, P., *Hydrodynamics and mass transfer of rotating packed beds for CO₂ capture*. 2019, University of Sheffield.
- [105] Sun, B.C., X.M. Wang, J.M. Chen, G.W. Chu, J.F. Chen, and L. Shao, *Simultaneous absorption of CO₂ and NH₃ into water in a rotating packed bed*. Industrial & Engineering Chemistry Research, 2009. **48**(24): p. 11175-11180.
- [106] Zhang, L.L., J.X. Wang, Y. Xiang, X.F. Zeng, and J.F. Chen, *Absorption of carbon dioxide with ionic liquid in a rotating packed bed contactor: mass transfer study*. Industrial & Engineering Chemistry Research, 2011. **50**(11): p. 6957-6964.
- [107] Qian, Z., Z.H. Li, and K. Guo, *Industrial applied and modeling research on selective H₂S removal using a rotating packed bed*. Industrial & Engineering Chemistry Research, 2012. **51**(23): p. 8108-8116.
- [108] Qian, Z., L.B. Xu, Z.H. Li, H. Li, and K. Guo, *Selective absorption of H₂S from a gas mixture with CO₂ by aqueous N-methyldiethanolamine in a rotating packed bed*. Industrial & Engineering Chemistry Research, 2010. **49**(13): p. 6196-6203.
- [109] Luo, X.B., M.H. Wang, J. Lee, and J. Hendry, *Dynamic modelling based on surface renewal theory, model validation and process analysis of rotating packed bed absorber for carbon capture*. Applied Energy, 2021. **301**: p. 117462.
- [110] Glasscock, D.A. and G.T. Rochelle, *Numerical-simulation of theories for gas-absorption with chemical-reaction*. AIChE Journal, 1989. **35**(8): p. 1271-1281.
- [111] Gbadago, D., H.T. Oh, D.H. Oh, C.H. Lee, and M. Oh, *CFD simulation of a*

- packed bed industrial absorber with interbed liquid distributors*. International Journal of Greenhouse Gas Control, 2020. **95**: p. 102983.
- [112] Kim, J., D.A. Pham, and Y.I. Lim, *Gas-liquid multiphase computational fluid dynamics (CFD) of amine absorption column with structured-packing for CO₂ capture*. Computers & Chemical Engineering, 2016. **88**: p. 39-49.
- [113] Kim, J., D.A. Pham, and Y.I. Lim, *Effect of gravity center position on amine absorber with structured packing under offshore operation: Computational fluid dynamics approach*. Chemical Engineering Research & Design, 2017. **121**: p. 99-112.
- [114] Pham, D.A., Y.I. Lim, H. Jee, E. Ahn, and Y. Jung, *Porous media Eulerian computational fluid dynamics (CFD) model of amine absorber with structured-packing for CO₂ removal*. Chemical Engineering Science, 2015. **132**: p. 259-270.
- [115] Pham, D.A., Y.I. Lim, H. Jee, E. Ahn, and Y. Jung, *Effect of ship tilting and motion on amine absorber with structured-packing for CO₂ removal from natural gas*. AIChE Journal, 2015. **61**(12): p. 4412-4425.
- [116] Sang, L., Y. Luo, G.W. Chu, J.P. Zhang, Y. Xiang, and J.F. Chen, *Liquid flow pattern transition, droplet diameter and size distribution in the cavity zone of a rotating packed bed: A visual study*. Chemical Engineering Science, 2017. **158**: p. 429-438.
- [117] Zheng, C., K. Guo, Y.D. Feng, C. Yang, and N.C. Gardner, *Pressure drop of centripetal gas flow through rotating beds*. Industrial & Engineering Chemistry Research, 2000. **39**(3): p. 829-834.
- [118] Shamsi, R. and H. Ghassemi, *Time-accurate analysis of the viscous flow around puller podded drive using sliding mesh method*. Journal of Fluids Engineering-

Transactions of the Asme, 2015. **137**(1): p. 011101.

[119] Yang, W.J., Y.D. Wang, J.F. Chen, and W.Y. Fei, *Computational fluid dynamic simulation of fluid flow in a rotating packed bed*. Chemical Engineering Journal, 2010. **156**(3): p. 582-587.

[120] Schiller, L., *Über die grundlegenden Berechnungen bei der Schwerkraftaufbereitung*. Z. Vereines Deutscher Inge., 1933. **77**: p. 318-321.

[121] Attou, A., C. Boyer, and G. Ferschneider, *Modelling of the hydrodynamics of the cocurrent gas-liquid trickle flow through a trickle-bed reactor*. Chemical Engineering Science, 1999. **54**(6): p. 785-802.

[122] Lappalainen, K., V. Alopaeus, M. Manninen, and J. Aittamaa, *Improved hydrodynamic model for wetting efficiency, pressure drop, and liquid holdup in trickle-bed reactors*. Industrial & Engineering Chemistry Research, 2008. **47**(21): p. 8436-8444.

[123] Iliuta, I., F. Larachi, M. Fourati, L. Raynal, and V. Roig, *Flooding limit in countercurrent gas-liquid structured packed beds-Prediction from a linear stability analysis of an Eulerian two-fluid model*. Chemical Engineering Science, 2014. **120**: p. 49-58.

[124] Zhang, C. and A. Bokil, *A quasi-three-dimensional approach to simulate the two-phase fluid flow and heat transfer in condensers*. International Journal of Heat and Mass Transfer, 1997. **40**(15): p. 3537-3546.

[125] Kołodziej, A. and J. Łojewska, *Experimental and modelling study on flow resistance of wire gauzes*. Chemical Engineering and Processing: Process

Intensification, 2009. **48**(3): p. 816-822.

[126] Kołodziej, A., J. Łojewska, M. Jaroszyński, A. Gancarczyk, and P. Jodłowski, *Heat transfer and flow resistance for stacked wire gauzes: Experiments and modelling*. International Journal of Heat and Fluid Flow, 2012. **33**(1): p. 101-108.

[127] Bussière, W., D. Rochette, S. Clain, P. André, and J.B. Renard, *Pressure drop measurements for woven metal mesh screens used in electrical safety switchgears*. International Journal of Heat and Fluid Flow, 2017. **65**: p. 60-72.

[128] Boyer, C., A. Koudil, P. Chen, and M.P. Dudukovic, *Study of liquid spreading from a point source in a trickle bed via gamma-ray tomography and CFD simulation*. Chemical Engineering Science, 2005. **60**(22): p. 6279-6288.

[129] Wang, Y.N., J.W. Chen, and F. Larachi, *Modelling and simulation of trickle-bed reactors using computational fluid dynamics: A state-of-the-art review*. Canadian Journal of Chemical Engineering, 2013. **91**(1): p. 136-180.

[130] Fourati, M., V. Roig, and L. Raynal, *Liquid dispersion in packed columns: Experiments and numerical modeling*. Chemical Engineering Science, 2013. **100**: p. 266-278.

[131] Carney, J.E. and J.R. Finn, *Device scale modeling of solvent absorption using MFIX-TFM*. 2016, National Energy Technology Lab.(NETL), Albany, OR (United States).

[132] Guo, J., W.Z. Jiao, G.S. Qi, Z.G. Yuan, and Y.Z. Liu, *Applications of high-gravity technologies in gas purifications: A review*. Chinese Journal of Chemical Engineering, 2019. **27**(6): p. 1361-1373.

- [133] Sudhoff, D., M. Leimbrink, M. Schleinitz, A. Gorak, and P. Lutze, *Modelling, design and flexibility analysis of rotating packed beds for distillation*. Chemical Engineering Research & Design, 2015. **94**: p. 72-89.
- [134] Kang, J.L., Z.J. Luo, J.L. Liu, K. Sun, D.S.H. Wong, S.S. Jang, C.S. Tan, and J.F. Shen, *Experiment and modeling studies on absorption of CO₂ by dilute ammonia in rotating packed bed*. 12th International Conference on Greenhouse Gas Control Technologies, Ghgt-12, 2014. **63**: p. 1308-1313.
- [135] Sheng, M.P., B.C. Sun, F.M. Zhang, G.W. Chu, L.L. Zhang, C.G. Liu, J.F. Chen, and H.K. Zou, *Mass-transfer characteristics of the CO₂ absorption process in a rotating packed bed*. Energy & Fuels, 2016. **30**(5): p. 4215-4220.
- [136] Yang, Y.C., Y. Ouyang, N. Zhang, Q.J. Yu, and M. Arowo, *A review on computational fluid dynamic simulation for rotating packed beds*. Journal of Chemical Technology and Biotechnology, 2019. **94**(4): p. 1017-1031.
- [137] Wenzel, D. and A. Gorak, *Review and analysis of micromixing in rotating packed beds*. Chemical Engineering Journal, 2018. **345**: p. 492-506.
- [138] Wang, Z.H., T. Yang, Z.X. Liu, S.C. Wang, Y. Gao, and M.G. Wu, *Mass transfer in a rotating packed bed: A critical review*. Chemical Engineering and Processing-Process Intensification, 2019. **139**: p. 78-94.
- [139] Wang, M., A.S. Joel, C. Ramshaw, D. Eimer, and N.M. Musa, *Process intensification for post-combustion CO₂ capture with chemical absorption: A critical review*. Applied Energy, 2015. **158**: p. 275-291.
- [140] Zhang, G.J., D. Ingham, L. Ma, and M. Pourkashanian, *Modelling of 3D liquid*

- dispersion in a rotating packed bed using an Eulerian porous medium approach.* Chemical Engineering Science, 2022. **250**: p. 117393.
- [141] Chamchan, N., J. Chang, H. Hsu, J. Kang, D.S.H. Wong, S. Jang, and J. Shen, *Comparison of rotating packed bed and packed bed absorber in pilot plant and model simulation for CO₂ capture.* Journal of the Taiwan Institute of Chemical Engineers, 2017. **73**: p. 20-26.
- [142] Thiels, M., D.S.H. Wong, C.H. Yu, J.L. Kang, S.S. Jang, and C.S. Tan, *Modelling and design of carbon dioxide absorption in rotating packed bed and packed column.* Ifac Papersonline, 2016. **49(7)**: p. 895-900.
- [143] Attou, A. and G. Ferschneider, *A two-fluid model for flow regime transition in gas-liquid trickle-bed reactors.* Chemical Engineering Science, 1999. **54(21)**: p. 5031-5037.
- [144] Ergun, S., *Fluid flow through packed columns.* Chemical Engineering Progress, 1952. **48(2)**: p. 89-94.
- [145] Ishii, M. and N. Zuber, *Drag coefficient and relative velocity in bubbly, droplet or particulate flows.* AIChE Journal, 1979. **25(5)**: p. 843-855.
- [146] Grosser, K., R. Carbonell, and S. Sundaresan, *Onset of pulsing in two-phase cocurrent downflow through a packed bed.* AIChE Journal, 1988. **34(11)**: p. 1850-1860.
- [147] Jiang, Y., M.R. Khadilkar, M.H. Al-Dahhan, and A.P. Dudukovic, *CFD of multiphase flow in packed-bed reactors: I. k-fluid modeling issues.* AIChE Journal, 2002. **48(4)**: p. 701-715.
- [148] Gunjal, P.R., M.N. Kashid, V.V. Ranade, and R.V. Chaudhari, *Hydrodynamics of*

trickle-bed reactors: Experiments and CFD modeling. Industrial & Engineering Chemistry Research, 2005. **44**(16): p. 6278-6294.

[149] Solomenko, Z., Y. Haroun, M. Fourati, F. Larachi, C. Boyer, and F. Augier, *Liquid spreading in trickle-bed reactors: Experiments and numerical simulations using Eulerian-Eulerian two-fluid approach*. Chemical Engineering Science, 2015. **126**: p. 698-710.

[150] Liu, S.J. and J. Long, *Gas-liquid countercurrent flows through packed towers*. Journal of Porous Media, 2000. **3**(2): p. 99-113.

[151] Mewes, D., T. Loser, and M. Millies, *Modelling of two-phase flow in packings and monoliths*. Chemical Engineering Science, 1999. **54**(21): p. 4729-4747.

[152] Lappalainen, K., M. Manninen, and V. Alopaeus, *CFD modeling of radial spreading of flow in trickle-bed reactors due to mechanical and capillary dispersion*. Chemical Engineering Science, 2009. **64**(2): p. 207-218.

[153] Sebastia-Saez, D., S. Gu, P. Ranganathan, and K. Papadikis, *Micro-scale CFD modeling of reactive mass transfer in falling liquid films within structured packing materials*. International Journal of Greenhouse Gas Control, 2015. **33**: p. 40-50.

[154] Liu, G.B., K.T. Yu, X.G. Yuan, C.J. Liu, and Q.C. Guo, *Simulations of chemical absorption in pilot-scale and industrial-scale packed columns by computational mass transfer*. Chemical Engineering Science, 2006. **61**(19): p. 6511-6529.

[155] Snijder, E.D., M.J.M. Teriele, G.F. Versteeg, and W.P.M. Vanswaaij, *Diffusion-coefficients of several aqueous alkanolamine solutions*. Journal of Chemical and Engineering Data, 1993. **38**(3): p. 475-480.

- [156] Wellek, R., R. Brunson, and F. Law, *Enhancement factors for gas-absorption with second-order irreversible chemical reaction*. The Canadian Journal of Chemical Engineering, 1978. **56**(2): p. 181-186.
- [157] Penttila, A., C. Dell'Era, P. Uusi-Kyyny, and V. Alopaeus, *The Henry's law constant of N₂O and CO₂ in aqueous binary and ternary amine solutions (MEA, DEA, DIPA, MDEA, and AMP)*. Fluid Phase Equilibria, 2011. **311**: p. 59-66.
- [158] Dashliborun, A.M., F. Larachi, and S.M. Taghavi, *Gas-liquid mass-transfer behavior of packed-bed scrubbers for floating/offshore CO₂ capture*. Chemical Engineering Journal, 2019. **377**: p. 119236.
- [159] Jiru, Y. and D.A. Eimer, *A study of mass transfer kinetics of carbon dioxide in (monoethanolamine + water) by stirred cell*. Energy Procedia, 2013. **37**: p. 2180-2187.
- [160] Ying, J.R. and D.A. Eimer, *Determination and measurements of mass transfer kinetics of CO₂ in concentrated aqueous monoethanolamine solutions by a stirred cell*. Industrial & Engineering Chemistry Research, 2013. **52**(7): p. 2548-2559.
- [161] Kolawole, T.O., *Intensified post-combustion carbon capture using a pilot scale rotating packed bed and monoethanolamine solutions*. 2019, Newcastle University.
- [162] Danckwerts, P., *The reaction of CO₂ with ethanolamines*. Chemical Engineering Science, 1979. **34**(4): p. 443-446.
- [163] Ebadi Amooghin, A., M.M. Moftakhari Sharifzadeh, and M. Zamani Pedram, *Rigorous modeling of gas permeation behavior in facilitated transport membranes (FTMs); evaluation of carrier saturation effects and double-reaction mechanism*. Greenhouse Gases: Science and Technology, 2018. **8**(3): p. 429-443.

- [164] Sharifzadeh, M.M.M., A.E. Amooghin, M.Z. Pedram, and M. Omidkhah, *Time-dependent mathematical modeling of binary gas mixture in facilitated transport membranes (FTMs): A real condition for single-reaction mechanism*. Journal of Industrial and Engineering Chemistry, 2016. **39**: p. 48-65.
- [165] Sebastia-Saez, D., S. Gu, and P. Ranganathan, *Volume of fluid modeling of the reactive mass transfer of CO₂ into aqueous amine solutions in structured packed elements at micro-scale*. Energy Procedia, 2014. **63**: p. 1229-1242.
- [166] Luo, X., A. Hartono, and H.F. Svendsen, *Comparative kinetics of carbon dioxide absorption in unloaded aqueous monoethanolamine solutions using wetted wall and string of discs columns*. Chemical Engineering Science, 2012. **82**: p. 31-43.
- [167] Hikita, H., S. Asai, H. Ishikawa, and M. Honda, *The kinetics of reactions of carbon dioxide with monoethanolamine, diethanolamine and triethanolamine by a rapid mixing method*. the chemical Engineering Journal, 1977. **13**(1): p. 7-12.
- [168] Versteeg, G. and W.P.M. van Swaaij, *On the kinetics between CO₂ and alkanolamines both in aqueous and non-aqueous solutions—I. Primary and secondary amines*. Chemical engineering science, 1988. **43**(3): p. 573-585.
- [169] Luo, X., A. Hartono, S. Hussain, and H.F. Svendsen, *Mass transfer and kinetics of carbon dioxide absorption into loaded aqueous monoethanolamine solutions*. Chemical Engineering Science, 2015. **123**: p. 57-69.
- [170] Versteeg, G.F., L.A.J. Van Dijck, and W.P.M. Van Swaaij, *On the kinetics between CO₂ and alkanolamines both in aqueous and non-aqueous solutions. An overview*. Chemical Engineering Communications, 1996. **144**(1): p. 113-158.

- [171] Plaza, J.M., D.V. Wagener, and G.T. Rochelle, *Modeling CO₂ capture with aqueous monoethanolamine*. Energy Procedia, 2009. **1**(1): p. 1171-1178.
- [172] Hughmark, G.A., *Mass and heat transfer from rigid spheres*. AIChE Journal, 1967. **13**(6): p. 1219-1221.
- [173] Wenzel, D., N. Gerdes, M. Steinbrink, L.S. Ojeda, and A. Górak, *Liquid distribution and mixing in rotating packed beds*. Industrial & Engineering Chemistry Research, 2018. **58**(15): p. 5919-5928.
- [174] Shih, T., W.W. Liou, A. Shabbir, Z. Yang, and J. Zhu, *A new $k-\epsilon$ eddy viscosity model for high reynolds number turbulent flows*. Computers & fluids, 1995. **24**(3): p. 227-238.
- [175] Lateb, M., C. Masson, T. Stathopoulos, and C. Bédard, *Comparison of various types of $k-\epsilon$ models for pollutant emissions around a two-building configuration*. Journal of Wind Engineering and Industrial Aerodynamics, 2013. **115**: p. 9-21.
- [176] Ouyang, Y., Y. Xiang, X.Y. Gao, W.L. Li, H.K. Zou, G.W. Chu, and J.F. Chen, *Micromixing efficiency in a rotating packed bed with non-Newtonian fluid*. Chemical Engineering Journal, 2018. **354**: p. 162-171.
- [177] Wang, J.Q., Y. Ouyang, W.L. Li, A. Esmacili, Y. Xiang, and J.F. Chen, *CFD analysis of gas flow characteristics in a rotating packed bed with randomly arranged spherical packing*. Chemical Engineering Journal, 2020. **385**: p. 123812.
- [178] Lappalainen, K., E. Gorshkova, M. Manninen, and V. Alopaeus, *Characteristics of liquid and tracer dispersion in trickle-bed reactors: Effect on CFD modeling and experimental analyses*. Computers & Chemical Engineering, 2011. **35**(1): p. 41-49.

- [179] Hoek, P.J., J.A. Wesselingh, and F.J. Zuiderweg, *Small-scale and large-scale liquid maldistribution in packed-columns*. Chemical Engineering Research & Design, 1986. **64**(6): p. 431-449.
- [180] Baldi, G. and V. Specchia, *Distribution and radial spread of liquid in packed towers with two phase cocurrent flow: effect of packing shape and size*. Quaderni dell'Ingegnere Chimico Italiano, 1976. **12**: p. 107-111.
- [181] Onda, K., H. Takeuchi, Y. Maeda, and N. Takeuchi, *Liquid distribution in a packed-column*. Chemical Engineering Science, 1973. **28**(9): p. 1677-1683.
- [182] Delgado, J.M.P.Q., *A critical review of dispersion in packed beds*. Heat and Mass Transfer, 2005. **42**(4): p. 279-310.
- [183] Yang, K., G.W. Chu, L. Shao, Y. Luo, and J.F. Chen, *Micromixing efficiency of rotating packed bed with premixed liquid distributor*. Chemical Engineering Journal, 2009. **153**(1-3): p. 222-226.
- [184] Lee, J., T. Kolawole, and P. Attidekou, *Carbon capture from a simulated flue gas using a rotating packed bed adsorber and mono ethanol amine (MEA)*. 13th International Conference on Greenhouse Gas Control Technologies, Ghgt-13, 2017. **114**: p. 1834-1840.
- [185] Amundsen, T.G., L.E. Oi, and D.A. Eimer, *Density and viscosity of monoethanolamine plus water plus carbon dioxide from (25 to 80) degrees C*. Journal of Chemical and Engineering Data, 2009. **54**(11): p. 3096-3100.
- [186] Vázquez, G., E. Alvarez, J.M. Navaza, R. Rendo, and E. Romero, *Surface tension of binary mixtures of water+ monoethanolamine and water+ 2-amino-2-methyl-1-*

propanol and tertiary mixtures of these amines with water from 25 C to 50 C. Journal of Chemical & Engineering Data, 1997. **42**(1): p. 57-59.

[187] Vaewhongs, P., K. Photein, R. Nimchareon, T. Limlertchareonwanit, K. Minakanishtha, K. Maneeintr, and T. Charinpanitkul, *Gas-phase mass transfer coefficient of CO₂ in different alkanolamine solutions within packed-bed absorption column*, in *The Second Materials Research Society of Thailand International Conference*. 2020.

[188] Esmacili, A., A. Tamuzi, T.N. Borhani, Y. Xiang, and L. Shao, *Modeling of carbon dioxide absorption by solution of piperazine and methyldiethanolamine in a rotating packed bed*. Chemical Engineering Science, 2022. **248**: p. 117118.

[189] Qing, Z., G. Yincheng, and N. Zhenqi, *Experimental studies on removal capacity of carbon dioxide by a packed reactor and a spray column using aqueous ammonia*. Energy Procedia, 2011. **4**: p. 519-524.

[190] Sønderby, T.L., K.B. Carlsen, P.L. Fosbøl, L.G. Kiørboe, and N. von Solms, *A new pilot absorber for CO₂ capture from flue gases: Measuring and modelling capture with MEA solution*. International Journal of Greenhouse Gas Control, 2013. **12**: p. 181-192.

[191] Wu, X.M., M. He, Y.S. Yu, Z. Qin, and Z.X. Zhang, *Overall mass transfer coefficient of CO₂ absorption in a diameter-varying spray tower*. 13th International Conference on Greenhouse Gas Control Technologies, Ghgt-13, 2017. **114**: p. 1665-1670.

[192] Kuntz, J. and A. Aroonwilas, *Mass-transfer efficiency of a spray column for CO₂*

- capture by MEA*. Greenhouse Gas Control Technologies 9, 2009. **1**(1): p. 205-209.
- [193] Ouyang, Y., Y. Xiang, X.Y. Gao, H.K. Zou, G.W. Chu, R.K. Agarwal, and J.F. Chen, *Micromixing efficiency optimization of the premixer of a rotating packed bed by CFD*. Chemical Engineering and Processing-Process Intensification, 2019. **142**: p. 107543.
- [194] Chen, Y.S., C.C. Lin, and H.S. Liu, *Mass transfer in a rotating packed bed with various radii of the bed*. Industrial & Engineering Chemistry Research, 2005. **44**(20): p. 7868-7875.
- [195] Akram, M., U. Ali, T. Best, S. Blakey, K.N. Finney, and M. Pourkashanian, *Performance evaluation of PACT Pilot-plant for CO₂ capture from gas turbines with Exhaust Gas Recycle*. International Journal of Greenhouse Gas Control, 2016. **47**: p. 137-150.
- [196] Rezazadeh, F., W.F. Gale, M. Akram, K.J. Hughes, and M. Pourkashanian, *Performance evaluation and optimisation of post combustion CO₂ capture processes for natural gas applications at pilot scale via a verified rate-based model*. International Journal of Greenhouse Gas Control, 2016. **53**: p. 243-253.
- [197] Agarwal, L., V. Pavani, D. Rao, and N. Kaistha, *Process intensification in HiGee absorption and distillation: design procedure and applications*. Industrial & engineering chemistry research, 2010. **49**(20): p. 10046-10058.
- [198] Kim, Y.E., J.A. Lim, S.K. Jeong, Y.I. Yoon, S.T. Bae, and S.C. Nam, *Comparison of carbon dioxide absorption in aqueous MEA, DEA, TEA, and AMP solutions*. Bulletin of the Korean Chemical Society, 2013. **34**(3): p. 783-787.

- [199] Lin, C. and B. Chen, *Carbon dioxide absorption in a cross-flow rotating packed bed*. Chemical Engineering Research and Design, 2011. **89**(9): p. 1722-1729.